Final Report for NOAA-NWS Grant NA10NWS468006

Development of an Integrated Wave-Current-Wind Forecasting System for Cook Inlet: Supplementing NCEP's Forecasting Efforts

<u>Submitted by</u>

Vijay Panchang (Principal Investigator)
Department of Ocean Engineering
Texas A&M University

July 2017

Table of Contents

CHAPTER 1. INTRODUCTION

Cook Inlet (CI) is a large estuary (~ 180 miles long), stretching from the Gulf of Alaska to Anchorage in south-central Alaska (Fig. 1.1). CI has a great deal of human activity, including high levels of resource extraction (about 16 oil and gas platforms, timber, minerals, etc). Approximately half of Alaska's population lives along CI's shores. Anchorage, on Knik Arm at the head of CI, is Alaska's largest city and a center of transportation, commerce, industry, and tourism. The Port of Anchorage receives food, fuel, building materials, durable and expendable supplies of all kinds for delivery to over 80% of Alaska's population and to four large military installations. Shipping routes in CI serve the port year-round, as well as the ports of Nikiski, Homer, and Drift River with transshipment to smaller coastal communities. Other marine traffic is related to the recreation and tourism industries, as well as commercial fishing for halibut and salmon, on which the coastal communities of the Kenai Peninsula depend. Homer Harbor is one of the largest boat harbors in the State and is often full to capacity with commercial and charter fishing, excursion, government agency, and private recreation boats. Kenai and Nikiski residents and businesses also depend on offshore oil and gas development in the central inlet and associated businesses onshore. The majority of citizens living in the south-central Alaska rely on the marine environment to some extent for subsistence, recreation, or commerce, and have need for reliable information about the marine environment. Offshore oil and gas operations also require wave information for design and evacuation purposes.

CI is also an extremely dynamic system. Exposure to the Gulf of Alaska, where the waves are among the largest waves in the world, renders human activities in CI vulnerable to complex and dangerous ocean conditions. Often, wave heights greater than 7 m are recorded by the buoys near the entrance to the inlet (Fig. 1.1). There are also large tidal variations (about 8-9 m, the largest in the US) and the complex bathymetry and coastal morphology result in large tidal currents. For example, tidal bores are commonly found in Turnagain Arm, creating currents in excess of 2-3 m/s. Currents on the order of 1-2 m/s also occur throughout the inlet during full tidal flow. There is also significant wave-current action and during low tide, silty bottoms (mudflats) are exposed which cause navigation difficulties including the grounding of boats during low tide (e.g. *Anchorage Daily News,* 9/9/2011). In addition, the interaction of the rugged topography (mountain ranges with elevations that abruptly rise to 3000 m, gaps, and channels) with strong atmospheric pressure gradients results in the so-called "gap winds" that adversely affect maritime and aviation activities during the winter season (Liu et al. 2006). As stated by Liu et al. (2006): "Weather in the North Gulf of Alaska is characterized by a high frequency of deep synoptic-scale low-pressure systems, especially during the cold season. The strong pressure gradients of these storms interact with the extremely rugged terrain of the coastal mountains to produce a variety of channeled flows". Liu et al. (2006) identify the existence of several low-level wind jets in the CI and Shelikof Strait areas, which have been classified into 10 different regimes by location and orientation. They report: "The nature of a particular regime is largely a function of pressure gradient orientation and local topography. Jets in the same group have a similar occurrence distribution with time. Some form of jet occurred in the study region almost daily each month of the period _ _ _ _ _". Mariners piloting

vessels in the region attest to the impact of the interaction of these forces on maritime operations.
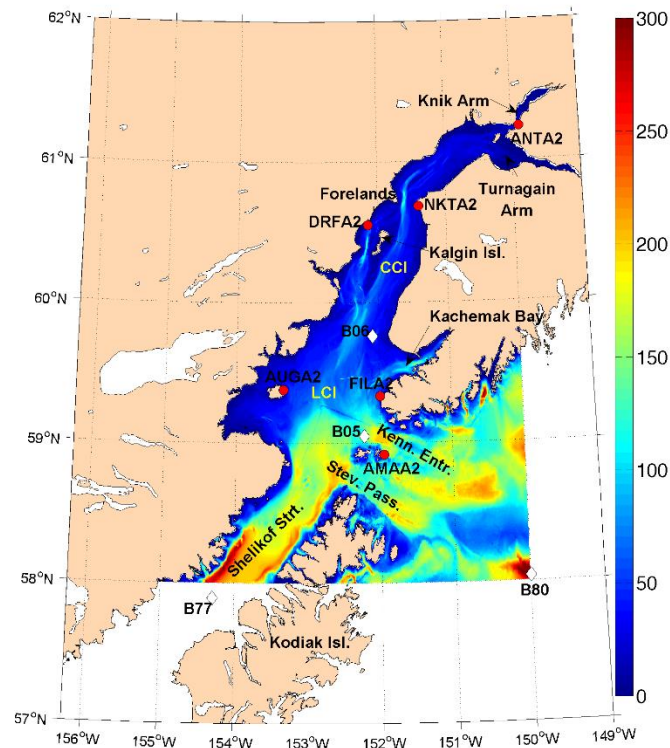
Fig. 1.1 CI region. Color represents bathymetry in meters (with respect to mean sea level), red circles denote weather stations, and diamonds denote buoy locations [From Singhal et al. 2013].

In this context, a project was developed to generate wave information for the CI area in the form of wave forecasts. The goal was to develop a real-time wave forecasting system that could help in planning, operation, and maintenance works associated with offshore drilling platforms, navigation, and various other human activities in CI. Wave predictions for the Gulf of Alaska region are in fact produced by the National Centers for Environmental Prediction (NCEP), but as part of a large-scale simulation for the entire Pacific Ocean (Tolman 2009). Well-established and validated energy-balance models like WAVEWATCH III^{TM} are used for this purpose along with simulated wind-fields. For a large domain such as the Pacific, the resolution must necessarily be coarse, and a grid of ~ 30 km was used by NCEP. In the last few years, NCEP has extended the forecasts into CI at finer resolution to produce first-order estimates of the wave conditions. We refer to them as first-order estimates because it is difficult for models operating on such a scale to accommodate numerous local effects such as bathymetric and geometric variability, complex regional wind dynamics, tidal and wind-driven currents, flooding and drying of many regions, and of course, detailed validation.

Over the last few years, regional wave forecasting systems have been established for various locations around the world. These systems provide wave forecasts on high-resolution grids and are connected to coarse resolution global wave forecasts produced by NCEP. Some examples include forecasted wave conditions in the Gulf of Maine (www.gomoos.com) and Prince

2

William Sound (www.aoos.org), that utilize the wave model SWAN ("Simulating Waves Nearshore"; Booij et al. 1999, Ris et al. 1999) to provide high-resolution wave forecasts for up to 48 hours (see Singhal et al. 2010 for details related to the Prince William Sound forecasting system). In some cases, the regional wave model is also coupled with the circulation model to account for wave-current interaction. For instance, wave forecasts in Humboldt Bay (provided by National Weather Service, Eureka) include the effect of tidal currents near the harbor entrance. Coupled forecasts of surface waves and currents are also provided by the Naval Research Laboratory for the Mississippi and Southern California Bights. However, the tidal range and magnitude of the currents at these locations are not as extreme as found in CI. They were similarly small in the studies of Chen et al. (2007) and Funakoshi et al. (2008), who coupled SWAN and ADCIRC ("Advanced Circulation") for various applications. Further, both of these latter studies were done in hindcast mode where computational efficiency was not an issue. In the forecasting mode, on the other hand, efficiency becomes a critical consideration so that the output may be provided in reasonable time.

The viability of interconnecting multiple models (i.e. winds, waves, and currents) in a dynamic environment such as CI presents unique challenges. It was necessary for us to identify and include, in the regional CI forecasting scheme, those phenomena that significantly influence the waves, but without expanding the cost and effort required to generate the forecast. An integrated wave system must include the complex effects induced by the winds, currents, and water-levels on the significant wave heights (SWHs). The sharp topographic gradients produce complex wind regimes must be properly modeled in order to obtain reliable simulations of both waves and currents. For this study, the wind forecasts are provided by the researchers from University of Alaska, Fairbanks (UAF), which is responsible for wind model development, implementation, improvement, and validation (Olsson et al. 2013).

As to wave-current interaction, the strong currents in CI created by tides, winds, and other mechanisms (e.g. baroclinic forcing), can influence the waves (a strong opposing current could increase the wave height and steepness). The waves, in turn, could affect the currents by transferring their momentum to the currents through gradients of radiation stress (Longuet-Higgins and Stewart 1964), Stokes drift, and modified wind stress. This dynamic feedback between the waves and the currents should thus be addressed in CI wave forecasting. While the wave-fields can be obtained using a suitable wave model, they are usually influenced by the quality of the winds and the wave open boundary conditions (WOBCs) available for a regional forecasting scheme. For developing hydrodynamic fields using a suitable circulation model, the question of efficiency (2D vs. 3D, barotropic vs. baroclinic) must be investigated, i.e. the mode in which a circulation model must run. This choice and the consequent assumptions can create inaccuracies in the results, as can the quality of the forcing functions, i.e. wind input, river discharge, none of which are accurately known.

Further, the issue of coupling the wave and circulation models must be investigated using one-way and two-way approaches. The efficiency and accuracy of both coupling approaches as well as the influence of the time interval for information exchange between the two models on the results and on modeling efficiency has to be examined. Finally, the effects of errors on the

final solution is has to be assessed. The integrated model thus consists of several components, each containing errors due to physics as well as operational constraints.

The major components of this project may be described as follows. The models used to forecast oceanic conditions consist of the Weather Research Forecasting (WRF) model for winds, the Simulating Waves in the Nearshore (SWAN) model for waves, and the Environmental Fluid Dynamics Code (EFDC) for currents and water levels. These models receive some level of input (notably, open boundary conditions) from other large-scale/global models. The integration of these models is not a trivial task, as described above, and is further complicated by the fact that not all of them are run at one location. The WRF model providing local winds for this project is operationally run at the University of Alaska and the global were model providing open boundary conditions is run at NCEP (NOAA). A considerable amount of testing and sensitivity analyses and work to identify efficient strategies for model is perforce part of this project, and this report describes these aspects at length. Subsequently, the models and information from various sources are integrated to automatically produce 36-hour forecasts once a day. Ultimately, the usefulness of any forecasting scheme will be based on how reliable the forecasts are. Unlike most efforts that show scatter and best-fit plots of model results and data, we have estimated the likelihood of a given forecasted sea-state being actually experienced.

The work described in this report has been performed by three graduate students (Dr Gaurav Singhal, Dr Abhishek Sharma, and Mr Mindo Choi) and the principal investigator. Various components of the work have appeared in a journal paper, four conference papers, and a Ph.D. thesis. (A second journal paper and another Ph.D. thesis are pending completion). Rather than refer the reader to these publications (which are provided in the Appendix), in many instances large parts of these publications are reproduced here for the reader's convenience and to provide continuity in the narrative. The layout of the report is as follows. Chapter 2 provides a description of the bathymetric and windfield datasets used in this project. Chapter 3 describes modeling methods used to estimate depth-averaged currents and water surface elevations (WSEs), as well as the establishment of two nearshore domains where flooding and drying can be important. This is followed by the simulation of wave conditions, in Chapter 4, using the SWAN model. Exploration of different ways to couple the modelled waves and currents is described in Chapter 5 with the perspective of identifying an efficient scheme. Chapter 6 provides tests of the integrated system. In Chapter 7, we describe the development of a forecast system (patterned after our previous work on Prince William Sound), and this is followed by detailed validation of the overall forecasting system using data from three satellites in Chapter 8. Chapter 9 provides conclusions of this study.

CHAPTER 2. MODEL BATHYMETRY AND WINDS

Bathymetric representation is one of the most critical aspects regarding the performance of any coastal model. Plant et al. (2009) demonstrated the influence of bathymetric filtering on modelled wave and flow fields, and found that their model results were extremely sensitive to the resolution of the input bathymetry. NOAA's National Geophysical Data Center provides various bathymetric datasets for CI such as the Etopo1/Etopo2 Global Relief Models, Tsunami Inundation Digital Elevation Model (DEM; NOAA Center for Tsunami Research), etc. The Etopo datasets have a fairly low resolution (1 min and 2 min) and do not properly resolve many complex bathymetric features of CI, while the DEM dataset is available at a 24 sec resolution, perhaps the highest resolution available for CI region. We therefore used the DEM; however, it does not cover some regions of the northern CI (especially the Turnagain Arm region). To compensate for the missing bathymetry in the Turnagain Arm region, past surveys (done by the National Ocean Service) along with the navigational charts were utilized. These data were interpolated onto the existing DEM to generate a more reliable bathymetry (a similar approach was used by Oey et al. 2007). Fig. 1.1 in the previous chapter shows the updated CI bathymetry using the DEM dataset. It is seen that, in general, the depths decrease from about 200 m near Stevenson Passage (in the south) to about 50 m in the central inlet (denoted by CCI in Fig. 1.1). The depths also show cross-shore variability in many regions. For instance, the depths decrease from over 50 m to less than 10 m across the channel near the Forelands. Overall, CI is mostly shallow with an average depth of about 50 m.

Turning to surface winds, it must be recognized that CI experiences very complex and dynamic weather patterns. During the winter season, winds in the northern Gulf of Alaska are a result of cyclonic storm systems off the Pacific and attain maximum strength from October through March (Stabeno et al. 2004). It is critical to reliably model such complex weather patterns (such as the strong gap winds; Liu et al. 2006) for forecasting purposes, since it is frequently stated that the quality of wave model predictions are most dependent on the quality of the input winds (Dykes et al. 2009). Unfortunately, there are only six weather stations (Fig. 1.1), viz. Amatuli Island (AMAA2), Augustine Island (AUGA2), Flat Island (FILA2), Drift River (DRFA2), Nikiski (NKTA2), and Anchorage (ANTA2), that provide a synoptic snapshot of wind patterns in the CI, and these are too few to obtain an accurate description of weather patterns over the entire region.

Over the last few years, NCEP's NAM ("North-American Mesoscale") model, which assimilates satellite-based measurements, has provided a synoptic snapshot of surface winds over the global ocean. However, the NAM winds do not properly account for coastal topographical variations, their resolution is much too coarse, and often the simulations do not extend into several coastal domains (e.g. CI, Prince William Sound, etc.) Since early 2007, operational weather forecasts using the WRF ("Weather Research and Forecasting") model have become available from the University of Alaska (http://aeff.uaf.alaska.edu/). These provide better coverage of the CI domain and use resolutions fine enough (~ 4 km) to resolve most of the salient features of the underlying topography. Since the WRF model is not

implemented by us at Texas A&M University, we refer the reader to Olsson et al. (2013) for details of the model. While there are some errors in the WRF predictions (described later), Singhal et al. (2010) found their effect on wave predictions to be marginal. For this study, therefore, we have used the WRF winds, obtained through the link noted above, to force the wave and circulation models. (A graphical example of such a windfield is shown in Fig. 2.1).
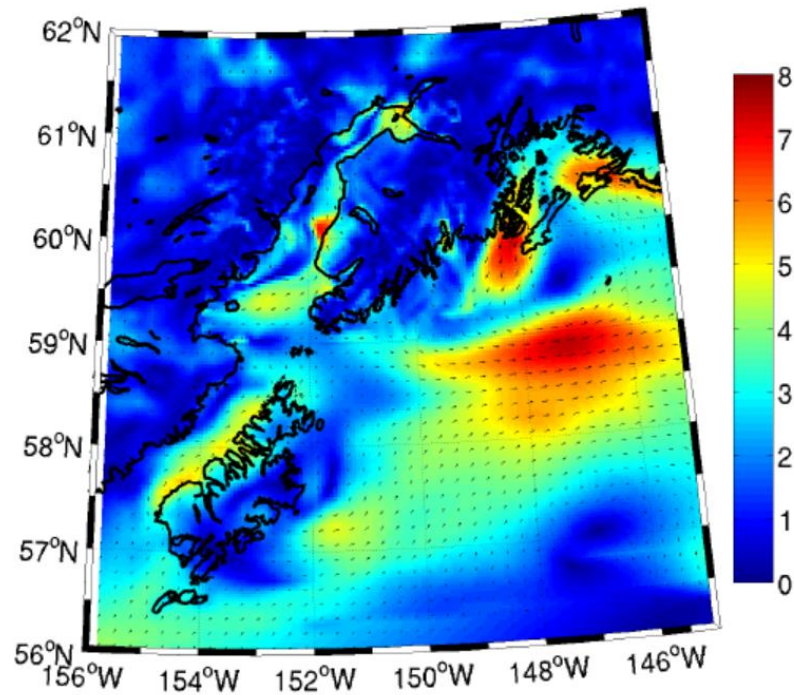
Fig. 2.1   Sample plot of WRF winds over northern Gulf of Alaska. Color represents wind speed (in m/s), and arrows depict wind direction.

Fig. 2.2 shows a sample comparison of wind speeds at various buoys and weather stations for the month of October 2008. It may be noticed that although there is significant spatial variability in the observed wind speeds, the WRF model results are generally in reasonable agreement with the measurements. The comparisons for wind directions were reasonable as well (not shown here). For some nearshore locations (e.g. AMAA2, NKTA2, ANTA2), model errors seem to be significant during some events (for instance, days 295-300 at AMAA2, day 285 at ANTA2, etc.) Although the 4 km resolution of the WRF model seems reasonable for the CI region, it may be insufficient to resolve the sharp topographical gradients near the coastline and may have resulted in these errors at the locations noted above. Clearly, though, the effect of the errors in the WRF winds on the wave-fields must be determined. This is performed in later in Chapter 6.
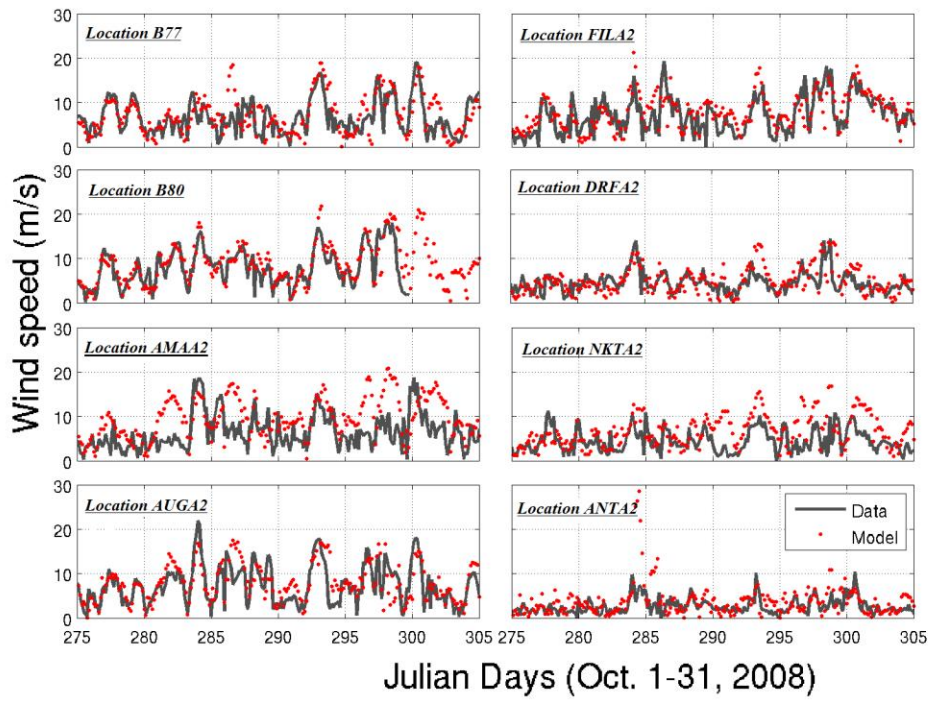
Fig. 2.2 Wind speed comparisons (After Singhal et al. 2013).

CHAPTER 3. MODELLING CIRCULATION AND WATER LEVELS

Circulation Model

The circulation in CI is mostly tidally-driven with M2 being the predominant constituent. The natural resonant frequency of CI is roughly equivalent to that of the tidal frequency, and as a result CI experiences some of the largest tidal fluctuations in the world. In addition, the tidal flow velocities intensify towards the north, with magnitudes reaching up to 3 m/sec. Okkonen and Howell (2003) suggest that wind-driven and buoyancy-driven flows also contribute to the overall +circulation patterns in CI. Tidal and baroclinic effects were also addressed in three-dimensional (3D) modeling studies by Oey et al. (2007) and Johnson (2008). Other observational studies, on the other hand, have noted that CI has a vertically well-mixed environment due to the strong tidal currents (Smith et al. 2005, Smith et al. 2010). While the aforementioned studies have addressed the circulation patterns and their seasonality in CI, how these affect the wave climate, in general, has not hitherto been examined.

For modeling, both finite-element (e.g. ADCIRC) and finite-difference (e.g. ROMS, POM, EFDC) models could be used. All these models have various capabilities and have been evaluated for numerous cases. To better describe the complex geometry, the finite-difference models were eliminated from consideration. ADCIRC, although widely used, often appears to be used in the 2D mode. We resorted to EFDC ("Environmental Fluid Dynamics Code") since it is publicly available; this advanced three-dimensional model with diverse capabilities internally links the hydrodynamic, sediment transport, water quality and eutrophication, and toxic contaminant transport (e.g. oil spill) submodels in a single source code (Hamrick 1992). Thus, EFDC has considerable advantage over other models in terms of eliminating the need for complex interfacing of multiple models to address the different processes. It can be run in barotropic or baroclinic and in 2D or 3D modes. It also has the capability of simulating wetting and drying processes (Ji et al. 2001), and has been tested and verified in a wide range of hydrodynamic and environmental studies (e.g. Kuo et al. 1996; Shen et al. 1999; Jin et al. 2001). It is thus a comprehensive circulation model, which enables us to operate it with different levels of physics to ascertain the appropriate level of effort needed for eventual wave-current modeling and forecasting.

Depth-Averaged Currents and Water Surface Elevations (WSEs) from the EFDC Model

The EFDC model was applied to the CI domain covering the region between -156º W to -149º W and 56º N to 61.5º N, on an irregular grid with a resolution of about 4 km at the open ocean boundaries, and decreasing to a resolution of ~1.5 km in the northern-most parts of CI (Fig. 3.1). Other model resolutions were also tested (e.g. <1 km) for this domain, however the model simulation time increased drastically for higher resolutions without a major impact on the accuracy of the results. Since the goal is to transition the modeling into real-time operational mode, some compromise regarding the model grid resolution is needed in order to make efficient, yet accurate, forecasts. Initially, the model was run in the depth-averaged mode,

forced by tides, winds, and river discharge in the barotropic mode with a plan to advance to higher levels of physics (e.g. 3D, salinity and density effects, etc.), if needed.

The CI circulation model was tested via the simulation of tidal conditions for May-August 2005, coinciding with NOAA's comprehensive current measurement program (http://www.tidesandcurrents.noaa.gov/). Ten locations were selected from this survey for model comparison (current meter locations are shown in Fig. 3.1.) in the lower CI (LCI) and central CI (CCI) regions (shown in Fig. 1.1; the LCI region extends approximately from 59° to 60° N, whereas CCI extends approximately from 60° to 60.75^o N). Note that NOAA installed current meters first at five locations in the CCI for about a month (late May to early July, 2005), and then moved those to the LCI for another month (July to August 2005). Modeled WSEs are also compared to data from four tidal gauges (locations shown in Fig. 3.1). The model was initiated from motionless conditions on 1 May, 2005 via prescription of tidal elevations and velocities at the open model domain boundaries (8 tidal constituents were included, viz. M2, S2, N2, K2, K1, O1, P1, and Q1). The corresponding boundary tidal elevations and velocities were extracted from TPXO6.2 global satellite-based tidal model (Egbert and Erofeeva, 2002). Further, monthly discharges from seven major rivers, as provided by US Geological Survey and Oey et al. (2007), were inputted to account for the mass introduced by the rivers into the domain. Winds from six weather stations and two NDBC buoys were also interpolated on the model grid to account for wind-driven circulation (please note that, during 2005, winds from the WRF model were not available).

Fig. 3.1 Measurement locations of buoys, tide gauges and current meters in CI. Current meters were deployed for a limited time in summer 2005. Dashed lines represent model boundaries for outer and nested grids. (After Singhal et al. 2013).

The model results for WSEs (relative to mean sea level) are shown in Fig. 3.2. In the north, the tidal range increases from about 3 m at Kodiak Island to roughly 9 m at Anchorage. It can be seen that the model captured the observed tidal variability, which is significant, at all four locations. Table 3.1 shows the overall summary of statistical estimates of best-fit slope (m) and intercept (c), correlation coefficient (R^2), and root mean square error (RMSE) for about three-month period (from 19 May – 1 August 2005) between the model and data. For the most part, the model results correlate with the data to a high degree (values of m and R^2 are in general larger than 0.88 and 0.86, respectively). Results at Anchorage, however, show a larger error compared to those at other locations; although the model predicted the tidal extremes correctly, the model results lagged the data by roughly 30 minutes. Such a lag can also be noticed in the work of Oey et al. (2007) at Nikiski; at Anchorage, however, Oey et al.'s model predicted a somewhat early arrival of tides. At any rate, lack of precision in the prediction of WSEs near Anchorage can be potentially dangerous for mariners, given the large tidal range which causes extensive wetting and drying.

Measure	Kodiak	Seldovia	Nikiski	Anchorage
m	0.91	1.01	1.05	0.88
c	0.05	0.08	-0.02	0.28
R^2	0.98	0.99	0.99	0.86
RMSE (m)	0.11	0.15	0.16	0.96
Sample size (N)	3553	3553	3553	3553

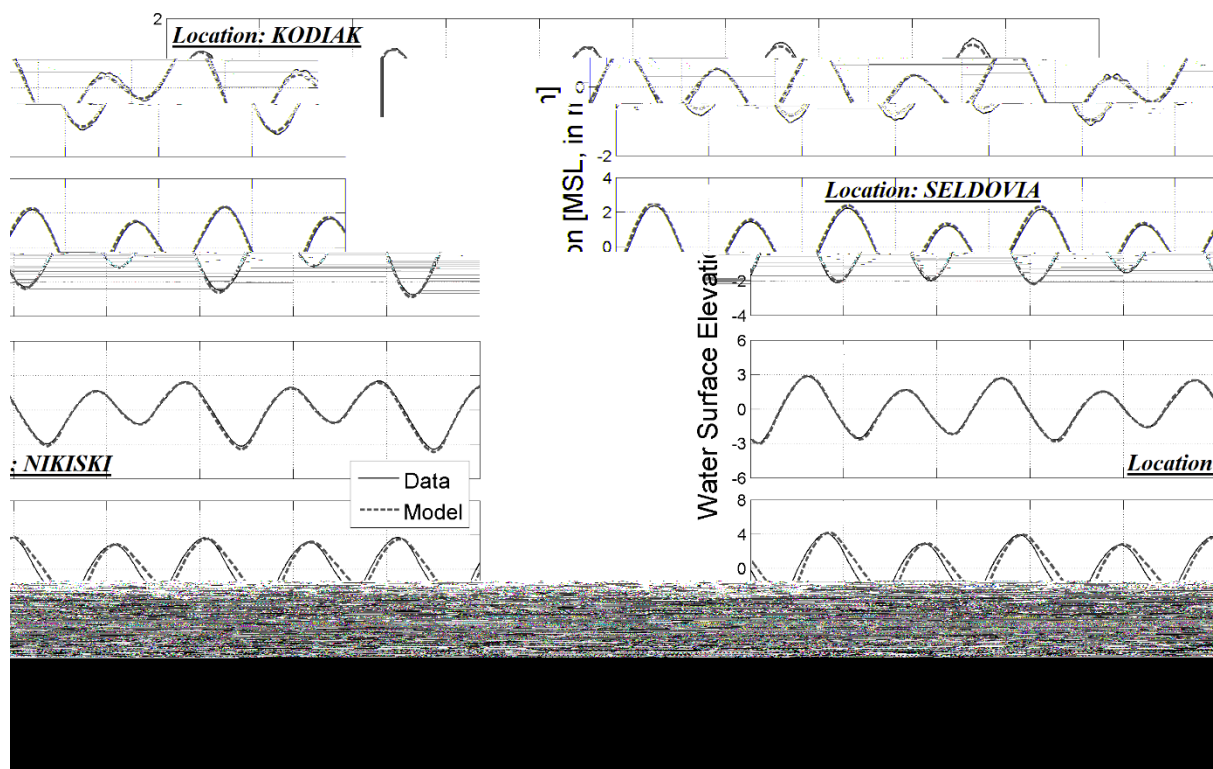**Table 3.1** Statistical comparisons of WSE for the tide gauges.

Fig. 3.2. WSE (relative to MSL) comparisons

This type of mismatch in the timing of the tides could perhaps be attributed to the resolution used. In our model implementation, the resolution is 700 m x 1400 m in the vicinity of Anchorage, which is situated in a narrow, meandering channel in Knik Arm. To examine the effect of the resolution, a nested grid with a higher resolution (300 m x 600 m) was thus constructed near Anchorage (Fig. 3.1), and was forced by the outer grid solution on its boundaries. The results for the nested grid are compared with data in Fig. 3.3, and it can be seen that the timing of the tides near Anchorage is much improved using the nested grid. Correlation estimates for the WSEs also improved significantly with $m = 0.96$, $R^2 = 0.99$, RMSE = 0.29 m.
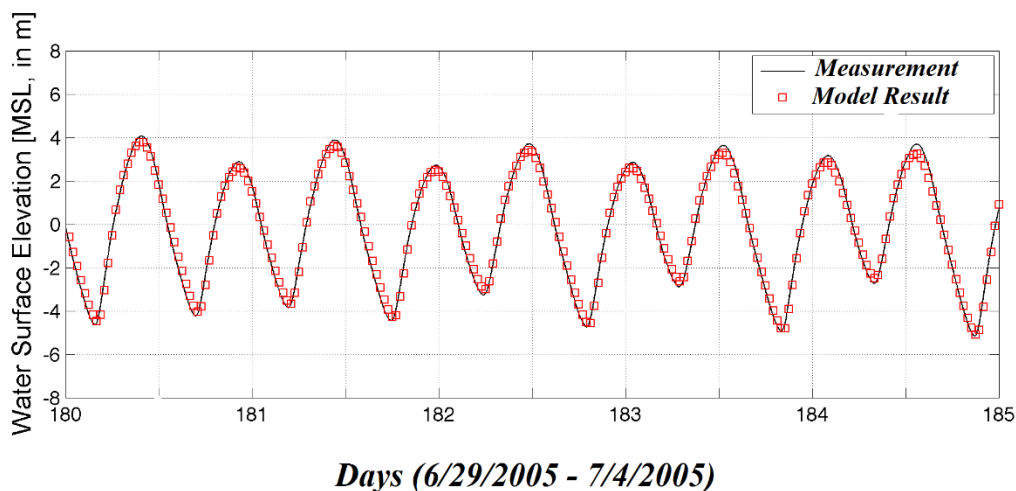
Fig. 3.3. WSE (relative to MSL) at Anchorage using the nested grid

As to flow velocities, measured flow data were depth-averaged and compared to those obtained from the EFDC model at ten locations throughout the CI (locations shown in Fig. 3.1). This analysis was performed separately for the east-west (E-W) and the north-south (N-S) flow components, since these components will be used to force the wave model (discussed in Chapter 5). The data summarized at the top of Tables 3.2 and 3.3 show that, in general, the range of velocities are higher in the CCI (1-3 m/s) compared to those in the LCI (0.2-1.5 m/s), with the N-S component usually being more dominant than the E-W component in the CCI. The model captures this variability and in general shows a high correlation with data ($R^2 \geq 0.86$, $0.74 \leq m \leq 1.06$, RMSE≤ 0.19). Although there are some errors in the model results (which may be due to baroclinic effects which were not included or inaccuracies in the input winds), it is encouraging that the 2D EFDC model has yielded such a high degree of match, and it would appear that accounting for additional physics may not be warranted. Yet, a further explanation of the effects of possible residual/random errors on the wave-field is described in Chapter 6.

Measure	Forelands (1)		South of West Forelands (2)		Drift river (3)		East of Kalgin Island (4)		South-east of Kalgin Island (5)	
	E-W	N-S	E-W	N-S	E-W	N-S	E-W	N-S	E-W	N-S
Data (m/s) (min, max)	(-0.89, 0.64)	(-2.12, 2.32)	(-1.66, 1.69)	(-1.34, 1.02)	(-1.08, 1.02)	(-0.98, 1.00)	(-0.65, 0.86)	(-2.85, 2.11)	(-0.89, 0.94)	(-1.87, 1.47)
Model (m/s) (min, max)	(-0.99, 0.60)	(-2.16, 2.64)	(-1.75, 1.68)	(-1.44, 1.23)	(-0.84, 1.10)	(-0.64, 1.03)	(-0.9, 0.67)	(-3.04, 2.19)	(-1.13, 0.89)	(-2.01, 1.61)
m	0.97	0.94	0.98	1.06	0.91	0.77	0.99	0.96	0.97	0.95
c	0.01	0.02	0.07	0.04	0.06	0.03	-0.08	0.03	-0.09	0.03
R^2	0.86	0.98	0.96	0.97	0.95	0.94	0.94	0.99	0.96	0.98
RMSE (m/s)	0.15	0.19	0.19	0.12	0.11	0.10	0.09	0.09	0.08	0.13
Sample size (N)	1489		1485		1530		1498		1503	

Table 3.2 Depth-averaged flow velocity comparisons, for locations in the CCI. Numbers in parentheses show minimum and maximum values for depth-averaged flow velocity components.

Measure	West of Cape Ninilchik (6)		Augustine Island (7)		West of Kachemak Bay (8)		Seldovia (9)		Stevenson Passage (10)	
	E-W	N-S	E-W	N-S	E-W	N-S	E-W	N-S	E-W	N-S
Data (m/s) (min, max)	(-1.25, 0.82)	(-1.92, 1.49)	(-0.44, 0.23)	(-0.92, 0.70)	(-0.33, 0.26)	(-1.19, 1.22)	(-0.68, 1.01)	(-0.44, 0.64)	(-1.25, 1.13)	(-0.35, 0.81)
Model (m/s) (min, max)	(-1.21, 0.70)	(-1.94, 1.46)	(-0.36, 0.24)	(-0.92, 0.72)	(-0.24, 0.18)	(-1.31, 1.21)	(-0.75, 0.74)	(-0.48, 0.41)	(-1.15, 1.02)	(-0.63, 0.63)
m	0.89	0.96	0.89	0.98	0.74	1.01	0.95	0.94	0.92	0.95
c	-0.08	-0.08	0.003	-0.01	-0.01	-0.04	-0.05	-0.04	0.06	-0.14
R^2	0.96	0.98	0.87	0.95	0.75	0.99	0.89	0.92	0.91	0.87
RMSE (m/s)	0.08	0.11	0.05	0.07	0.05	0.06	0.10	0.06	0.12	0.08
Sample size (N)	1441		1418		1412		1486		1448	

Table 3.3 Depth-averaged flow velocity comparisons, for locations in LCI. Numbers in parentheses show minimum and maximum values for depth-averaged flow velocity components

### *Nested Domains: Modeling Flooding and Drying*

In order to obtain reliable simulations, some aspects need special attention (such as the need for very high resolution, adjustments to wave spectral frequencies while simulating waves (discussed later in Chapter 4), modeling flooding and drying, etc.), and, for operational forecasting, the best approach is to create separate coupled (nested) subdomains. The phenomenon of flooding and drying is particularly important in many regions of Cook Inlet, since tidal fluctuations (and currents) are high, and a wave model that disregards the changing water-levels may end up providing wave forecasts that disregard the modifications due to currents, or worse, providing wave forecasts for regions from where the water has ebbed. We therefore created two local sub-domains, Kachemak Bay (KB) and the Anchorage area (Fig.

3.4). These models were driven by the solutions of the low-resolution outer grid CI models on the boundaries.
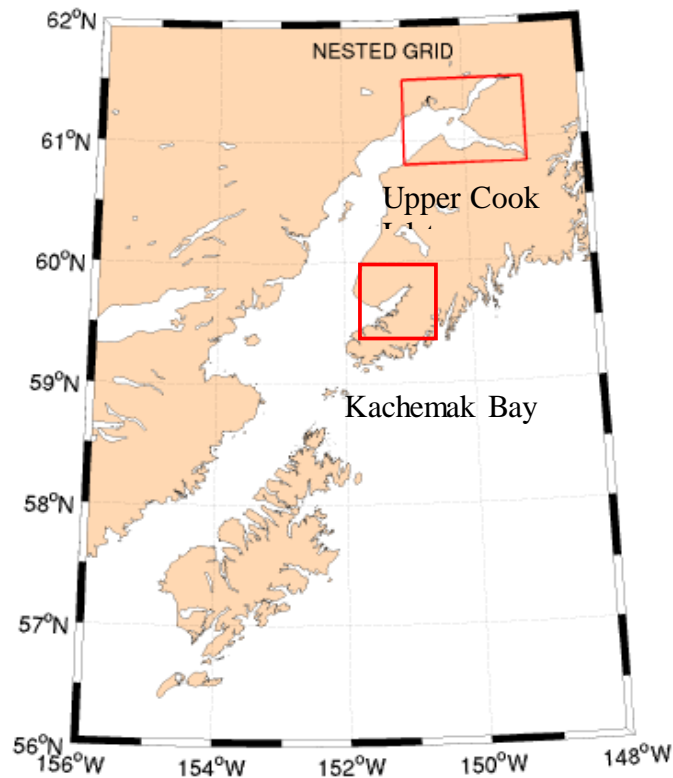

Fig. 3.4 Overall Cook Inlet, and the nested Kachemak Bay (KB) and Upper Cook Inlet (UCI) domains.

As seen in the NOAA navigational charts (Fig. 3.5), in Kachemak Bay, the entire western shoreline as well as the extreme north-eastern parts of the "inner" bay become dry during low water (green-shaded area in Fig. 3.5). A large area in the vicinity of Anchorage also becomes exposed during low water conditions. The true color and Landsat TM images obtained using data from the Terra (MODIS) satellite are shown in Fig. 3.6 for the UCI (Anchorage area) domain for high and low tide conditions. The time-dependency of the water level changes is obvious, and it is to be noted that the Anchorage Daily News has reported several incidents pertaining to boat groundings in this area. It is obviously critical to accurately predict the extent of such regions to aid navigation.
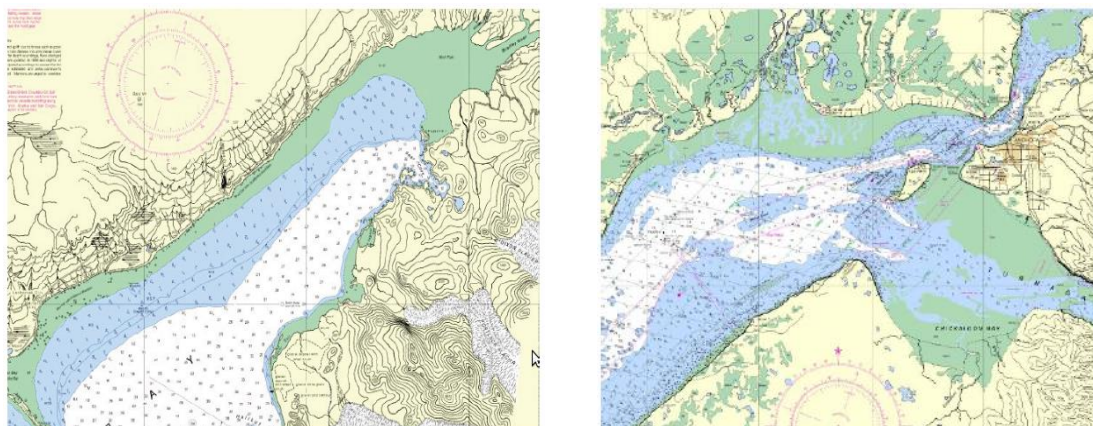
Fig. 3.5 Map of KB (left) and UCI (right) showing the extent of dry regions, which are depicted by the green shaded area (source: NOAA).
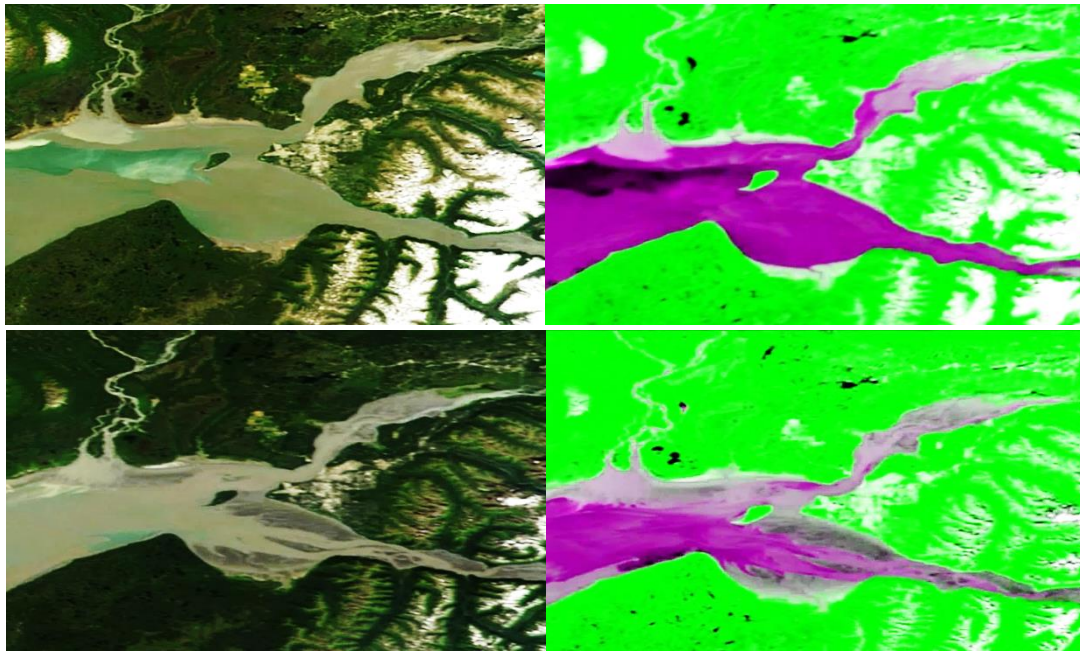
Fig. 3.6 High tide event (top panel) and low tide event (bottom panel). True color satellite images (left) and Landsat TM images (right) for UCI region.

In the circulation model, for each time-step, the model checks the total depth (H) against the drying depth (HDRY) at each grid point. If H <HDRY at a grid point, then the model assumes that point to be "dry" (although a thin film of water remains at that grid point for continuity). The flow velocities for "dry" grid points are then set to zero. It is necessary to identify this parameter HDRY properly, and then to validate the results, at least qualitatively (since no quantitative data are available).

Three representative drying depths HDRY, viz. 10 cm, 20 cm, and 50 cm, were chosen to model the extent of dry regions. Fig. 3.7 shows the snapshot of modeled total depth in Kachemak Bay during the time when water level at Seldovia was lowest (inset of Fig. 3.7a). While all three chosen values of drying depths seem to show some drying, simulations performed using HDRY=50 cm (Fig. 3.7c) predicted the extent of "dry" regions that closely matched those shown in Fig. 3.5.
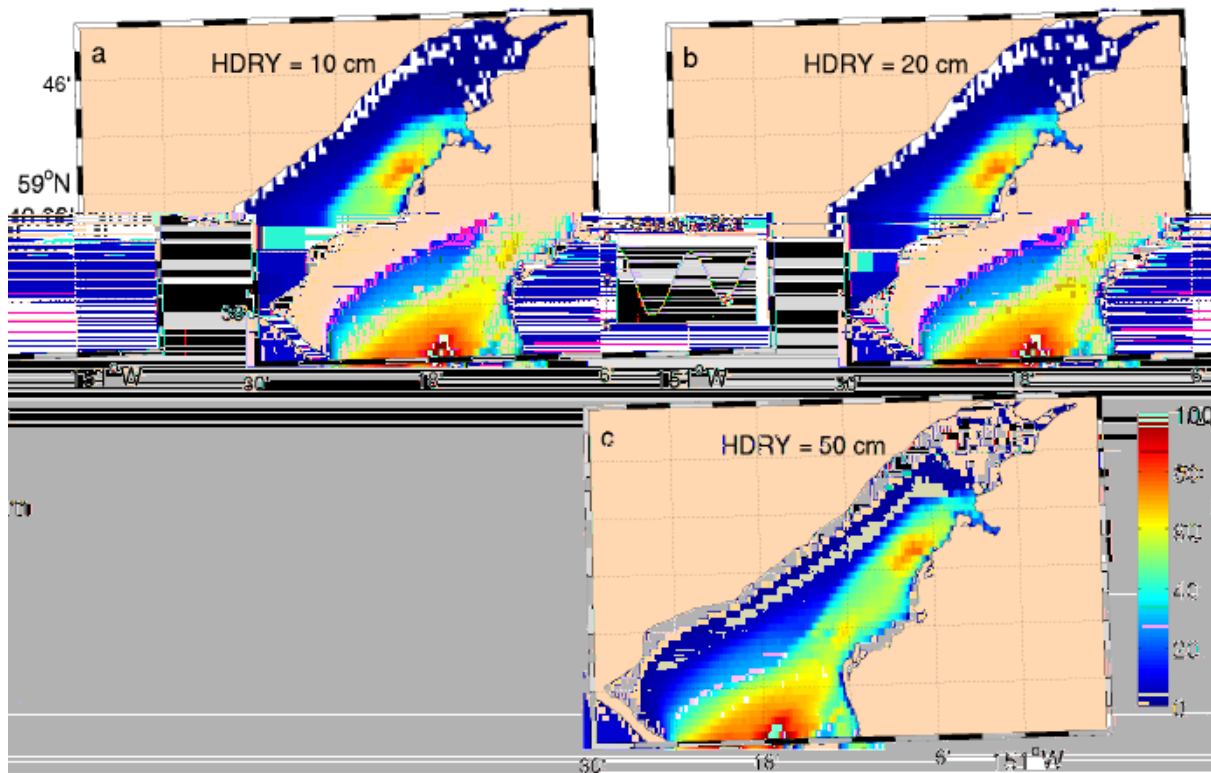
Fig. 3.7 Sensitivity of modeled dry regions (shown by white spaces) to drying depth. Inset in (a) shows measured (blue line) and modeled (red circle) WSE at Seldovia during the snapshot.

A similar study was conducted for the coastal area near Anchorage. A fine grid with resolution of 24 seconds was constructed and this model was initialized using boundary conditions from the outer coarser (CI) grid. The nested grid solution was then checked for its capability in simulating the extent of "dry" regions. A large area in the vicinity of Anchorage becomes exposed during low water conditions (green-shaded area in Fig. 3.5). Fig. 3.8 shows the model-predicted instantaneous total water depth during low water conditions (inset of Fig. 3.8). It can be clearly seen that the model-predicted "dry" regions (white patches in Fig. 3.8) are qualitatively similar to those shown in the NOAA navigational chart (Fig. 3.5).
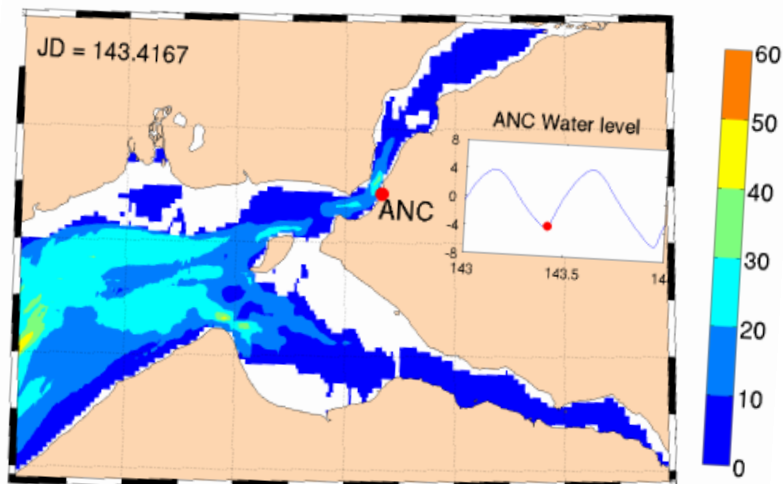

Fig. 3.8 Model-predicted instantaneous total water depth for the same region as in Fig. 3.5. White patches depict "dry" regions, whereas inset shows measured (blue) and instantaneous model-predicted (red circle) WSE at Anchorage.

15

Influence of different forcing mechanisms

Currents, and hence the waves, are affected by several forcing functions, typically, tides, winds, and river discharge. It is difficult to include all effects in a forecasting scheme, unless it is absolutely necessary. Some effort was directed towards determining which forcing mechanisms are dominant and should be included in the circulation model. For example, how significantly does the wind forcing affect the flow field? In many regions, tides are dominant and including winds, if their effect is comparatively small, impedes forecasting efficiency.

Fig. 3.9 shows a sample plot to explain the contribution of tides, winds and river discharge in Kachemak Bay. It can be seen that the tides and winds may have an impact over a large area, whereas the effects of river discharge is usually local.
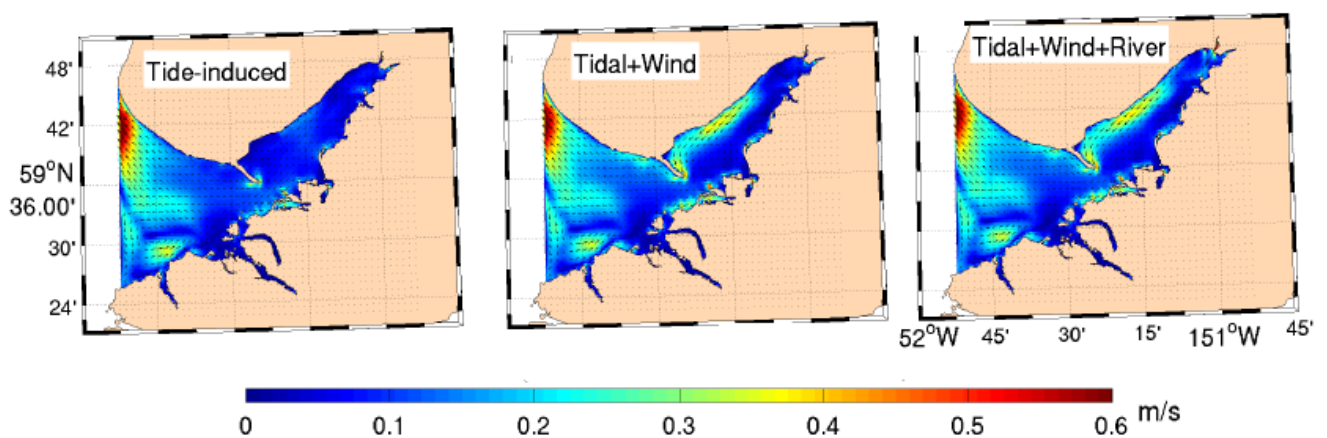
Fig. 3.9. Modeled flow-field, and the contribution from different forcing mechanisms

The tide-induced currents seem to be stronger in the "outer" bay and ranged between 0.5-0.6 m/s, while the wind-induced currents, during this snapshot, were stronger along the western shoreline of the "inner" bay and ranged between 0.2-0.3 m/s.

Summary

The results shown above indicate that the depth-averaged EFDC model provided reliable predictions of water-levels and circulation patterns in CI. The water levels were predicted with high accuracy at Kodiak, Seldovia, and Nikiski ($R^2 > 0.98$); near Anchorage a finer grid was required to obtain a good match with data and, in particular, to properly predict the tidal phases. The depth-averaged flow velocities were also predicted with high accuracy ($m > 0.74$, $R^2 > 0.86$) throughout the CI, thereby suggesting that the 2D model is sufficient and accounting for additional physics may not be warranted for forecasting purposes. (We did perform baroclinic simulations with multiple levels, but ruled out this option since the differences in the results did not justify the additional computational time and effort). Results for the two subdomains (Upper Cook Inlet cobering the Anchorage area) and Kachemak Bay suggest that flooding and drying is reproduced in a manner that bears considerable resemblance to NOAA charts and satellite images.

CHAPTER 4. MODELLING WAVES

Wave Model

Due to the presence of dynamic and energetic local weather systems, waves in the northern Gulf of Alaska are among the largest in the world with SWHs frequently exceeding 5m during the winter season. Thus, it is critical to predict such extreme events accurately in order to support the various maritime activities. NCEP provides continuous 7-day wave forecasts for the CI region using the multi-grid version of WAVEWATCH III model (hereafter, WW3; Tolman 2009) on a spatial resolution of about 7 km. The NCEP wave forecasts, however, utilize the NAM winds which, as noted earlier, are much too coarse to properly account for the local topographical features. In addition, the NCEP wave forecasts do not include the effects of currents, which may also have a significant effect on surface waves.

Clearly, the CI wave model should account for such complexities in order to obtain reliable estimates of wave parameters. For this purpose, the SWAN model (version 40.81) was utilized. The model has been widely used for hindcasting and forecasting purposes (e.g. Allard et al. 2008, Singhal et al. 2010). Details of the SWAN model have been described in Booij et al. (1999), Ris et al. (1999), and elsewhere, and thus are not included here. Briefly, SWAN is a third generation wave model specifically designed for simulation of waves in coastal waters and accommodates wind-induced wave generation, energy transfer due to quadruplet and triad wave-wave interaction, and dissipation due to breaking and bottom friction. Significantly, the model can accept current fields produced by the circulation model and hence can incorporate the effects of wave-current interaction. The model is widely used for various applications such as siting aquaculture operations (Panchang et al. 2008) and offshore oil platforms (Panchang et al. 2013), wave forecasting (Singhal et al. 2010), etc.

Model Application and Preliminary Validation

The SWAN wave model covered the same region as the circulation model, but at a resolution of about 1.5 km throughout the domain. SWAN was set up using the default options for wave generation (wind growth, quadruplet, and triad wave-wave interactions), wave breaking, bottom friction, etc. A model time-step of 15 min was initially used. For the overall grid, we use a frequency range of approximately 0.04-0.50 Hz with 24 frequency bins. The wave model was forced by the WRF model that provided the output of winds every hour at a resolution of ~4 km. The WOBCs were obtained from the global WW3 model at the locations of Buoy 46078 (hereafter, B78) and Buoy 46080 (hereafter, B80), shown in Fig. 3.1. The full spectral output at B80 was forced along the east boundary, while the output at B78 was used to force the south boundary. Since the WW3 model, at present, does not provide full spectral output at locations near the west boundary, the output at B78 was also assumed along the west boundary (the validity of this assumption is discussed in Chapter 6).

Sample results obtained using the above model configuration are compared with buoy measurements for B05 and Buoy 46106 (B06) for a 12-day period in November 2008 (Fig.

4.1). The wave model, in general, seems to capture the variability in the SWHs, although there are some errors which may be due to inaccuracies in the winds and WOBCs. In addition, there may be some effect due to the water-level fluctuations and/or currents; the result obtained using the coupled version "C1W-1h" is also shown in Fig. 4.1 (red line), however, this is discussed later in Chapter 6.
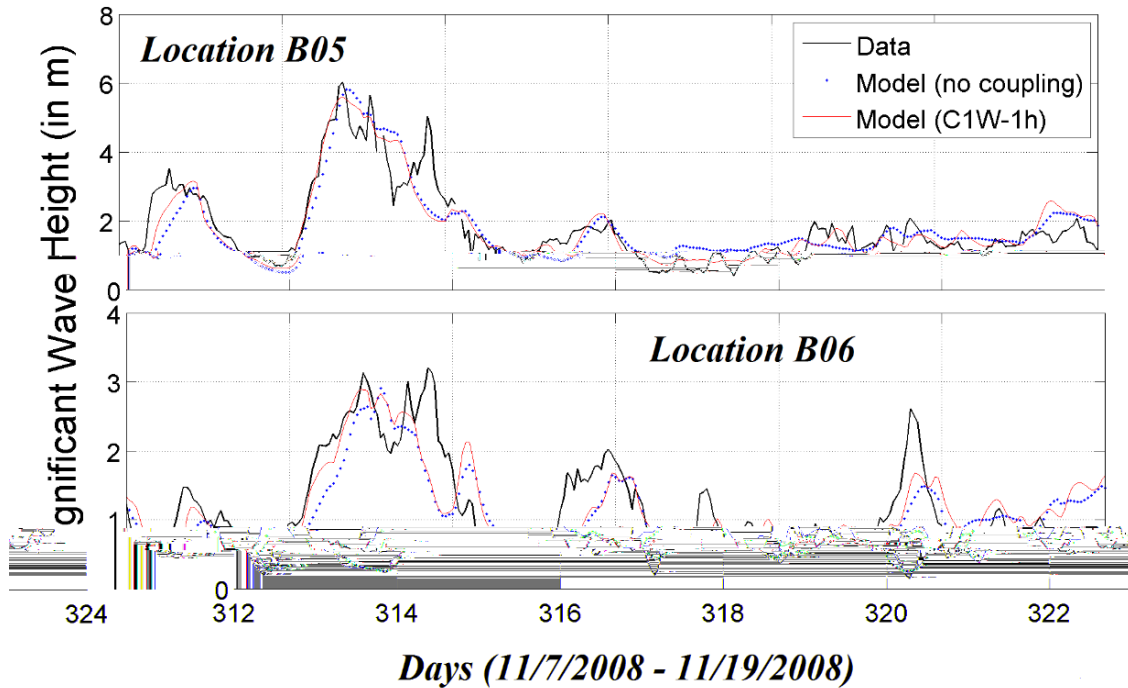

Fig. 4.1 Sample SWH comparisons at (a) B05 and (b) B06.

While the overall results, as seen in Fig. 4.1, appear reasonable in the central areas, the effect of grid resolution and frequencies to be modelled and their resolution must be examined in nearshore areas. We attempted to address these issues by performing several simulations using the wave and circulation models in the KB region. (For convenience and brevity, we describe here the wave model results obtained after coupling with the currents. The coupling is described in Chapter 5). Two model domains, an inner grid with a fine resolution (~200 m) and an outer grid with a coarse resolution (~1000 m), were used for this investigation (Fig. 4.2).
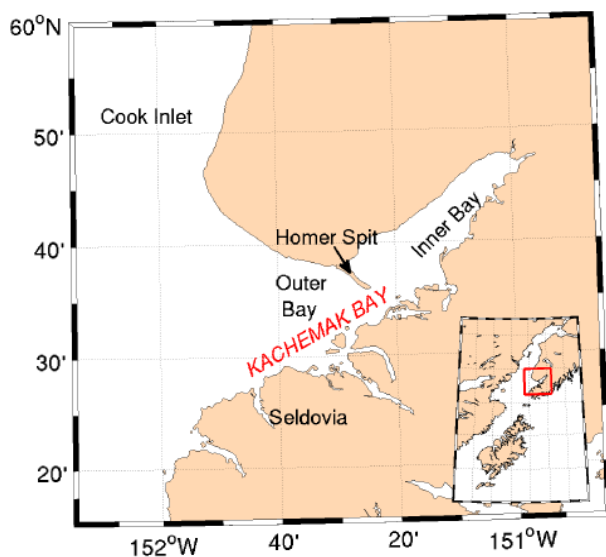
**Fig. 4.2** KB domain for coupled wave-current model

18

An example snapshot of modelled SWHs is shown in Fig. 4.3 which compares the performance of the coarse and nested grids (based on Fig. 4.2) for the KB region. For the most part, the results from both the grids are reasonably consistent with each other in the "outer" bay region (the western part of the bay). This is encouraging as the resolution used for the outer grid (1 km) was 5 times that for nested KB grid size (200 m). However, the differences are more pronounced in the "inner" bay region, and in addition, the outer grid does not resolve the coastal features properly, especially Homer Spit and the western shoreline of the 'inner" bay. Overall, it seems that the fine grid captures the shoreline variations better compared to the coarse outer grid. Thus, to properly simulate KB, the fine grid used here may be appropriate.
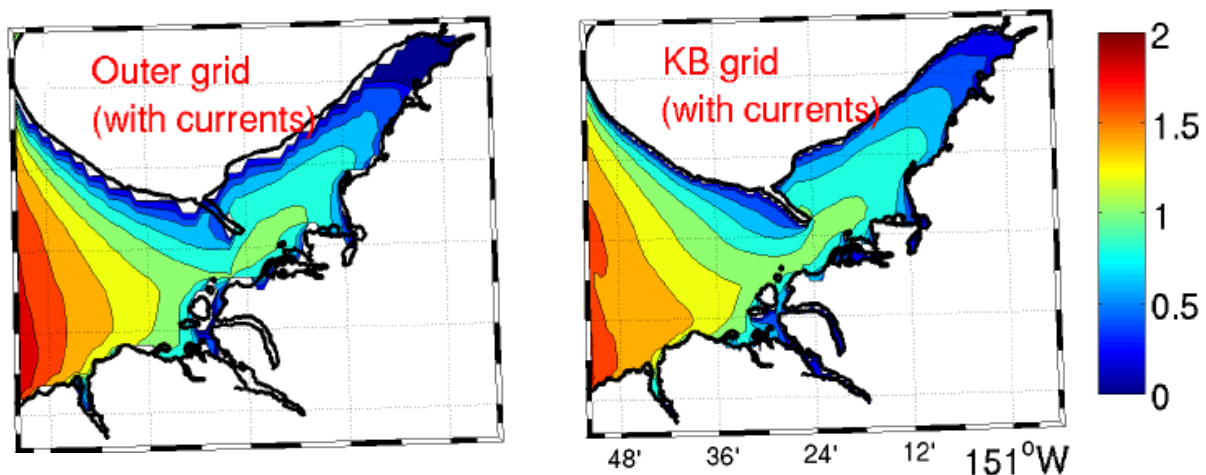

Fig. 4.3 Effect of grid resolution; SWHs obtained using a coarser grid (left) and a finer grid (right)

Turning to spectral frequencies, there is a question of what wave frequency range and spectral resolution should be used if the region experiences locally generated wind-seas. This issue becomes important because CI is a large domain and wave characteristics can vary in different parts of the domain. Nearshore areas may possibly be characterized by small period waves much of the time. For the overall grid, as noted earlier, we use a frequency range of approximately 0.04-0.50 Hz, but the resolution may not suffice for bay-scale local generation. The impact of spectral resolution on SWHs was studied using the fine grid (*vide supra*). This was done to check the model sensitivity to short- and long-period seas, and to see the effect of spectral resolution on SWHs. Two comparisons were considered:

(1) Two different frequency ranges, 0.04-0.5 Hz and 0.04-1.0 Hz were considered. The effect of varying the frequency range is shown in Fig. 4.4.
(2) The frequency range of 0.04-1.0 Hz was divided first into 24 frequency components, and then into 48 components. The effect of spectral grid resolution is shown in Fig. 4.5.
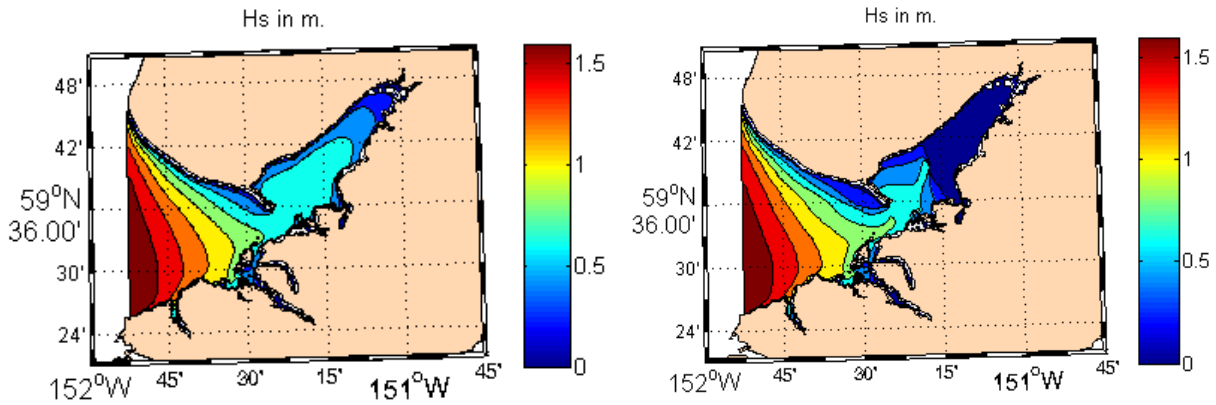
Fig. 4.4 Effect of frequency range; SWHs using frequency range of 0.04-1.0 Hz (left) and 0.04-0.5Hz (right)
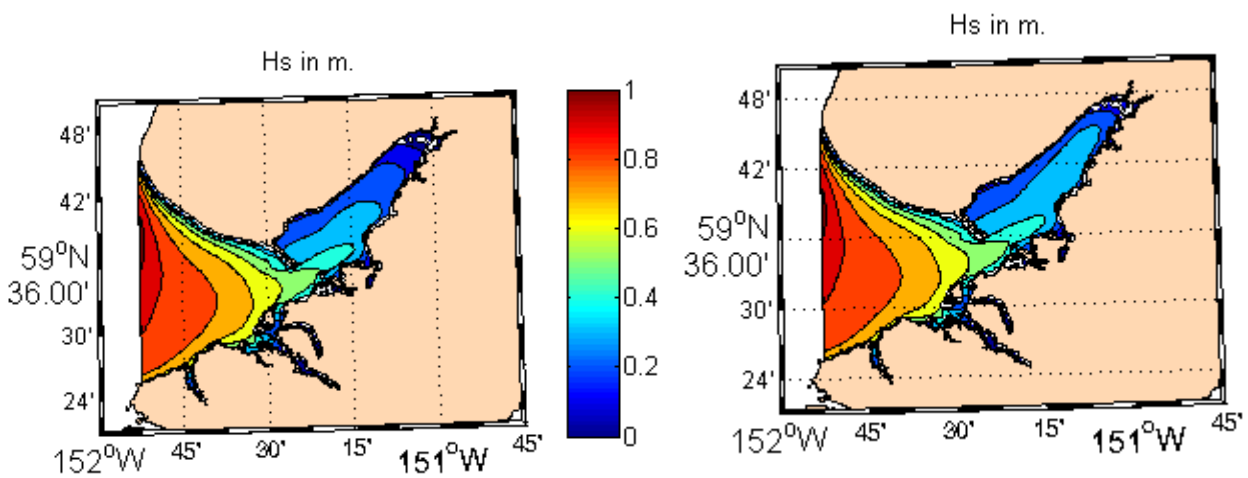
Fig. 4.5 Effect of frequency resolution; SWHs using 24 components (left) and 48 components (right)

It can be seen in Fig. 4.4 that the "inner" bay shows wave development further to the east when higher frequencies were included in the wave modeling, and differences of up to 0.5 m can be found. This indicates that the "inner" bay may be dominated by winds that are locally-generated. It can be concluded from Fig. 4.5 that to accurately model the SWHs inside the "inner" bay, a finer spectral resolution is preferable for forecasting. In summary, based on these example results, we may conclude that the coarse resolution of the outer grid, along with the insufficient spectral frequency resolution, can influence the accuracy of model results in the "inner" bay.

The above paragraphs have described the essential features of the wave model. As seen in later chapters, the model will be forced not merely by the winds and open ocean wave conditions obtained from NOAA's WAVEWATCH model, but also by currents. There remain other issues such as the effect of certain unknowns in the open boundary conditions, errors in the windfields, etc. Rather than discuss them individually, it is more efficient to examine these in the context of the integrated wind-current-wave model system since that is what will be ultimately implemented. Hence these issues are relegated to a later chapter.

CHAPTER 5. MODELLING WAVE-CURRENT INTERACTION

## *Coupling the Wave and Circulation Models*

To study the effects of wave-current interaction, considerable effort was directed towards coupling the wave and circulation models. In certain regions of CI (e.g. near the Forelands), the surface-currents were found to be quite strong (2-3 m/s) and they can hence influence the local wave climate. Under certain wave conditions, the wave-induced radiation stresses contribute to the currents, and must be included as input to the circulation model. Thus it becomes necessary to develop a methodology for coupling the wave and circulation models in order to account for these dynamic processes. In our work, a stand-alone interface, written in Shell scripting language, was developed in order to initiate the cross-talk between the models at appropriate time-steps.

Coupling between the wave and circulation models could be performed two ways - 1) Offline coupling, and 2) Online coupling. In general, offline coupling entails running the two models separately (in no particular order) for the entire duration of simulation (e.g. two days). The information can then either be transferred from one model to the other model (one-way approach; Fig. 5.1), or it could be exchanged among both the models (two-way approach; Fig. 5.2). In the one-way approach, the second model is executed using the output of the first model (Fig. 5.1), whereas the two-way approach requires both models to be executed multiple times, while exchanging information, until the solution is converged (Fig. 5.2). Online coupling, in contrast, invokes both models simultaneously. After a suitable time interval (e.g. three hours), the two models exchange information and continue the simulation until the next communication time step (Fig. 5.3). This technique avoids the use of multiple iterations as there is dynamic exchange of information among the two models during the simulation process. However, in between two information exchange time-steps, the conditions are assumed steady. In contrast, in the one-way approach, the required information at all time-steps from the other model is pre-calculated. Thus there are advantages and disadvantages associated with both the methods and the effects of these on the model accuracy and efficiency must be investigated.
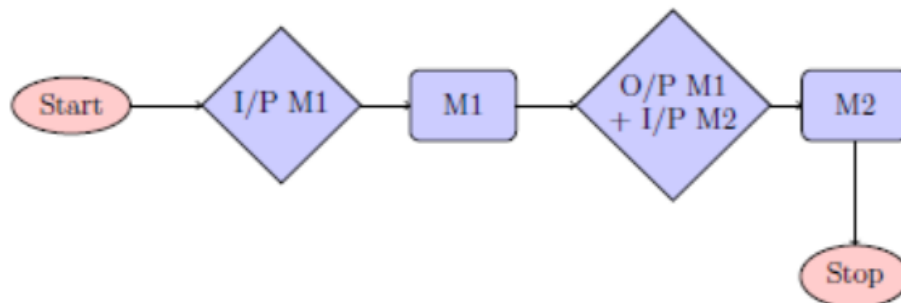
Fig. 5.1 Offline coupling with one-way approach. M1 represents Model 1, whereas M2 represents Model 2. I/P is input, O/P is output.
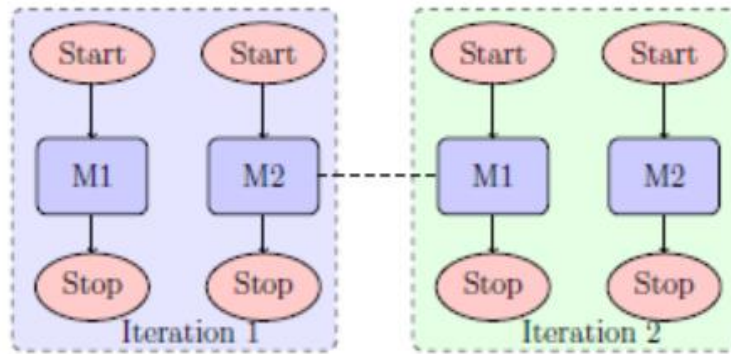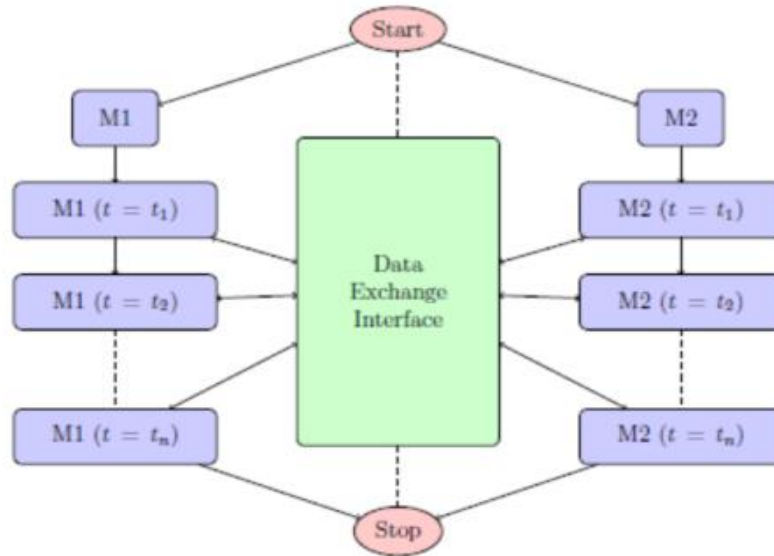
Fig. 5.2 Same as Fig. 5.1, but with two-way approach involving two iterations.

In the context of the present work, the coupling of SWAN and EFDC was performed on a Macintosh computer with Quad-core processor (with hyper-threading) and 16 GB RAM. SWAN can run in parallel mode for multi-processor systems, whereas EFDC is only capable of running in serial mode. In this study, we have used the one-way off-line coupling (hereafter, C1W) and the two-way on-line coupling (hereafter, C2W). The purpose of using the two methods is to compare the wave model results with and without any coupling, and to address the question of which method is more efficient for forecasting purposes.

In the one-way approach, the simulation is started with EFDC which provides, by way of output, WSEs and flow velocities. SWAN is then initiated with the EFDC output along with the other forcing terms (winds, WOBCs, etc.). For the on-line coupling, a simple interface was built using the shell scripting language, as stated earlier. This interface controlled the execution of both the models simultaneously: starting from t = 0, each model advances to the so-called "information exchange" time step when the models are stopped momentarily to exchange information (gradients of radiation stresses are transferred from SWAN to EFDC, whereas WSEs and flow velocities are transferred from EFDC to SWAN), after which the models continue the simulation until the next "information exchange" time-step, and so on. Thus, each model has information about the other model after each exchange, which is assumed steady until the next exchange. The results from the two coupling methods are compared to the results without coupling using two information exchange time-steps (1h, 3h); these model runs are named C1W-1h, C1W-3h, C2W-1h, and C2W-3h in the following discussion.

Fig. 5.3 Online coupling of two models

To examine the performance of these coupling methods, the integrated wind-wave-current forecasting scheme was implemented for a 12-day period in October 2008, which consisted of four distinct storm events (denoted by E1, E2, E3, E4 in Fig. 5.4). The measured wind and wave conditions during these events near B05 are shown in Fig. 5.4. Figs. 5.4*a* and Fig. 5.4*b* show SWH and mean wave direction, respectively, and Fig. 5.4c shows wind speed and direction measured at AUGA2 (a weather station 40 nm north-west of B05 shown in Fig. 1.1; B05 is not equipped with an anemometer for measuring wind velocities). The large waves with SWH ~ 5 m during E2 and E3 appear to be coming from the west (Fig. 5.4b), which is consistent with the dominant wind direction (Fig. 5.4c red line). On the contrary, waves during E4 appear to be coming from the east-south-east direction (i.e. from Gulf of Alaska). Waves during E1 exhibit greater variability and are northerly for the most part. Although the SWHs for all the events are quite large, they may be generated by different physical mechanisms (e.g. local winds funneled by the surrounding Chugach Mountains and swells from Gulf of Alaska). In summary, these events were selected because of (1) the magnitude of these events (i.e. SWHs > 4m); (2) their distinct characteristics discussed above; (3) the availability of buoy measurements to guide the model development and validation; and (4) their potential to serve as benchmarks for quantifying modeling errors for future events.
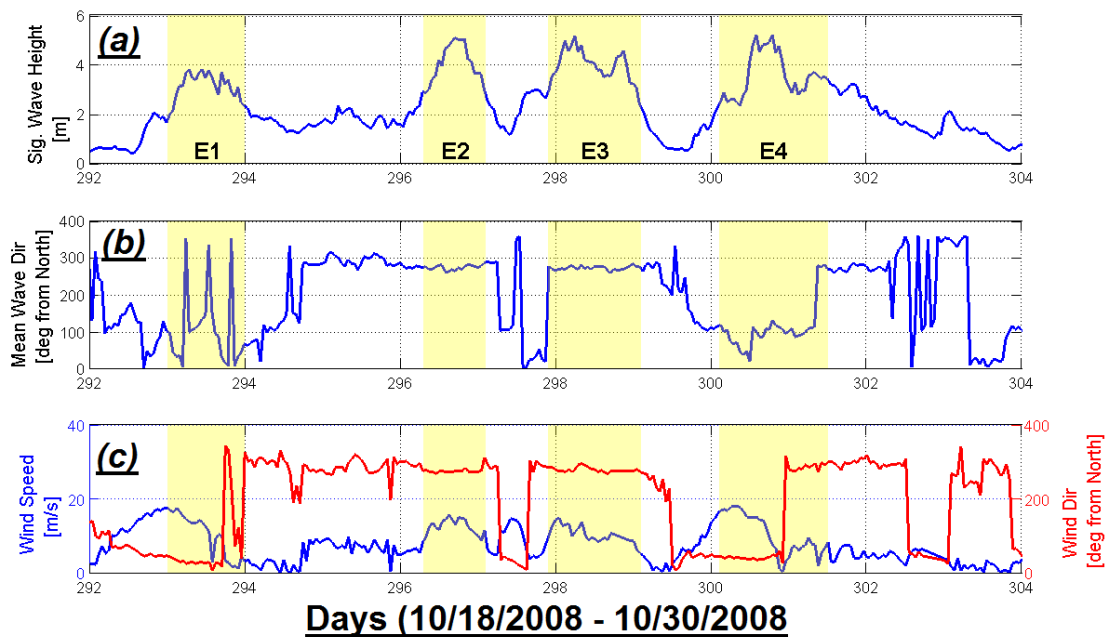
Fig. 5.4 (a) SWH and (b) mean wave direction (degrees from north, clockwise) measured at B05. (c) wind speed (blue line) and direction (red line) measured at AUGA2. (after Singhal et al. (2013)).
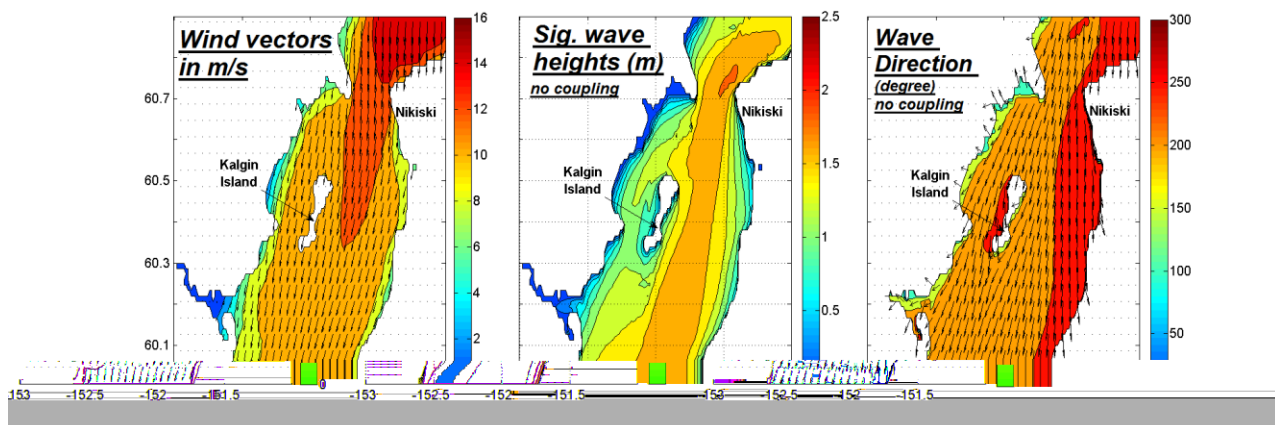
Our first task is to qualitatively explore the details of model results and modeling efficiency when different coupling methods are used. A snapshot of the modeled wind and "background" wave conditions (with no currents) during event E4 (day 301.0417, i.e. 1 AM on 27 October 2008 UTC) is shown in Fig. 5.5 for the CCI region. The winds and waves during this time were mostly southward with wind speeds ~ 12 – 14 m/s and the modeled SWH ~ 1.5 – 2 m.

For wave-current interaction, the two coupling methods (i.e. C1W and C2W) were implemented using 1h and 3h updating intervals. Fig. 5.6 shows a combined plot of wave and current conditions, outputted from the SWAN model, on day 301.0417 (same time as Fig. 5.5). For C1W-1h, the flow-field (which is largely tidal) was inputted to the wave model every hour; this yields a resolution of about 12 points per tidal cycle which may be considered to be reasonably accurate. In this case, the current direction is northward (opposite to the wind/wave direction) with a maximum speed of about 1.3 m/s near the Forelands, whereas to the south of Kalgin Island, currents are directed southward (same as the wind/wave direction) with speeds about 1 m/s (Fig. 5.6*a*). The opposite current directions are indicative of tide reversal during this time instant. The result in C1W-3h (Fig. 5.6*b*), with an updating resolution of about 4 points per tidal cycle, is fairly similar to Fig. 5.6*a* but the peak velocities near the Forelands are different by ~0.3 m/s, since the flow-field at this instant (i.e. day 301.0417) is obtained by interpolation between days 301 and 301.125 (3-h period). The C2W simulations contain more physics (owing to the effect of the waves being accounted for in the currents) and are hence more time-intensive relative to the C1W simulations. In C2W-1h (Fig. 5.6*c*), the flow-fields were updated on day 301.0417 and are mostly similar to those shown in C1W-1h. However, in the case of C2W-3h (Fig. 5.6*d*), the updating interval has a much greater effect because the

24

flow-field taken from the previous updating time instant (i.e. on day 301) is assumed to be constant for the next three hours (i.e. day 301.125) in the wave model. As a result, C2W simulations (Fig. 5.6*d*) show current-fields from the previous updating time instant (i.e. day 301), which are propagating northward in the entire domain, and are larger in magnitude (compared to those shown in C1W and C2W-1h simulations) with maximum speeds of about 2 m/s (indicative of a flooding tide). Looking at the overall results, it would appear that the C2W-3h diverges from the other solutions; the similarity of C2W-1h with C1W simulations would suggest that the effect of waves on the flow-fields is marginal.

Compared to the SWHs obtained without any coupling (Fig. 5.5), the SWHs obtained using C1W simulations (Figs. 5.6 *e, f*) are about 0.3-0.4 m higher near the Forelands due to the effect from the opposing current. South of Kalgin Island, however, the SWHs increase by about 0.2 m with C1W-1h (Fig. 5.6*e*), and by about 0.3 m with C1W-3h (Fig. 5.6*f*). These differences in the SWHs with C1W simulations (Figs. 5.6*e, f*) are related to 1h vs. 3h interpolation of flow-fields in the wave model. SWHs obtained using C2W simulations (Figs. 5.6*g, h*), on the other hand, seem to be about 0.1-0.2 m higher than C1W, and about 0.5 m higher compared to no coupling. As explained above, these differences are due to the differences in current-fields between C1W and C2W simulations. In general, these results, which are qualitatively consistent with our expectations given the directions of the waves and currents, inspire confidence in the used modeling scheme.

Overall, the differences in the SWHs (~ 0.5 m) with and without coupling clearly indicate that some level of coupling (one-way or two-way) is necessary in the CI region. Since the effect of waves on currents was found to be marginal, the C2W approach may not be warranted. Also, as discussed above, a smaller updating time step may be required (1h or less) to better resolve the tidal fluctuations. With regard to the efficiency of the system, it was found that the C1W approach is more efficient compared to the C2W approach (a 2-day simulation using C1W with a 1h exchange interval took about 2h, whereas with C2W the same simulation took about 3h).

Fig. 5.5. Modeled wind speed (color) and direction arrows (left panel). Modelled SWHs (central panel), and mean wave direction (right panel) in the CCI on 10/27/2008 at 1 am UTC.
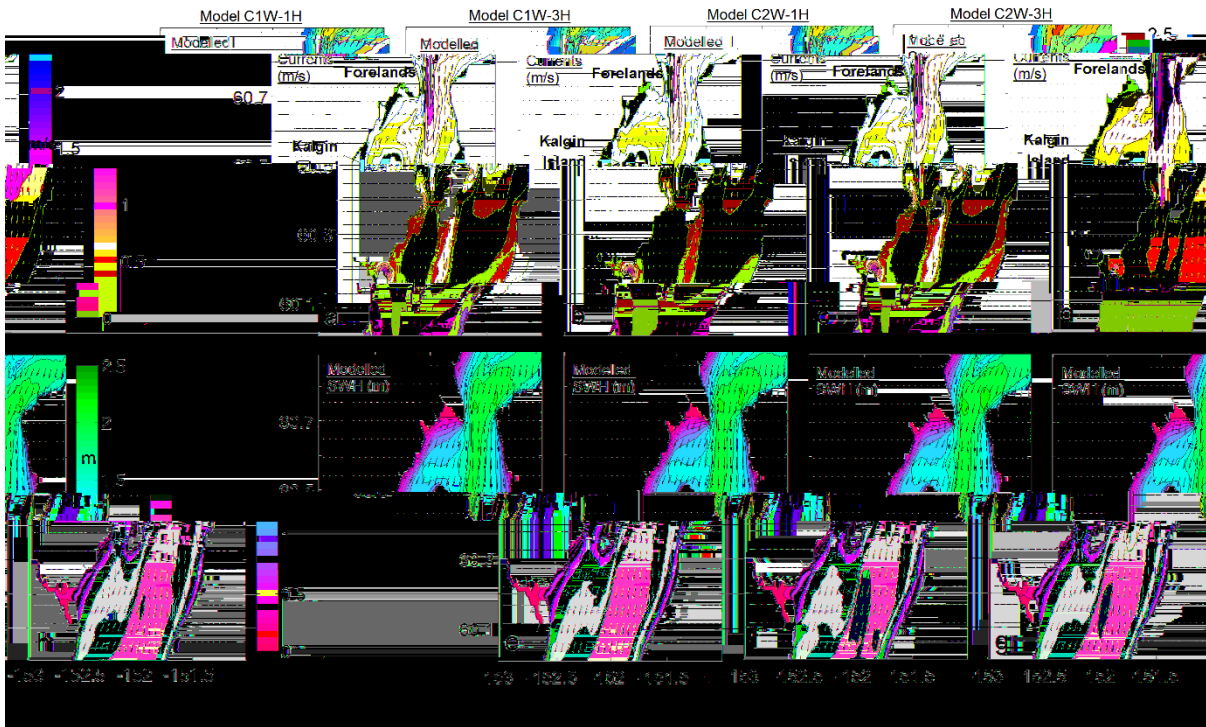
Fig 5.6 Comparison of coupled model results of currents (top panels) and SWHs (bottom panels) in CCI using C1W and C2W approaches during the same time as Fig. 5.5. Panels (a)-(d) show currents and (e)-(h) show SWHs outputted from the C1W-1H, C1W-3H, C2W-1H, and C2W-3H simulations, respectively. Arrows in top and bottom panels indicate current and wave direction. (After Singhal et al. 2013).

CHAPTER 6.   TESTING THE INTEGRATED SYSTEM.

Overall, the comparison of model results with data, described in Chapters 2-4, inspire confidence in the individual component models. We now examine the performance of the integrated system, and attempt to ascertain how errors in the individual component models affect the overall result. Each component of the system can yield errors due to limitations in physics as well as operational constraints. In the development of a practical forecasting scheme, it may not be feasible to remedy all of the errors in the component models; nor is a remedy for all errors warranted, since some of them may influence the final solution only to a small extent. Errors in the integrated model results are quantified by identifying corresponding errors in the input forcing functions (winds, currents, WOBCs, etc.). The identification and quantification of such errors could eventually serve as "guidance" for estimating the uncertainty associated with the wave forecasts, and to determine which aspects need improvement.

Toward this end, we use the same test-case considered in Chapter 5, i.e. the 12-day period in October 2008 with four distinct storm events (denoted by E1, E2, E3, E4 in Fig. 5.4, as stated earlier).   We use the available data to evaluate model performance quantitatively (some qualitative features were discussed in Chapter 5) and to examine errors.

Quantitative Assessment of Model Performance

Model performance was first evaluated (Fig. 6.1), with and without coupling, against data from B05 and B06 situated in the LCI. While the discussion in Chapter 5 dealt with only one event, here data from all 12 days of data are used. There are rather small differences between the results of all model simulations (i.e. no coupling, C1W-1h, C1W-3h, C2W-1h, and C2W-3h), and overall they follow a similar trend at both the locations. For smaller SWHs (< 2m), however, the coupled model results show some oscillations with a period of approximately half a day, especially between days 302 – 304, which are not seen in the results obtained without coupling (blue line; Fig. 6.1). These patterns can also be seen in Fig. 4.1*a* (red line, between days 318 – 322). Although the data undulations shown in Fig. 6*a* (black line, between days 318-322) are not exactly reproduced by the C1W-1h simulation, these results indicate that, for smaller SWHs (< 2m), the coupling does modify the SWHs due to fluctuating tidal currents. Overall, from these results and the discussion in Chapter 5, it may be concluded that C1W-1h is sufficient for coupling SWAN and EFDC in CI.

As regards the coupled model performance for the four events shown in Fig. 6.1, event E1 was predicted with better accuracy compared to the other events (E2, E3, E4 were under-predicted roughly by 20%, 40%, and 15% respectively). These large errors demand further investigation of other factors (winds, wave boundary conditions etc.) in order to identify the cause of such errors.
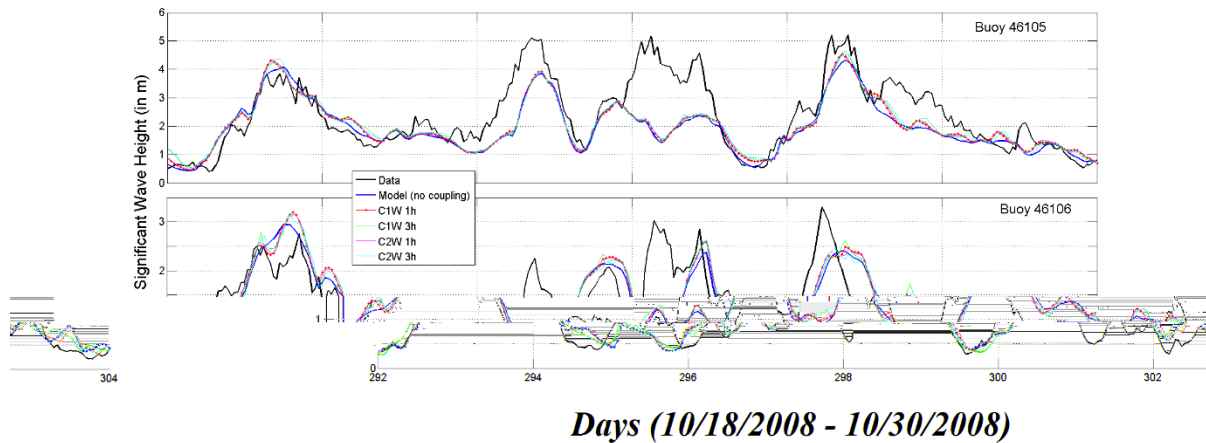
Fig. 6.1 Model comparisons of SEHs with and without coupling with data at B05 (top) and B06 (bottom).

### *Effect of individual errors in the integrated system*

The SWH errors discussed above could have resulted from errors in any of the individual components of the overall system (such as winds, currents, WOBCs). In the following, the effect of these errors is discussed in detail only for B05.

(a) Effect of Errors in WOBCs

The accuracy of the WOBCs could dictate the accuracy of the wave conditions at locations in the interior of the model domain. The LCI is often dominated by swells coming from Gulf of Alaska through Stevenson Passage and Kennedy Entrance towards the east, and Shelikof Strait towards the west (Fig. 1.1). The spectral output of WW3 model forms the basis for the WOBCs of the CI wave model. As discussed earlier in Chapter 4, spectra at B78 and B80 were used as forcing functions along the open boundaries. It is thus obvious that one must check the quality of WW3 output at B78 and B80. It can be clearly seen that the four storm events are under-estimated by WW3 (black dashed line in Figs. 6.2*a, b*). For instance, during E4, the measured SWH at B80 exceeded 8 m (Fig. 6.2*b*), whereas the WW3 prediction was about 5.5 m (~30% underestimation). This implies that these errors on the boundaries could be responsible for some of the error (or the entire error) at B05. One way to confirm this hypothesis is to force the model through buoy-measured wave spectra on the open boundaries. Unfortunately, B78 and B80 only measure the 1D wave energy spectrum and do not contain any directional information. Thus, the buoy-measured spectra were used along with the WW3 output of peak wave direction (assuming it was accurate) and the spreading function of Mitsuyasu et al. (1975) to construct a 2D wave energy spectrum (the chosen spreading function may not be suitable for unidirectional swell conditions, and hence introduces additional uncertainty). The resulting 2D wave spectra were then imposed along the open boundaries.

Wave model results at the locations of B78, B80, and B05 using the buoy-imposed spectra are also shown in Fig. 6.2 (red dotted line). The model output closely matched the buoy

28

measurements at the locations of B78 and B80 (Fig. 6.2a,b). At the location of B05 (Fig. 6.2c), only E1 and E4 seemed to be affected by the change in WOBCs. Since the wave direction is predominantly from the eastern Gulf of Alaska, this implies, to some extent, that the large seas associated with E1 and E4 are representative of the seas that occurred at B80 (located on the eastern boundary of the model domain). However, this does not apply to other events (E2 and E3) since those are still under-estimated by the model. This possibly suggests that the waves measured at B05 during events E2 and E3 may not have originated in Gulf of Alaska; rather they may be a result of some other physical phenomenon (e.g. local winds).
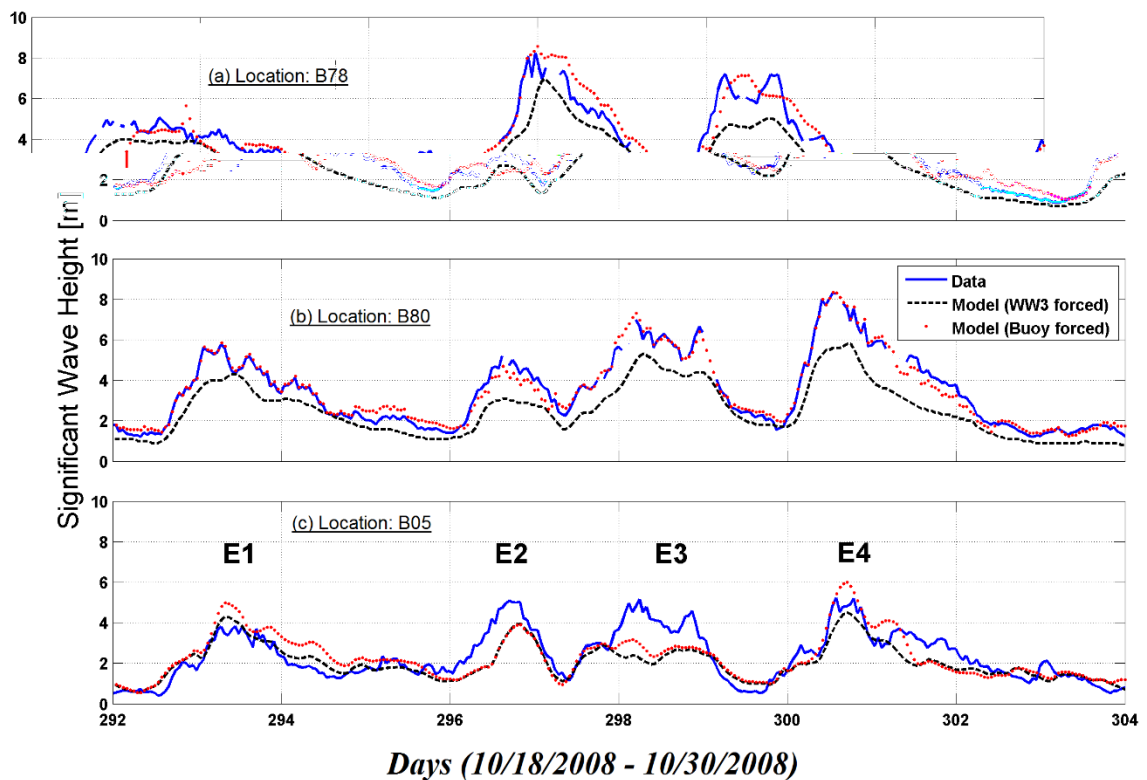
Fig. 6.2 SWH comparisons using WW3 and buoy-forced wave spectra on boundaries at three locations.

Comparisons at the location of Buoy 46077 (B77) are also shown to check the validity of using wave conditions at B78 on the entire west-boundary. B77 is located in Shelikof Strait (Fig. 1) and experiences swells coming from the south-west direction (apart from locally generated wind-seas). As can be seen from Fig. 6.3 (black dashed line), the model results do not fare well throughout the period of the simulation. This indicates that the assumption of wave conditions from B78 is incorrect along the western open boundary. Unfortunately, there are no nearby points along the western boundary from where full spectral information could be extracted. Thus, we have resorted to using an approximate approach, outlined in Singhal et al. (2010), for generating the 2D wave spectra along the western boundary. In particular, WW3 provides output of SWH, peak wave period, and peak wave direction on a 7 km grid for northern Gulf

of Alaska. Using these quantities, one can utilize the JONSWAP spectrum along with a suitable directional spreading function to create a 2D energy spectrum (see Singhal et al. (2010) for specific details). Fig. 6.3 also shows the effect of using the approximate approach on SWHs at the location of B77 (red line). It can be seen that the large errors around day 298 have reduced significantly. This allows us to conclude that the approximate approach of using JONSWAP spectrum, while not without problems, appears superior to assuming the wave conditions from B78 along the western boundary. For the remainder of the discussion that follows, the open boundaries are forced by approximated 2D JONSWAP spectrum on the western boundary and the full spectral output at the locations of B78 and B80 along the southern and the eastern boundary, respectively.


Days (10/18/2008 - 10/30/2008)
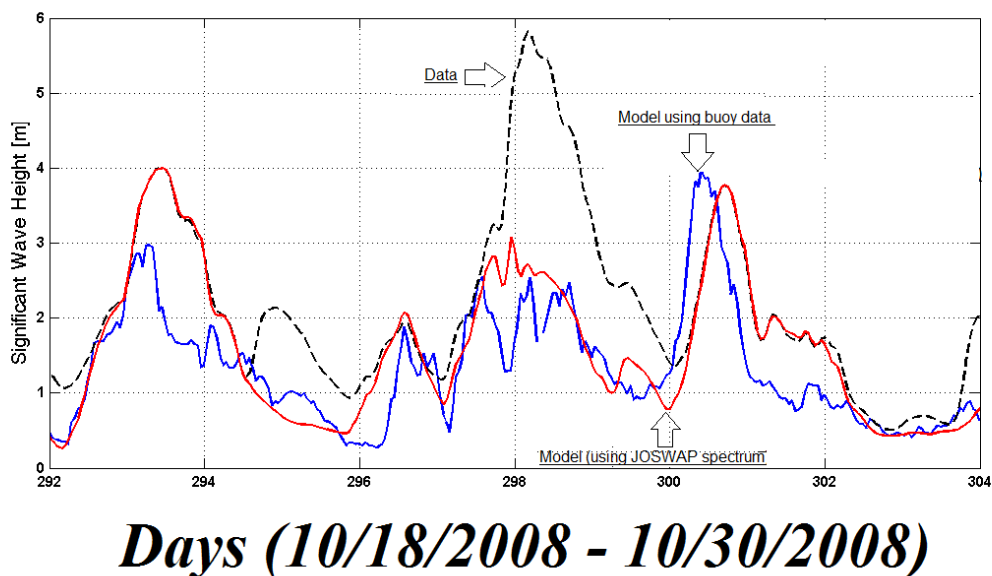
Fig. 6.3. SWH comparisons at B77 using buoy and JONSWAP spectra on the western open boundary. (After Singhal et al. 2013).

(b) Effect of Errors in Winds

Turning to the errors in the input winds, based on the previous discussion, events E2 and E3 do not seem to be affected by the the errors present in the WOBCs. The quality of WRF winds was checked specifically during E2 and E3. As noted earlier, B05 is not equipped with an anemometer, and thus WRF winds were compared at the locations of three weather stations – Augustine Island (AUGA2), Flat Island (FILA2), and Amatuli Island (AMAA2) – that form a

triangle around B05 (Fig. 1.1). The winds were predominantly from the west during the two events (Fig. 6.4 right column). This trend is typical during the month of October when the winds originate from Iliamna Lake in the west (Liu et al. 2006). Fig. 6.4 indicates that the WRF model under-predicted the wind speeds at AUGA2 and FILA2. The under-prediction, on average, was by a factor of about 1.25 for E2, and about 1.75 for E3. This under-prediction in the wind speeds seems to be in line with the corresponding under-prediction in the modeled SWHs at B05. The winds at AMAA2, on the contrary, were consistently over-predicted by WRF (this trend was found during other times as well). A full assessment of WRF model for CI is, however, beyond the scope of this work, and attention is rather directed towards finding solutions in order to improve the corresponding wave estimates.
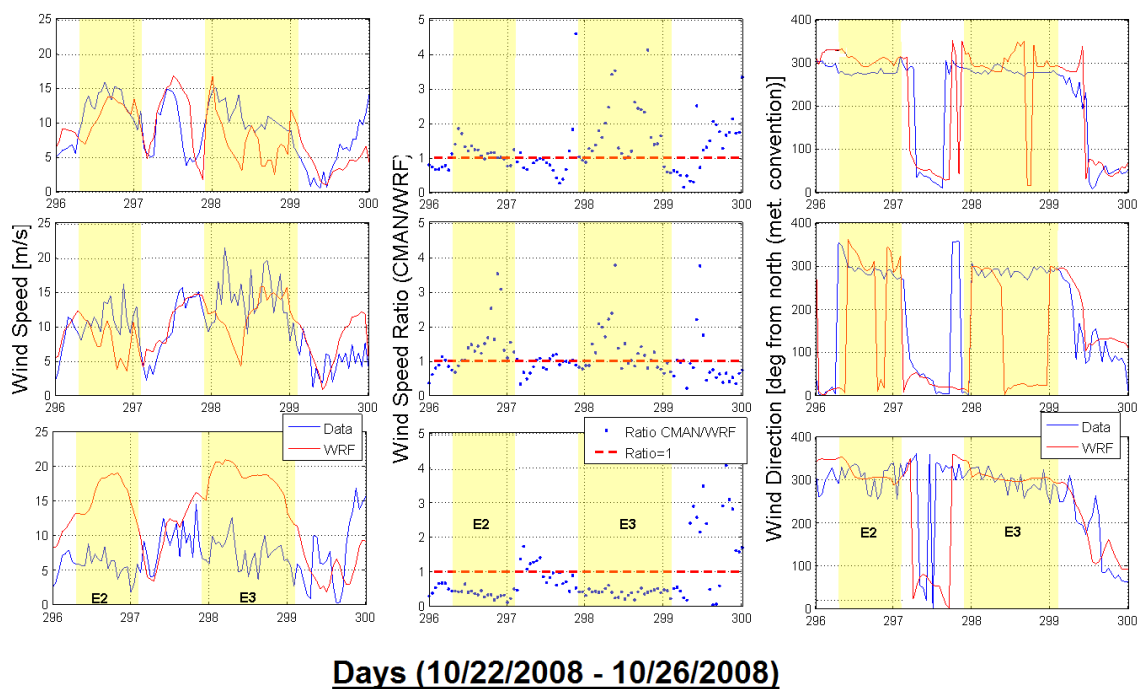
Fig. 6.4. WRF model comparisons at three weather stations (top row, Augustine Island; middle row, Flat Island; bottom row, Amatuli) for wind speed (left column), ratio of observed vs. WRF (central column), and wind direction (right column).

In this case, a straightforward remedy is to modify the wind speeds using the average under-prediction ratio during events E2 and E3. The WRF wind speeds were thus adjusted by a factor of 1.25 spatially over a small region near B05 (somewhat subjectively determined) for E2 (that lasted about a day); a factor of 1.75 was used over the same region for E3 (also lasted about a day). The results, shown in Fig. 6.5, clearly indicate that the adjustment significantly improves the SWH estimates during E2 and E3 (even though some errors still remain).
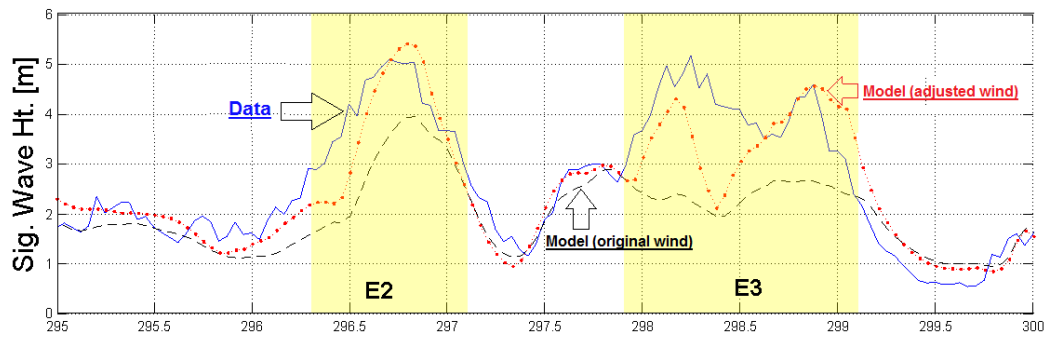
Days 10/21/2008 - 26/10/2008

Fig. 6.5. Sensitivity of SWHs to enhancement of wind speed during E2 and E3 at B05.

Although the above discussion shows that improving the winds for specific events may improve the SWHs, the obvious question, viz. "how does the wave forecaster know there is a problem with the winds?", still remains unanswered. The randomness of the wind-fields renders the creation of simple correction factors for general use impossible. Other solutions, such as the improvement of the WRF model physics, better resolved topographical features, and/or data assimilation, may have to be explored.

(c) Effect of Errors in Currents

While the velocity fields calculated in Chapter 3 were fairly accurate, it is possible that random errors in the wind-fields used to force the circulation model or (possibly seasonal) baroclinic effects, not considered here, could induce errors in a forecasting scheme. A sensitivity analysis was therefore performed by adding a random error ϵ to the modeled flow velocities, where ε is a uniformly distributed random number such that, -0.1*velocity $\leq \varepsilon \leq$ 0.1*velocity. The SWH results obtained using the updated velocities were compared to the results without the added error at various locations throughout the CI. It was found that, for the most part, the maximum differences between the SWHs were of the order of ±10 cm. These small differences are negligible in the context of the surface wave heights applications, and suggests that the velocities obtained from the EFDC simulations are adequate for the task at hand.

CHAPTER 7. DEVELOPMENT OF AN OPERATIONAL FORECASTING SYSTEM FOR COOK INLET

In previous chapters, the performance of the wave model (SWAN) and circulation model (EFDC) was discussed in the hindcast mode. Many issues related to grid resolution, effective frequency range and spectral resolution, the requirement of finer nested domains to resolve coastal features, efficient coupling procedures, the importance of various forcing mechanisms (winds, tides and wave-induced forcing), the modeling of wetting/drying processes, etc. were addressed through these hindcast simulations. Satisfactory performance of these models motivated their use for forecasting purposes. The main objectives of this project is to develop an operational forecasting system that would provide forecasts of waves (including the forecasts of associated currents and surface elevations) using an effective method to couple the wave model and the circulation model. This consists of the following tasks:

(1) Development of an operational wave forecasting module for the entire Cook Inlet domain as well as for nested domains such as Kachemak Bay (KB) and Upper Cook (UCI) at fine resolution (*vide* Figs. 3.1, 3.4, 3.5, and 3.6).
(2) Development of an operational circulation model for these domains with wetting/drying process included.
(3) Coupling the wave and circulation models in the forecast mode as described in Chapter 5.

Based on the hindcast work described earlier, we established an operational wave forecast module (step 1) above. The nested grid system (described in Chapter 3), comprised of the inner high resolution grids (KB and UCI) and outer low resolution (entire CI region) grids, is used for forecasting purposes. A grid resolution of ~ 1.5 km is used for outer CI grid, whereas the nested KB and UCI domains are resolved at approximately 0.2 km (see Fig.7.1). The spectral ranges (minimum and maximum frequencies) used for the simulations are described below:

Domain	f_{min} (Hz)	f_{max} (Hz)	No. of frequencies (Hz)
CI	0.04	0.5	24
UCI	0.05	1.0	48
KB	0.05	1.0	48

To provide wave forecasts systematically on a daily basis, a MATLAB protocol to automatically obtain data (WRF winds and NCEP waves) by interconnecting two different FTP servers was developed. The system is run on a Macintosh computer and uses a number of MATLAB scripts which is automated to run on a daily basis. The salient features of this protocol are shown in Fig. 7.2. Our earlier work in Prince William Sound (Singhal et al. 2010) formed the basis for this development.

❑ **Grid Resolution Outer Domain**

   SWAN - ~ 1.5 km

   EFDC - ~ 4 km at Open Ocean Boundary
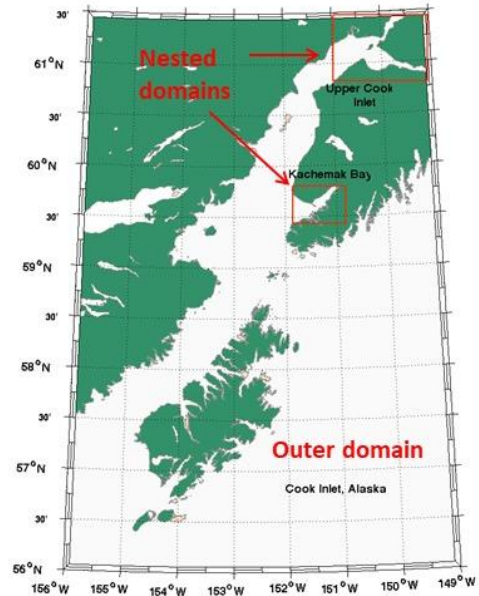
      and ~1.5 km to Northern-most Part of CI

❑ **Grid Resolution Kachemak Bay**

   SWAN and EFDC - Outer 1 km, Inner ~200m

❑ **Upper Cook Inlet**

   SWAN and EFDC - Outer 1 km, Inner ~200m

Fig. 7.1 Forecast model domains

The system is initialized at 0000 GMT and the input forcing functions (winds and boundary conditions) are downloaded from FTP servers of AEFF and NOAA. The first 12 hours (denoted as \MODEL SIM TIME" in Fig. 7.2) include the time lag associated with the WW3 output (~5.5 hours) and the WRF output (~7.5 hours), and also the model computational time (~2.5 hours). Overall about 12 hours of real time are lost in the modeling effort, and hence, even though each simulation is made for 48 h, the forecasts are provided at 1200 GMT for the next 36 h. Upon completion of the simulation, contour plots of SWH, peak period (Tp), mean direction (Dp), and wave-induced Stokes' drift are generated. These are also transferred to the Texas A&M University FTP server so that the NWS office (Anchorage) can access them (this was based on the advice of Dr. Carven Scott of NWS). During the forecast mode, the sea-state at 24 h is also saved in order to initialize the next 00z run (the following day). The system provides 36 h forecasts of significant wave heights, peak periods and peak directions twice every day before 0000 GMT and 1200 GMT.

As to the flow model, EFDC model was applied to the CI domain covering the region between -156°W to -149°W and 56°N to 61.5°N, on an irregular grid with a resolution of about 4 km at the open ocean boundaries, and decreasing to a resolution of ~1.5km in the northern- most part of CI. The time step was 12 minutes. Based on the protocols described below, we have established an operational forecasting module to provide 36 h forecasts of water surface elevations (WSEs), surface currents and the extent of "wet/dry" regions by using a nested grid system. For these domains, the representative depth at which the grid is assumed to become dry (HDRY) must be selected to model the extent of dry regions. For each time-step, the model checks the total depth against the specified threshold depth HDRY at each grid point. Here, HDRY was set equal to 0.5 m, based on earlier studies (Chapter 3).
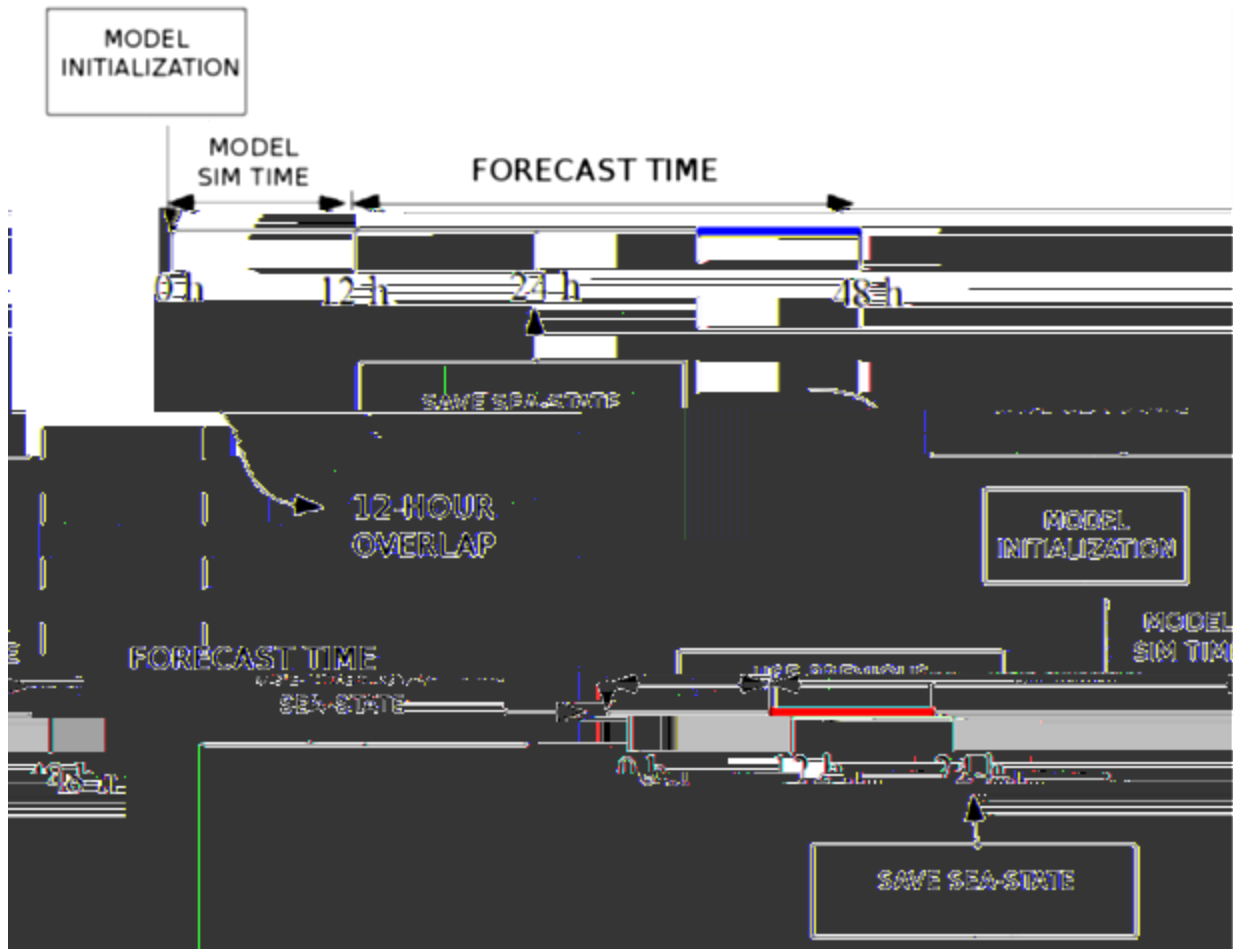
Fig. 7.2 CI forecasting system protocol

In general, the coupling between the wave and circulation models is performed using offline coupling (OFC) or online coupling (ONC). Details regarding these coupling methods are discussed in Singhal et al. (2013). They stated, "…for forecasting purposes, one-way coupling would be adequate; two-way coupling, albeit incorporating better physics, has less of an effect on the accuracy of the forecast than improved wind-fields." Moreover, they found the effect of the waves on the currents marginal and deemed the ONC approach unnecessary for CI domain. To develop the forecasting system, only offline coupling with one-way approach shown in Fig. 7.3 is considered.
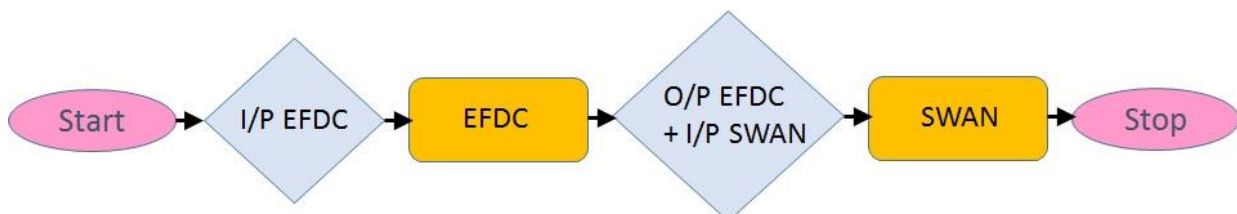
Fig. 7.3 Offline coupling with one-way approach. I/P is input, O/P is output.

Example Forecasts

Overall, the wave height forecasts are provided twice a day at 0000 GMT and 1200 GMT. Using the protocol and steps discussed above, the forecasts of water surface elevation and current velocities for three different domains mentioned earlier are provided twice every day before 0000 GMT and 1200 GMT. The forecasts can be accessed through the following links established during this project:

For the wave forecasts:
http://wave.tamug.edu/CI_main.html

For the circulation model:
http://wave.tamug.edu/CI_latest/CI_CIRC_main.html

Some contour plots of intermediate hour forecasts (for 1200 GMT run on May 06, 2013) of WSEs obtained from the operational system for outer CI, KB and UCI domains are shown in Figs. 7.3-7.5. Note that the white patches in these plots depict "dry" region. Similar forecasts for the surface currents using outer grid simulations are shown in Fig. 7.6.
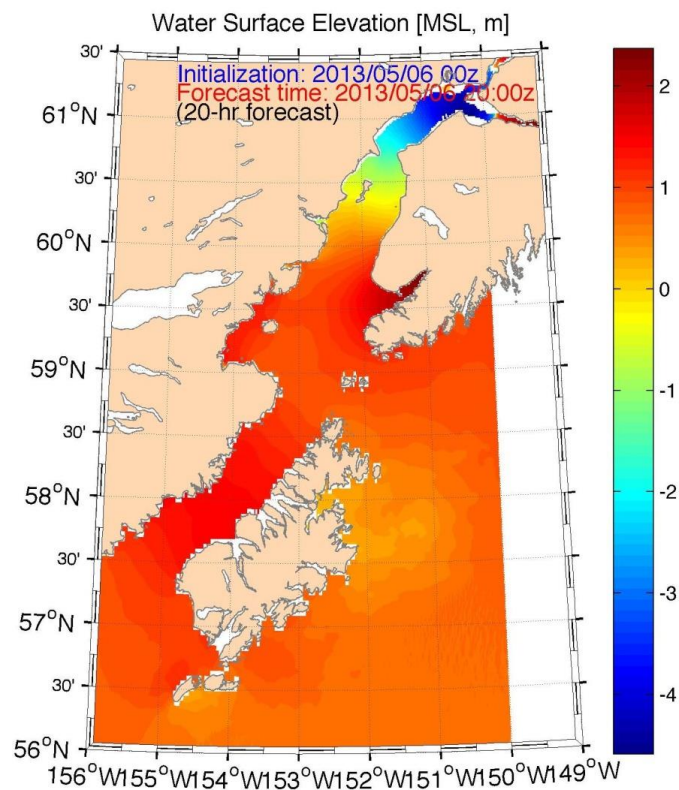
Fig. 7.3. Forecasted water surface elevations for outer (coarse) CI grid simulation. White patches depict "dry" region.
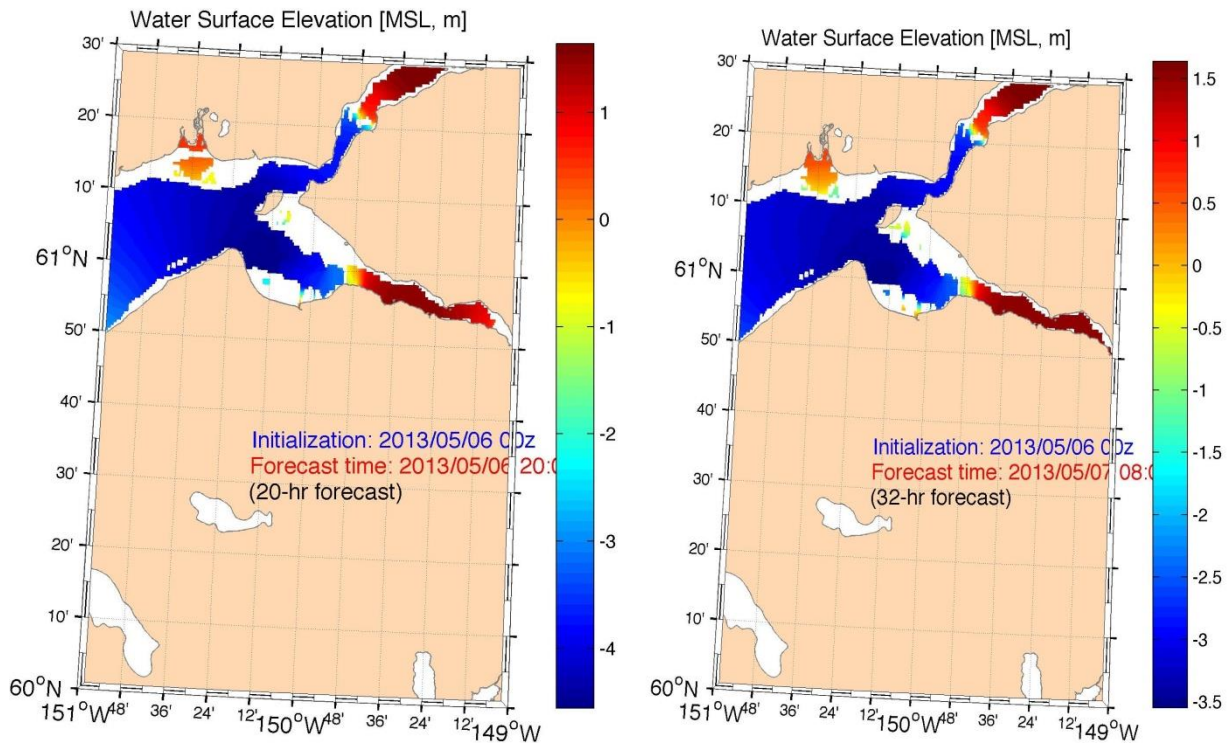
Fig. 7.4. Forecasted instantaneous water surface elevations for well-resolved UCI domain. White patches depict "dry" region.
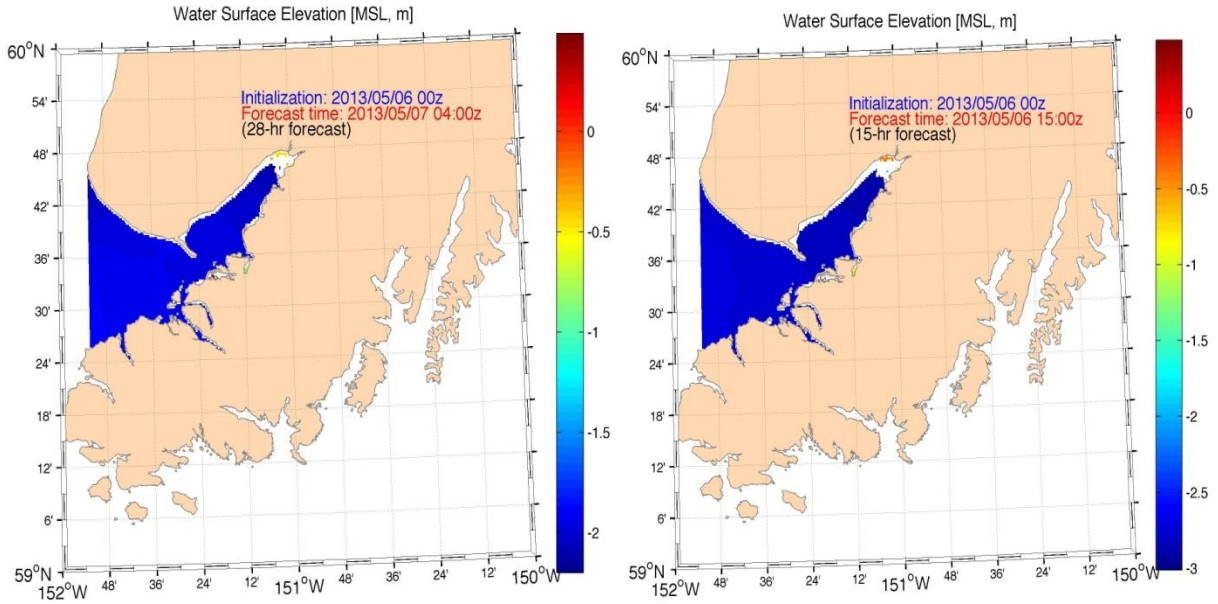
Fig. 7.5. Forecasted instantaneous water surface elevations for well-resolved KB domain

Fig. 7.6. Forecasted surface currents for outer (coarse) CI grid simulation.

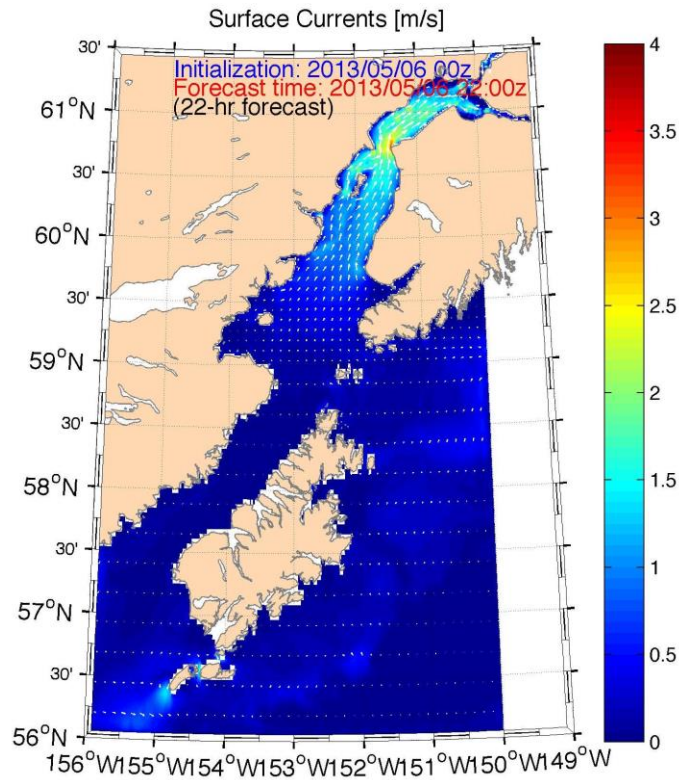A sample resulting wave forecast is shown in Fig. 7.7. These figures, are shown by way of example. In Chapter 8, we examine these results in detail from the view point of reliability of the forecasts.
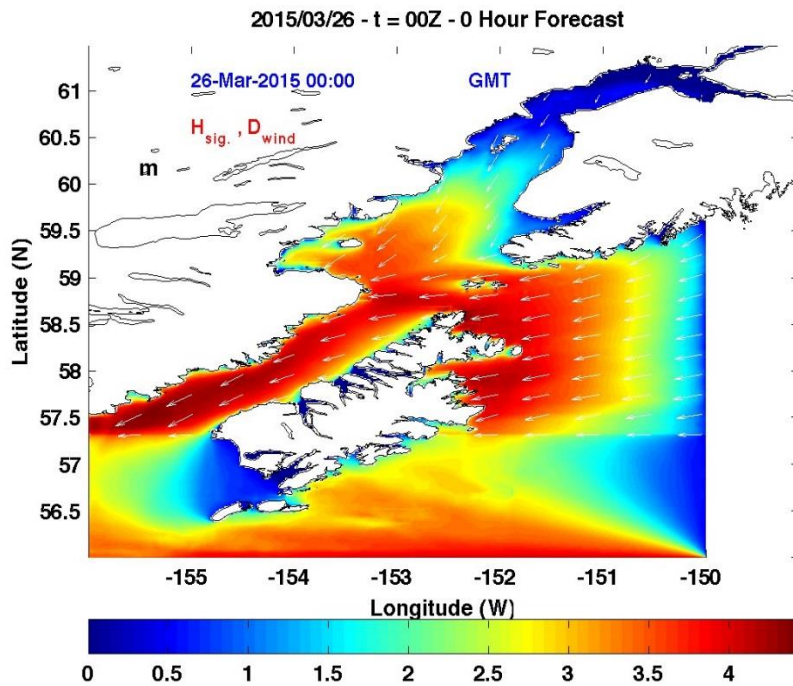

Fig. 7.7 Sample wave forecast in Cook Inlet, Alaska

CHAPTER 8. SYSTEM VALIDATION: RELIABILITY OF THE OPERATIONAL COOK INLET FORECAST SYSTEM

For purposes of model verification and validation, normally hindcasts are performed for a set of predetermined specific events. These simulations can be repeated after modifying or adjusting spatial/temporal resolutions, various model parameters, and/or forcing functions, using available data as a guide. Simulations in the forecast mode, on the other hand, offer the modeler relatively little flexibility in this regard. The modeler has no data for the future and has little recourse except data assimilation if the forecast indicates a mismatch with the data, if available. Model resolution may be dictated to a greater extent by the logistics of obtaining a forecast rather than by modeling accuracy. Forcing functions also may contain inaccuracies, against which there may be no easy remedy. Thus, once a system has been designed, guided by hindcast studies such as those described in Chapters 2-6, the modeler has little choice but to accept the flaws of the system. Therefore, a specific assessment of the "forecast skill" must be provided. This will enable users to invest the appropriate confidence in the forecast and plan accordingly.

To address forecast uncertainty, forecast centers sometimes run wave model ensembles. This issue has also been recently addressed in a limited manner by Bidlot et al. (2002) for global simulations (not regional) and Dykes et al. (2009) for the Adriatic. These studies have compared model predictions to data. However, the comparisons are provided in the form of the usual statistics, viz. correlation coefficients, best-fit slopes, scatter indices, etc., which do not, on their own, assist the user in establishing the likelihood of occurrence of a predicted condition. In contrast, our goal is to provide a measure of the uncertainty associated with a *specific* forecast, which is what a user would desire.

As noted earlier, few if any buoys are operational in the CI domain. We have therefore taken recourse to satellite data. Unlike *in situ* instrumental data, which are available at a given location at regular intervals (e.g. hourly), satellite data are available only at specific times relating to the flight protocols. While model results are available on a regular grid for the entire domain at three-hourly or hourly intervals, satellite data consist of measurements "along-track", typically at a spacing of approximately 6 km; and, the satellite "overflies" the domain on an exact or approximate repeat protocol (say, every 10 days), although it may still overfly the domain but on a different track (say) 3 or 4 days after the first one.

To validate the efficiency of the forecasting system, satellite data from currently flying missions like SARAL/ALTIKA, JASON-2 and CRYOSAT-2 can be used. The tracks in the CI domain are shown in Fig. 8.1. The work of data acquisition is tedious and we had to first identify appropriate tracks that also matched the model predictions in space and time. We extracted satellite data in the Cook Inlet region from AVISO (http://www.aviso.altimetry.fr/en/home.html) which provides 1°x 1°, gridded multi-mission wind/wave data sets. This was used in conjunction with the "Radar Altimeter Acquisition System" or "RADS" which provides specific along-track data (http://rads.tudelft.nl/rads/data/authentication.cgi). Using RADS, the SWH data have been

collected using automated MATLAB scripts which plot the along-track data from their ASCII files. Comparisons between model and satellite data are made for the dates when the satellite passes over CI.

(a) SARAL/ALTIKA   (b) JASON-2   (c) CRYOSAT-2
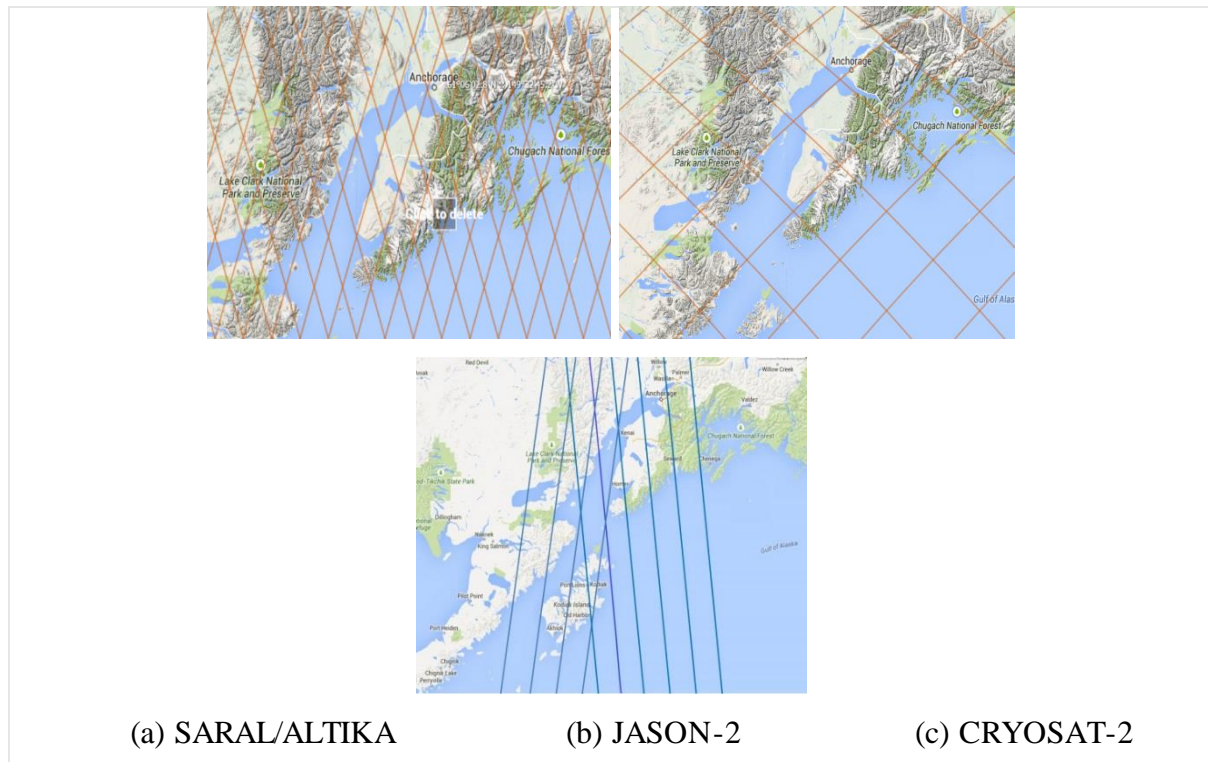
Fig. 8.1 Satellite tracks in the Cook Inlet region (the three panels correspond to each of the satellites).

A satellite altimeter an essentially measures wave heights based on a radar pulse as it flies along its tracks. As stated earlier, we used the JASON-2, CRYOSAT-2 and SARAL/ALTIKA satellites described in Table 8.1 for comparing with the model. JASON-2 operates using two different radar frequencies, viz. the Ku-band (13.6 GHz) and C-band (5.3 GHz). The Ku-band is most commonly used frequency for JASON-1, ENVISAT, etc. JASON-2 flies in a low-earth orbit with a global coverage between 66°N and 66°S latitude and covers 95% of world's oceans with tracks repeating approximately 10 days apart. CRYOSAT-2, built by the European Space Agency, also measures SWHs, using the Ku-band, and wind speeds. SARAL/ALTIKA measures SWHs (Ka band) and wind speed as well. The repeat periods for JASON-2, CRYOSAT-2 and SARAL/ALTIKA tracks are 9.8 days, 29.8 days and 35 days, respectively.

Table 8.1 Satellite Characteristics

	CRYOSAT-2	**JASON-2**	**SARAL/ALTIKA**
Launch Date	April 2010	June 2008	February 2013
Mission Type	Earth observation	Earth orbiter	Remote sensing
Mission Duration	3 years (planned)	3 years (design) 5 years (extended)	5 years (ARGOS) 3 years (AltiKa)
Purpose	Earth polar measurement	Physical oceanography	Marine meteorology Sea-state forecasting, etc.
Period	99.16 minutes	112.34 minutes	100.54 minutes

Basic Comparisons

Comparison requires one to first appropriately collocate measured and modelled SWHs, because few, if any, satellite tracks fall directly over the model grid points. Therefore, for the comparisons, SWH data are used from the four nearest model grid points and then averaged. Temporally, the satellite crossing time was rounded to the closest forecast hour. By way of example, SWH data obtained from the model are compared in Figs. 8.2-8.4 and Tables 8.2-8.4. The results in general show good match between model results and measurements.

Table 8.2 Comparison of modelled significant wave height (SWH) with CYROSAT-2 data

Latitude	Longitude	SWH CRYOSAT-2	Averaged SWH in Model
59.003290	-152.132235	2.719	2.758
58.889719	-152.155201	1.028	1.166
58.662565	-152.200838	3.160	3.017
58.321805	-152.268573	2.633	2.641
58.037810	-152.324377	0.545	0.816
57.412936	-152.445170	1.081	0.894
56.844767	-152.552729	1.837	1.643
56.503819	-152.616283	1.690	1.727
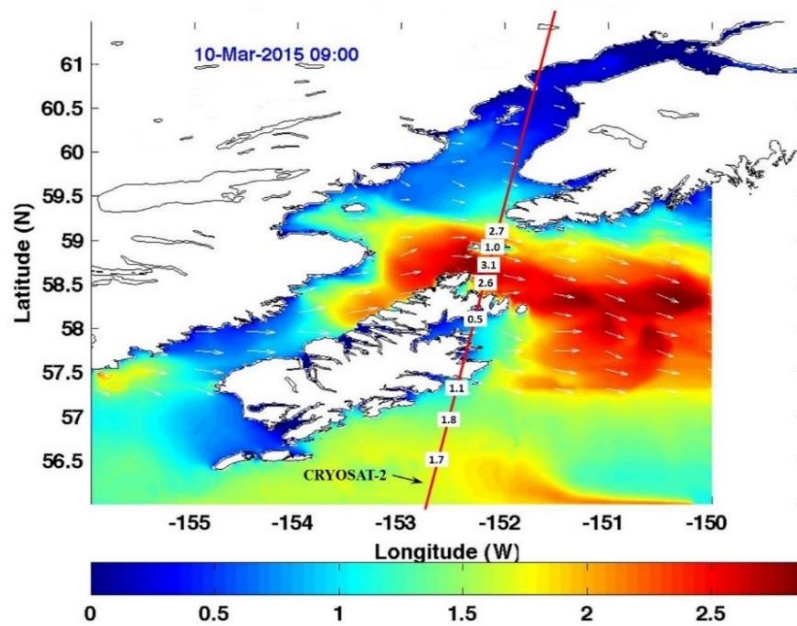
Fig. 8.2 CYROSAT-2 data (line) and modelled SWH in m (color plot).

Table 8.3 Comparison of modelled significant wave height (SWH) with JASON-2 data

Latitude	Longitude	SWH JASON-2	Averaged SWH in Model
59.288832	-153.843698	1.326	1.476
59.155585	-153.525746	2.24	2.007
59.022010	-153.210390	2.569	2.417
58.887322	-152.897612	2.355	2.438
58.683723	-152.433240	3.057	2.551
58.581229	-152.203196	3.452	2.652
58.340305	-151.671924	3.304	2.787
58.061987	-151.070479	3.365	2.567
57.991921	-150.926154	3.076	2.439
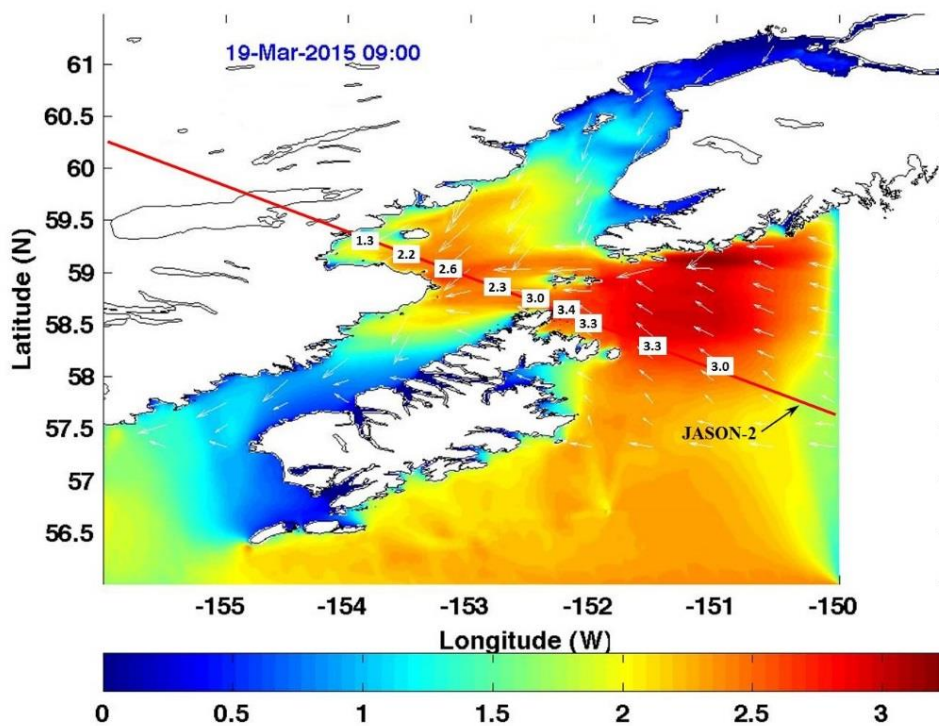
Fig. 8.3 JASON-2 data (line) and modelled significant wave height (color plot).

Table 8.4 Comparison of modelled significant wave height (SWH) with SARAL/ALTIKA data

Latitude	Longitude	SWH in SARAL/ALTIKA	Averaged SWH in Model
56.063723	-150.324188	2.779	2.678
56.482870	-150.563049	2.805	2.796
56.961477	-150.841756	2.838	2.634
58.513796	-151.793079	3.879	3.622
58.930776	-152.061994	2.731	2.596
59.049857	-152.139903	3.173	3.079
59.287900	-152.297169	2.653	2.403
59.525782	-152.456398	2.574	2.525
59.644660	-152.536763	2.165	2.378
59.882293	-152.699023	1.204	1.352
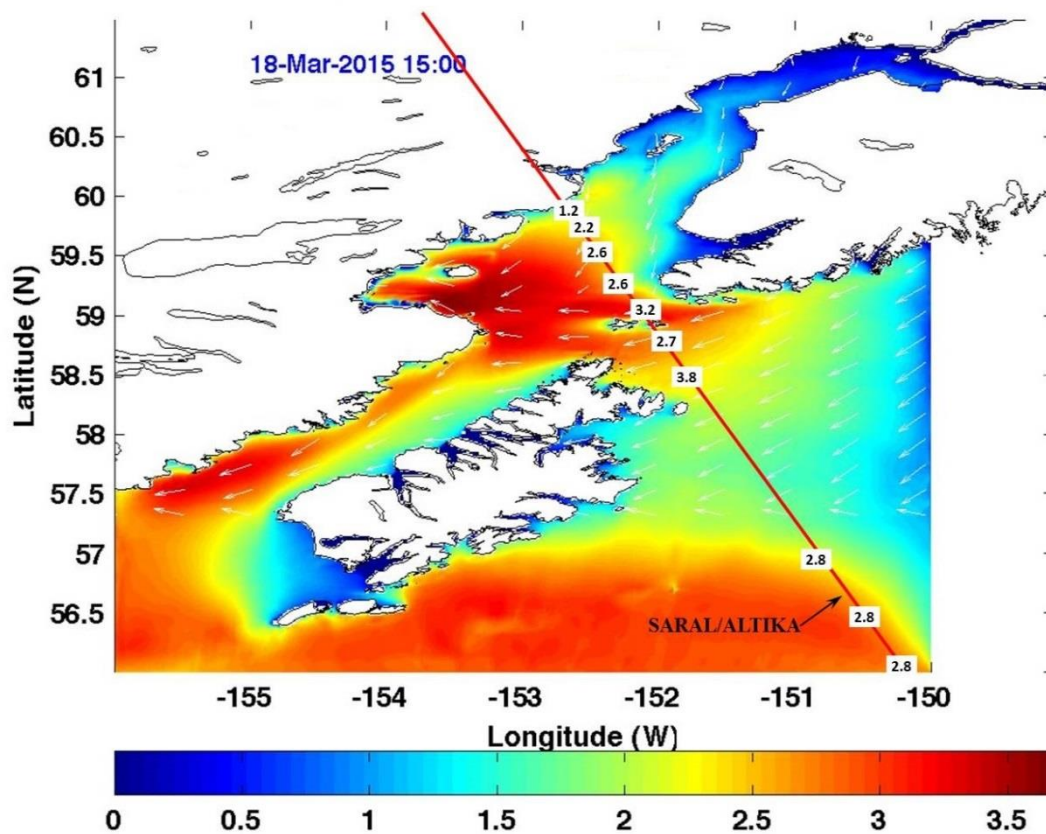
Fig. 8.4. SARAL/ALTIKA data (line) and modelled significant wave height (color plot).

Additionally, comparison in a "nested" region of the model, i.e. Kachamek Bay, for March 2015 is shown in Figure 8.5. Similarly, Figs. 8.6 and 8.7 show comparisons based on tracks falling in the narrow areas at the entrance of Upper Cook Inlet. In both cases, there seems to

be good agreement between the modelled data and the JASON-2 satellite data. This comparison in the nested area suggests that model performance is quite reliable even in regions where flooding and drying can influence the hydrodynamics.
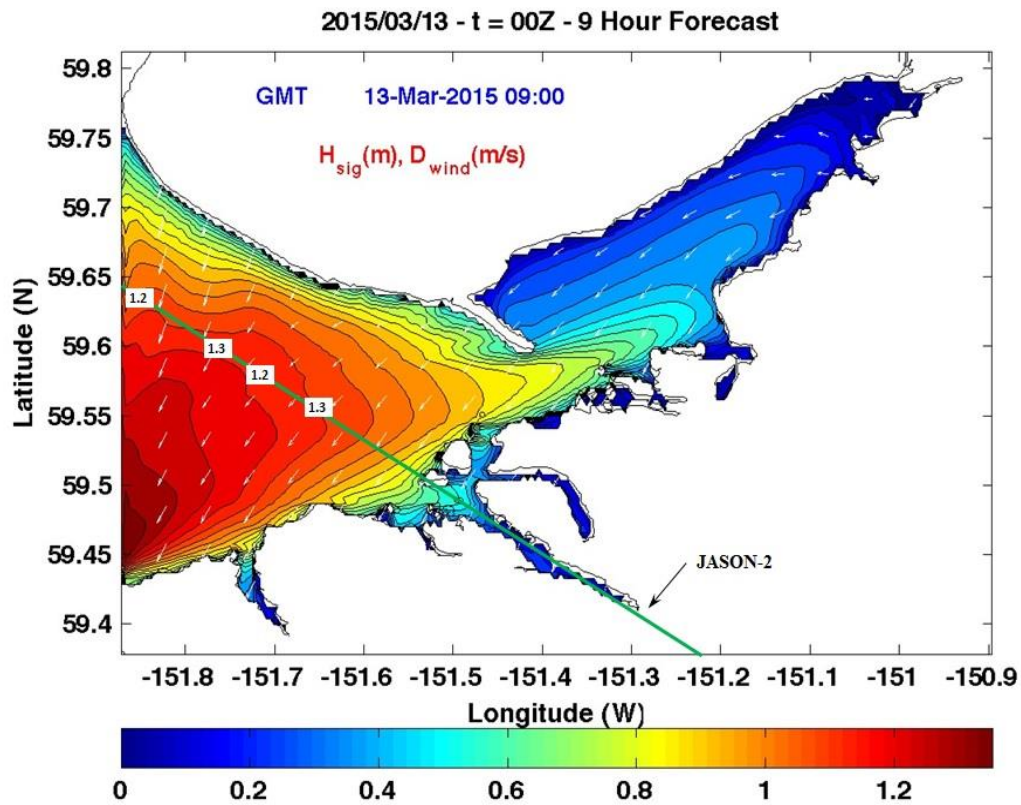

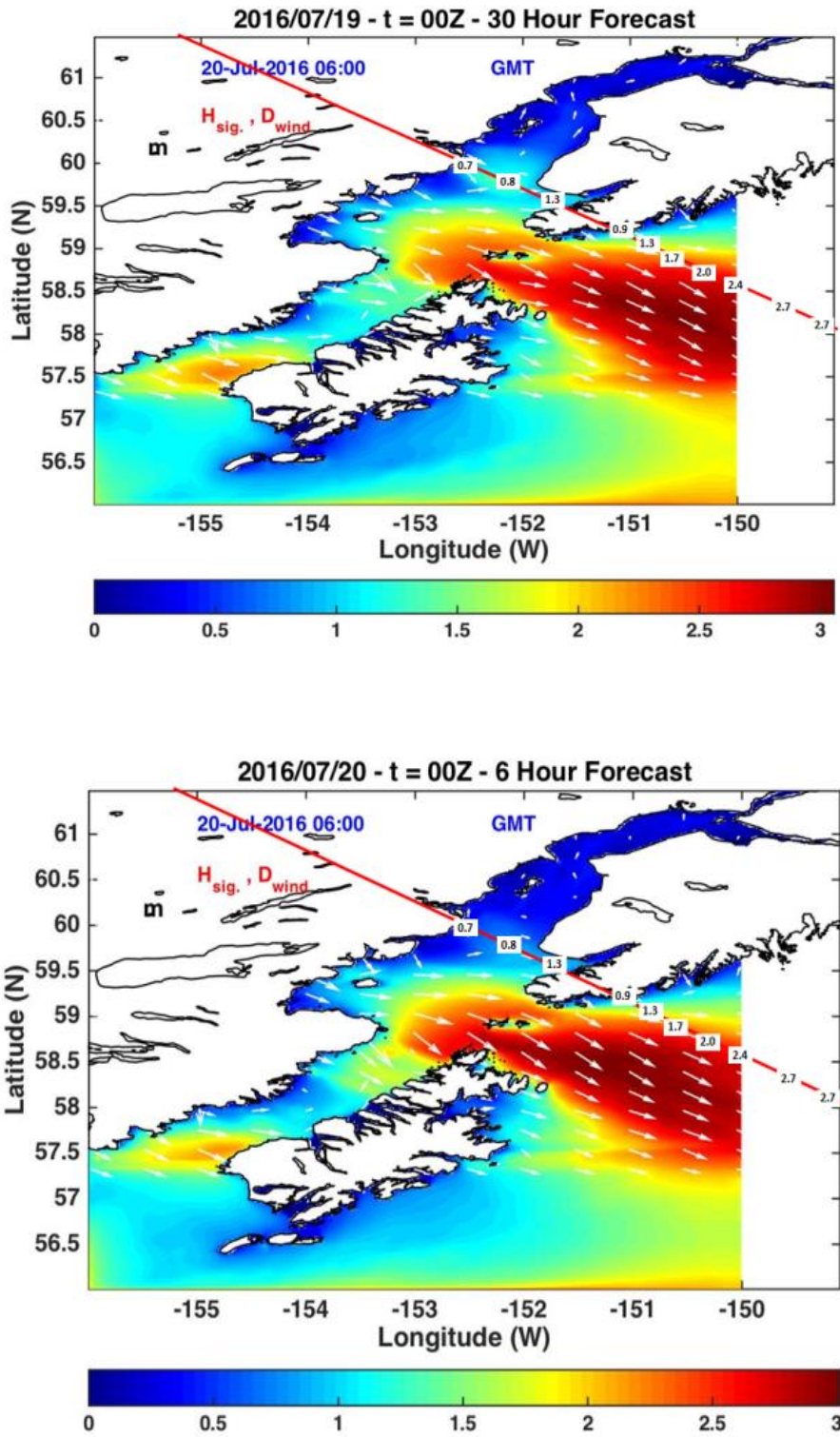**Fig. 8.5** JASON-2 data (green line) and modelled SWH in m (color plot) in Kachemak Bay

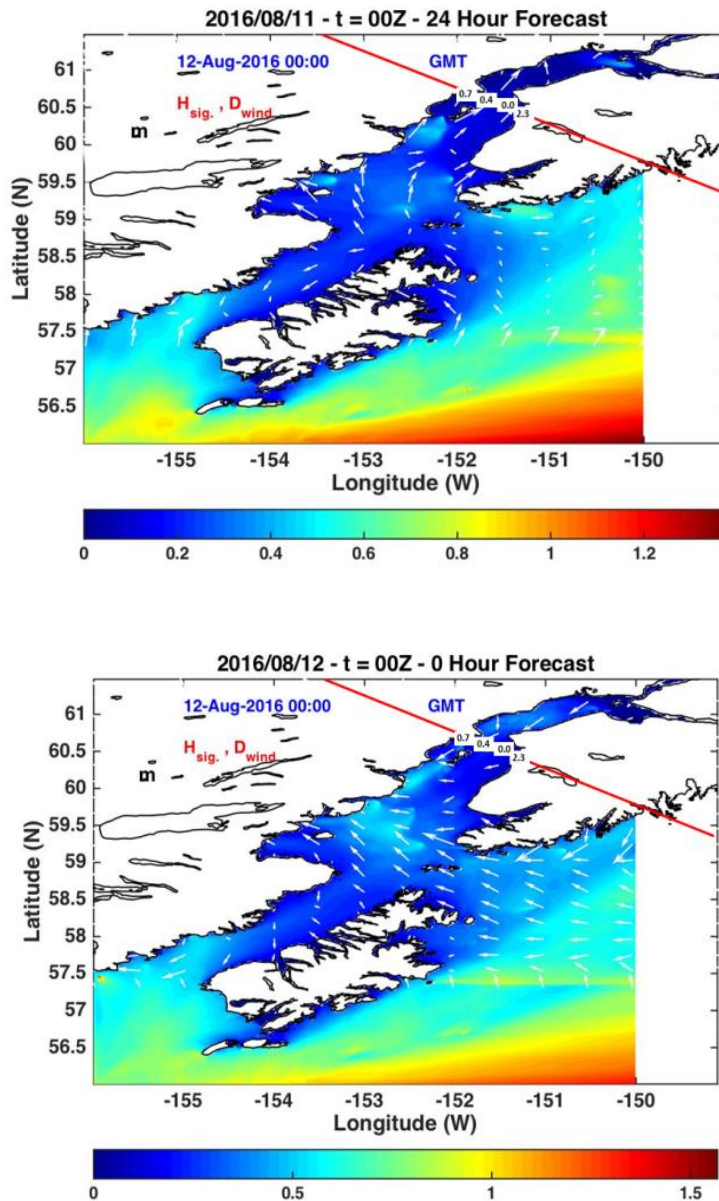**Fig. 8.6** SWHs (in m) using JASON-2 "pass number-P206" on July 20th, 2016

Fig. 8.7 SWHs (in m) using JASON-2 "pass number-P028" on Aug 12th, 2016

Forecast Comparisons

In the model domain, SARAL/ALTIKA overflight occurs at approximately 3 pm and 5 am. The corresponding data can thus be used only for comparing with forecasts made at noon the same day and the previous day. So, three lead times can be determined, based on those specific times: for L=3 and 27 h for a 3pm satellite pass, and L=17 h for 5 am satellite pass. However, the JASON-2 and CRYOSAT-2 overflights do not repeat at the same time because repeat cycle is not in terms of an integer number of days. These tracks repeat every 10 and 29 days, but two hours earlier each time; these data therefore yield different lead times relative to the forecasts made at noon the same day and previous day. Thus the lead times relative to the forecasts vary widely. We have therefore grouped all occurrences in lead time intervals of six hours, i.e. L=0-6hr, 6-12hr, 12-18hr, 18-24hr, 24-30hr and 30-36hr. Thus, some smaller lead times are possible for these two satellites compared to SARAL/ALTIKA because of their overflight timing

protocols. In general, these lead times provide information on time scales that are reasonable for various operational purposes.

Sample comparisons, for two tracks in March 2015, are shown in Figs. 8.8 and Figs. 8.9 for JASON-2 and CRYOSAT-2, respectively. The results show that the forecasted significant wave heights were in the range of 1-3 m, and that they corresponded to the satellite measurements reasonably well. This is particularly encouraging since these represent 33-hour forecasts.
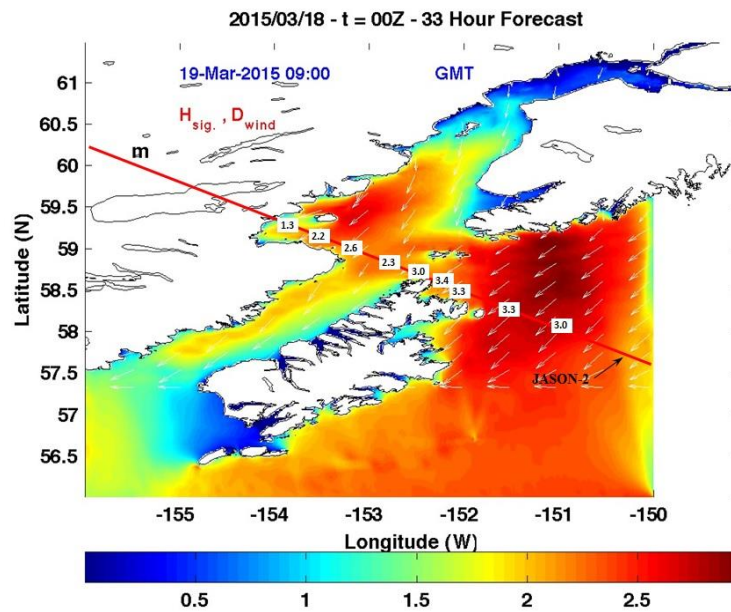

Fig. 8.8 SWH comparisons (meters) for March 18, 2015 at 9 a.m.; color: 33-h forecast; white boxes; JASON-2 satellite measurements.
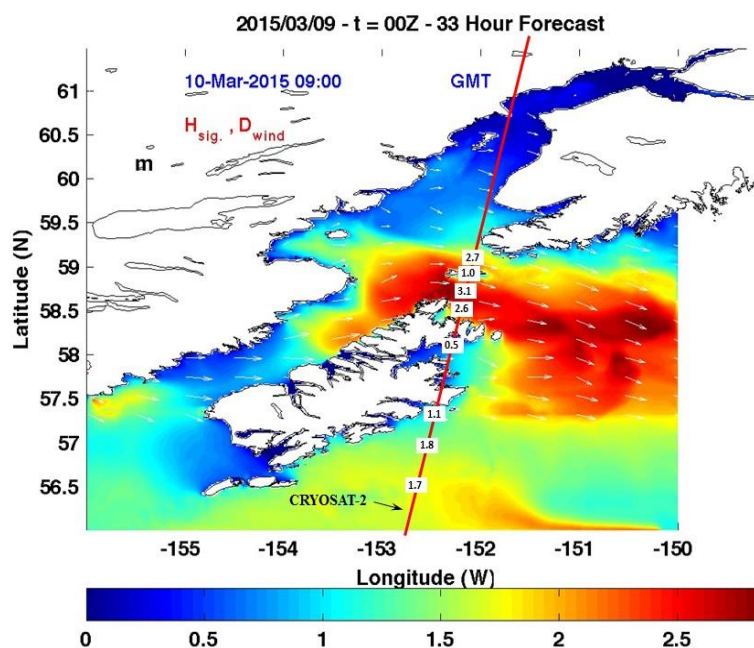

Fig. 8.9 SWH comparisons (meters) for March 09, 2015 at 9 a.m.; color: 33-h forecast; white boxes; CRYOSAT-2 satellite measurements.

Overall Model Reliability

Commonly used statistical measures such as the best-fit slope (m), the correlation coefficient (R^2), and the root-mean-square error (RMSE) are employed to assess to overall reliability of wave forecasts. Statistical measures are shown in Figure 8.10 for L=3h, 17h and 27h for comparisons relative to data from SARAL/ALTIKA. Generally (not surprisingly) the quality of the forecast degrades for longer lead times. Overall, though, the correlation is high for the wave heights ($R^2 = 0.87$, 0.88 and 0.87 for three forecasts) even though the R^2 is slightly lower for the wind speeds ($R^2 = 0.79$, 0.81 and 0.79). Also, encouraging is the high correlation for long lead times (L = 17 hr and 27 hr). Mostly, the predicted SWHs are a very close to the slope 1 line.

Similar statistics have been constructed for the other two satellites (JASON-2 and CRYOSAT-2). They are shown in Figure 8.11 for L=0-6h, 6-12h, 12-18h, 18-24h, 24h-30h and 30h-36h with 6h intervals. (As noted earlier, this comparison is possible for smaller and longer lead time intervals for these two satellites, relative to the fixed 3h, 17h, and 27h lead times for SARAL/ALTIKA, because of the overpass timing protocols). While, as before, the quality of the forecast appears to be lower for longer lead times, the generally high correlation for the wave height ($R^2 = 0.77$, 0.84, 0.82, 0.85, 0.81 and 0.79 for all forecasts) engenders confidence in the results. Moreover, the R^2 is slightly higher for the wind speed ($R^2 = 0.93$, 0.92, 0.93, 0.93, 0.93 and 0.92) than for SARAL/ALTIKA. Again, the predicted SWHs are very close to the slope 1 line.
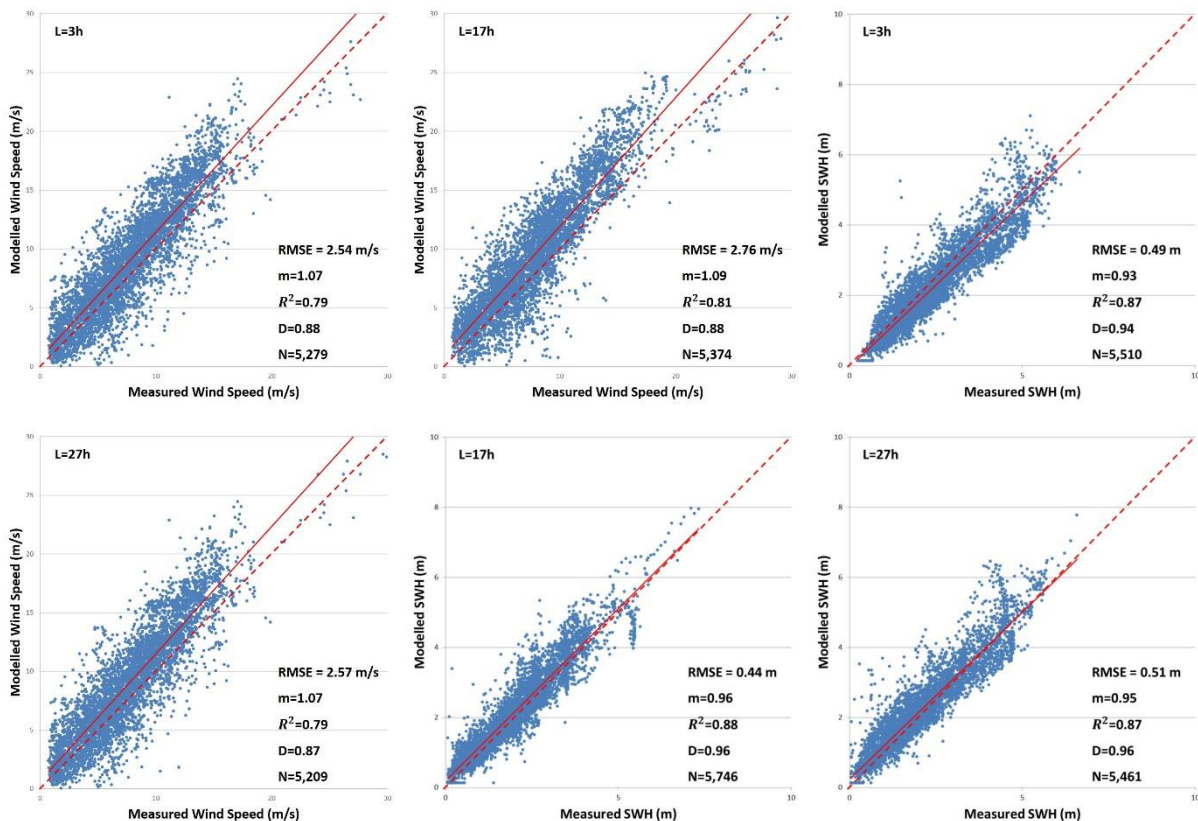
Fig. 8.10 Comparison of wind speed (top row) and SWH (bottom row) for L=3h, L=17h and L=27h. Points represent data from satellites (SARAL/ALTIKA), solid line represents best-fit slope and dashed line represents slope of unity.

The statistical measures provided in some of the figures do not inform the user about the probability of forecasted event actually occurring. In other words, the probability of each forecasted condition actually occurring must be estimated. We reproduce the methods described in Singhal et al. (2010). Two methods have been used: (1) the RMSE method and (2) the absolute error method. For both the methods, we first quantified all forecasted SWHs into distinct groups from 0–1.5, 1.5–3, 3–5, 5–8, and 8–10 m. Grouping of SWHs based on the predicted values rather than on data is necessary since the measurements are not known a priori. The measured data points were then extracted for each predicted SWH group. For the first method, the RMSE for each predicted SWH group was estimated. Then, the difference between each predicted SWH and the corresponding measured value was calculated. The percentage of data points for which this difference fell within specified intervals was estimated. The intervals chosen are 0.5, 1.0, and 1.5 times the RMSE. For the second method, the absolute error for each predicted SWH was computed, and the percentages of values that fell within 15, 25, and 35% absolute errors were estimated.
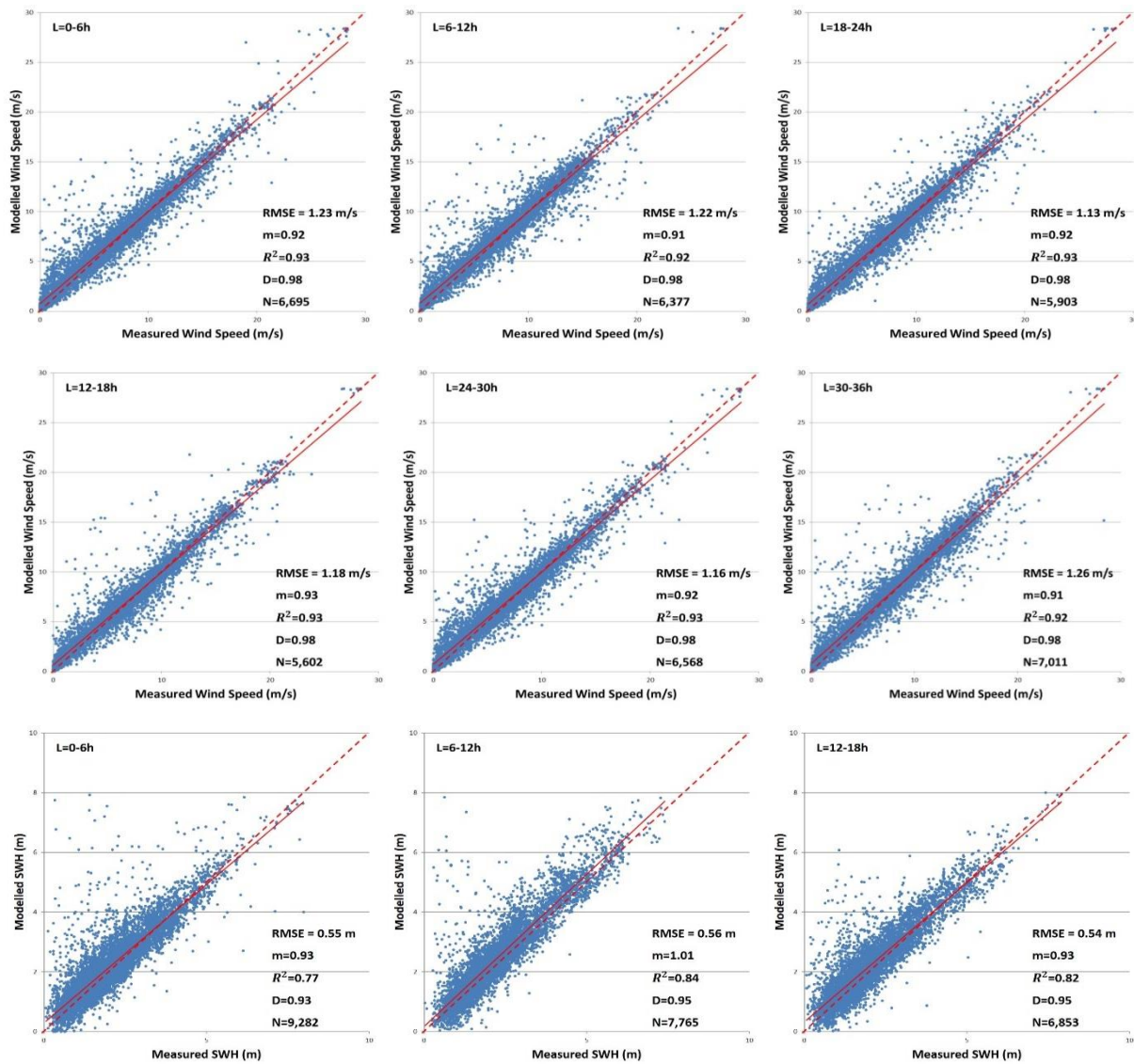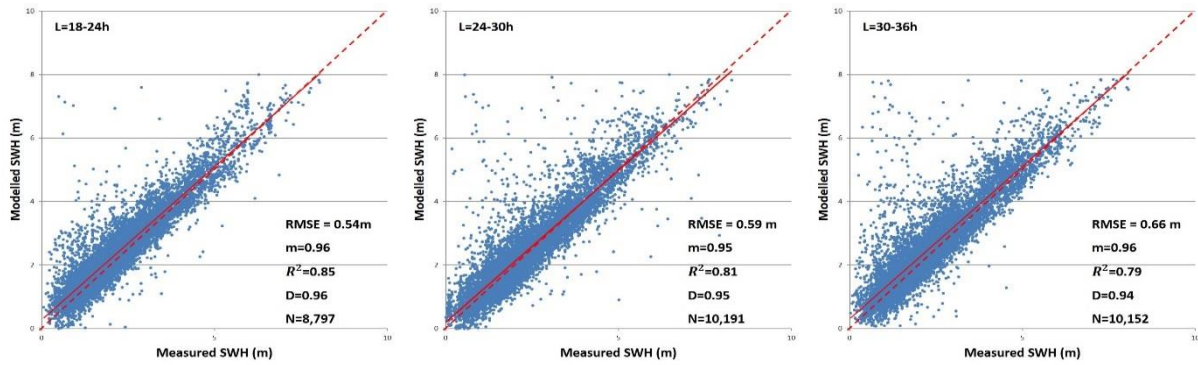
Fig. 8.11 Comparison of wind speeds (top two rows) and SWHs (bottom two rows) for L=0-6 h, L=6-12 h, L=12-18 h, L=18-24 h, L=24-30 h and L=30-36 h. Points represent data from 2 satellites (JASON-2 and CRYOSAT-2), solid line represents best-fit slope and dashed line represents slope of unity.

The above analyses are performed separately for L=3, 17, and 27h. The results are summarized in Table 8.5 (SARAL/ALTIKA only). For the most part, the RMSE increases with increasing SWHs. The results in Table 1 can be demonstrated by an example for L=3h, for instance. The results indicate that the predictions that fell in the 1.5-3.0 m range have an RMSE = 0.44 m. Further, a wave height predicted in this range would have an 87% chance of actually being between 1.06 and 3.44 m (1.5-1×RMSE and 3.0+1×RMSE). Similarly, for the L=17h forecast that falls in the 3m –5m interval, there would be a 62% chance of the actual conditions being between 2.68m (3-0.5×RMSE) and 5.32m (5+0.5×RMSE).

Table 8.5 Distribution of deviations between predicted SWHs and SARAL/ALTIKA data

			Probability of occurrence							
	Predicted		RMSE bound				Absolute error bound			
L	SHW group	RMSE					15	25	35	Samples
(h)	(m)	(m)	0.5	1	1.5		(%)	(%)	(%)	(N)
3h	0.0-1.5	0.37	0.76	0.93	0.97		0.29	0.57	0.81	1904
	1.5-3.0	0.44	0.71	0.87	0.95		0.54	0.81	0.94	2281
	3.0-5.0	0.65	0.59	0.75	0.87		0.61	0.90	0.97	1148
	5.0-8.0	0.83	0.66	0.75	0.81		0.68	0.83	0.93	177
	8.0-10.0	-	-	-	-		-	-	-	
	Overall	0.49	0.72	0.86	0.93		0.47	0.75	0.90	5510
17h	0.0-1.5	0.29	0.83	0.93	0.96		0.46	0.64	0.74	1943
	1.5-3.0	0.37	0.78	0.90	0.95		0.60	0.83	0.92	2442
	3.0-5.0	0.65	0.62	0.78	0.88		0.58	0.80	0.91	1259
	5.0-8.0	0.80	0.54	0.71	0.81		0.65	0.82	0.93	102
	8.0-10.0	-	-	-	-		-	-	-	
	Overall	0.44	0.77	0.88	0.93		0.55	0.76	0.86	5746
27h	0.0-1.5	0.27	0.86	0.93	0.96		0.49	0.68	0.78	1795
	1.5-3.0	0.44	0.77	0.87	0.93		0.60	0.78	0.85	2365
	3.0-5.0	0.66	0.66	0.84	0.91		0.65	0.86	0.91	1101
	5.0-8.0	1.32	0.58	0.73	0.81		0.52	0.72	0.82	200
	8.0-10.0	-	-	-	-		-	-	-	
	Overall	0.51	0.78	0.88	0.93		0.57	0.76	0.84	5461

Using the absolute error method, for L=27h, a prediction between 5m and 8m would have an 82% of chance of experiencing a sea state between 3.25m (5m-0.35%) and 10.8m (8m+35%).

Probability estimates relating to the likelihood of a prediction representing an actual sea-state are summarized in Table 8.6 based on data from JASON-2/CRYOSAT-2. Again, the RMSE's increase with increasing SWHs, and are approximately 15% of the mean wave heights for that range. By way of demonstration, the results in Table 8.6 indicate that for L=12-18h, the predictions that fall in the 1.5-3m range have an RMSE of 0.41 m, and that these predictions would have a 91% chance of actually representing a sea-state between 1.06 and 3.44 m (1.5-1×RMSE and 3.0+1×RMSE). Similarly, for the 18-24L forecast that fells in the 3m –5m interval, there would be a 72% chance of the actual conditions being between 2.68m (3-0.5×RMSE) and 5.32m (5+0.5×RMSE). Using the absolute error method, for L=24-30h, a prediction of 5m-8m would have an 78% of chance of experiencing a sea state between 3.75m (5m-0.25%) and 10.0m (8m+25%).

The above analysis represents a relatively novel but truly useful method of assessing forecast reliability. The comprehensive assessment of the results presented in Figs 8.10 and 8.11 suggests that the predictions are close to reality, and the data in Tables 8.5 and 8.6 demonstrate that the forecast system provides results which are within 0.5*RMSE of the actual sea-state approximately 75% of the time. This enhances the practical benefit of the system to the user of the forecasts.

Table 8.6 Distribution of deviations between predicted SWHs and JASON-2 and CRYOSAT-2 data

			Probability of Occurrence						
L (h)	Predicted SHW group (m)	RMSE (m)	RMSE bound			Absolute error bound			Samples (N)
			0.5	1	1.5	15 (%)	25 (%)	35 (%)	
0-6h	0.0-1.5	0.33	0.82	0.93	0.96	0.43	0.65	0.79	2790
	1.5-3.0	0.44	0.77	0.89	0.94	0.58	0.77	0.86	4683
	3.0-5.0	0.78	0.73	0.83	0.89	0.66	0.80	0.85	1620
	5.0-8.0	1.82	0.74	0.75	0.79	0.70	0.76	0.80	189
	Overall	0.55	0.81	0.91	0.94	0.55	0.74	0.84	9282
6-12h	0.0-1.5	0.32	0.83	0.92	0.96	0.45	0.65	0.79	2028
	1.5-3.0	0.41	0.79	0.90	0.95	0.60	0.80	0.88	3719
	3.0-5.0	0.77	0.67	0.82	0.88	0.56	0.75	0.85	1619
	5.0-8.0	1.31	0.64	0.77	0.83	0.61	0.77	0.87	399
	Overall	0.56	0.53	0.61	0.64	0.55	0.75	0.85	7765
12-18h	0.0-1.5	0.32	0.81	0.92	0.97	0.39	0.61	0.75	1948
	1.5-3.0	0.41	0.77	0.91	0.95	0.58	0.78	0.87	3309
	3.0-5.0	0.57	0.65	0.83	0.92	0.64	0.84	0.92	1196
	5.0-8.0	0.55	0.57	0.77	0.91	0.79	0.99	1.00	152
	Overall	0.43	0.76	0.89	0.94	0.54	0.74	0.84	6605
18-24h	0.0-1.5	0.35	0.81	0.92	0.96	0.41	0.62	0.76	2378
	1.5-3.0	0.52	0.75	0.88	0.93	0.47	0.68	0.80	3665
	3.0-5.0	0.79	0.69	0.83	0.88	0.62	0.76	0.85	1629
	5.0-8.0	0.89	0.61	0.77	0.87	0.67	0.90	0.96	383
	Overall	0.57	0.77	0.88	0.92	0.49	0.69	0.80	8055
24-30h	0.0-1.5	0.37	0.80	0.91	0.96	0.37	0.60	0.76	3011
	1.5-3.0	0.45	0.76	0.89	0.94	0.59	0.78	0.87	4348
	3.0-5.0	0.77	0.72	0.84	0.88	0.67	0.83	0.90	2217
	5.0-8.0	1.39	0.68	0.80	0.84	0.62	0.78	0.86	615
	Overall	0.59	0.79	0.90	0.94	0.56	0.74	0.84	10191
30-36h	0.0-1.5	0.37	0.80	0.92	0.96	0.39	0.62	0.78	2838
	1.5-3.0	0.47	0.77	0.89	0.93	0.58	0.78	0.86	4753
	3.0-5.0	0.75	0.72	0.84	0.89	0.65	0.80	0.87	2497
	5.0-8.0	1.36	0.67	0.80	0.85	0.61	0.79	0.87	666
	Overall	0.61	0.79	0.89	0.93	0.55	0.74	0.84	10754

CHAPTER 9. SUMMARY AND CONCLUDING REMARKS

The previous chapters have described a comprehensive effort to develop a regional operational wave forecasting system for Cook Inlet. The system is intended to supplement NCEP's efforts in the Pacific Ocean. It uses wave boundary conditions from NCEP's forecasts but places emphasis on enhancing local representation. This is accomplished in three ways. First, a finer grid (~1.5 km by 1.5 km) is used in much of the domain; additionally, nested domains for Kachemak Bay and Upper Cook Inlet (Anchorage area) are used. Second, currents and water levels are also modelled, and the effect of changing currents and water levels (i.e. flooding and drying in the two nested domains) is included. Third, a regional wind model, operated by the Alaska Experimental Forecast Facility at the University of Alaska, is used to obtain local wind-fields that force the wave/current models.

Each component of the system has been rigorously investigated, and hindcasts have been used, along with available data, to guide the development of the forecasting system. Numerous examples have been provided that demonstrate that the system components as well as the integrated system yield simulations that are realistic. Significantly, data from three satieties, SARAL/ALTIKA, JASON2, and CRYOSAT2 were used to assess forecast reliability. The system was largely successful in forecasting wave conditions that come to pass a few hours after the forecast was made. The system produces 36-hours forecasts once a day. The maximum lead time available for comparison, based on satellite flight protocols, were 27 hours SARAL/ALTIKA and 30-36 hours for the other two satellites. Even for these lead times, the forecasted SWH's were within ±(0.5*RMSE) over 75% of the time, for the most part. The RMSE's themselves were about 20% of median interval in which the forecast fell. Thus the user can use the forecasts with confidence and also use Tables 8.5 and 8.6 to ascertain the likelihood of a forecasted event coming to pass.

The integrated system is at present operated at Texas A&M University and the results are placed on the websites mentioned in Chapter 7. We can transfer the software to the Anchorage NWS office on request.

Three doctoral students at Texas A&M University contributed to this project, to varying degrees. The following publications (see Appendix) have resulted from this work:

- Singhal, G., Panchang, V.G., Horrillo, J., and Jeong, C.K. (2011). "Reliability and Efficiency of a Coupled Wind-Wave-Current Forecasting System for Cook Inlet, Alaska." Solutions to Coastal Disasters, Anchorage, Alaska, USA, 109-119.
- Singhal, G., Panchang, V.G., and Nelson, A.J. (2013). "Sensitivity assessment of wave heights to surface forcing in Cook Inlet, Alaska." Continental Shelf Research, 63(S15), S50-S62.
- Sharma, A., Choi, M., and Panchang, V.G. (2015). "Development and Validation of an Operational Forecasting System for Waves and Coastal Flooding and Drying in Cook Inlet, Alaska." Coastal Structures and Solutions to Coastal Disasters, Boston, Massachusetts, USA, 238-246.
- Choi, M. and Panchang, V.G., (2017). "Operational Wave Forecast Reliability in Cook Inlet, Alaska", *MTS/IEEE OCEANS 17,* Anchorage, Alaska, submitted.

A paper describing forecast reliability using satellite data and contrasting a high wave environment (Cook Inlet, AK) and low wave environment (Persian Gulf) is in preparation.

REFERENCES

Allard, R.A., Dykes, J.D., Hsu, Y.L., Kaihatu, J.M., Conley, D. 2008. A real-time nearshore wave and current prediction system. *J. Marine Systems*, 69, 37-58.

Bidlot, J.R., Holmes, D.J., Wittmann, P.A., Lalbeharry, R. and Chen, H.S., 2002. Intercomparison of the performance of operational ocean wave forecasting systems with buoy data. *Weather and Forecasting*, *17*(2), pp.287-310.

Booij, N., Ris, R.C., Holthuijsen, L.H. 1999. A third-generation wave model for coastal region: 1. Model description and validation. *J. Geophys. Res.* 104 (C4), 7649-7666.

Chen, Q., Wang, L., Zhao, H., Douglass, S.L. 2007. Prediction of storm surges and wind waves on coastal highways in hurricane-prone areas. *J. Coast. Res.* 23(5), 1304 – 1317.

Dykes, J. D., D. W. Wang, and J. W. Book, 2009. An evaluation of a high-resolution operational wave forecasting system in the Adriatic Sea. J. Marine Systems, 78, S255-S271.

Egbert, G.D. and Erofeeva, S.Y. 2002. Efficient inverse modeling of barotropic ocean tides. *J. Atmos. Oc. Tech.* 19(2), 183-204.

Funakoshi, Y., Hagen, S.C., Bacopoulos, P. 2008. Coupling of hydrodynamic and wave models: Case study for Hurricane Floyd (1999) hindcast. *J. Waterway, Port, Coastal and Ocean Engg.* November, 321-335.

Hamrick, J.M. 1992. A three-dimensional environment fluid dynamics computer code: theoretical and computational aspects. Special Report 317. The College of William and Mary, Virgina Institute of Marine Science, Williamsburg, Virgina, 63pp.

Ji, Z.-G., Morton, M.R., Hamrick, J.M. 2001. Wetting and drying simulations of estuarine processes. *Estuar., Coastal, and Shelf Sci.* 53, 683-700.

Jin, K.-R., Hamrick, J.H., Tisdale, T. 2001. Application of a three-dimensional hydrodynamic model for Lake Okeechobee. *J. Hydraulic Engg.* 126, 758-771.

Johnson, M. 2008. Water and ice dynamics in Cook Inlet. Final Report, OCS Study MMS 2008-061. Mineral Management Service, p. 106.

Kuo, A.Y., Shen, J., Hamrick, J.M. 1996. The effect of acceleration on bottom shear stress in tidal estuaries. *J. Waterway, Port, Coastal, and Ocean Engg.* 122, 75-83.

Liu, H., Olsson, P.Q., Volz, K.P., Yi, H. 2006. A climatology of mesoscale model simulated low- level wind jets over Cook Inlet and Shelikof Strait, Alaska. *Estuar., Coastal and Shelf Sci.* 70, 551-566.

Longuet-Higgins, M.S. and Stewart, R.W. 1964. Radiation stress in water waves; a physical discussion, with applications. *Deep-Sea Research,* 11, 529 – 562.

Mitsuyasu, H., Tasai, F., Subara, T., Mizuno, S., Ohkusu, M., Honda, T., Rikiishi, K. 1975. Observations of the directional spectrum of ocean waves using a clover-leaf buoy. *J. Phys. Oceanogr.* 5, 750 – 760.

Oey, L.-Y., Ezer, T., Hu, C., Muller-Karger, F.E. 2007. Baroclinic tidal flows and inundation processes in Cook Inlet, Alaska: numerical modeling and satellite observations. *Ocean Dynamics*, 57, 205-221.

Okkonen, S.R. and Howell, S.S., 2003. *Measurements of temperature, salinity and circulation in Cook Inlet, Alaska*. US Minerals Management Service, Alaska OCS Region.

Olsson, P.Q., Volz, K.P. and Liu, H., 2013. Forecasting near-surface weather conditions and precipitation in Alaska's Prince William Sound with the PWS-WRF modeling system. *Continental Shelf Research*, *63*, pp.S2-S12.

Panchang, V.G., Jeong, C., and Li, D. 2008. Wave climatology in coastal Maine for aquaculture and other applications." *Estuaries and Coasts*, 31, 289-299.

Panchang, V., C.K, Jeong, and Z. Demirbilek, 2013. Analyses of extreme wave heights in the Gulf of Mexico for offshore engineering applications. *J. Offshore Mech. Arctic Engineering*, 135, 031104

Plant, N.G., Edwards, K.L., Kaihatu, J.M., Veeramony, J., Hsu, L., Holland, K.T. 2009. The effect of bathymetric filtering on nearshore process model results. *Coastal Engg,* 56, 484-493.

Ris, R.C., Booij, N., Holthuijsen, L.H. 1999. A third-generation wave model for coastal regions: part II verification. *J. Geophys. Res.* 104 (C4), 7667-7681.

Shen, J., Boon, J., Kuo, A.Y. 1999. A numerical study of a tidal intrusion front and its impact on larval dispersion in the James River estuary. *Estuaries,* 22, 681- 692.

Singhal, G., Panchang, V.G., Lillibridge, J.L. 2010. Reliability assessment for operational wave forecasting system in Prince William Sound, Alaska. *J. of Waterway, Port, Coastal, and Ocean Engg*, 136(6), 337-349.

Singhal, G., Panchang, V.G. and Nelson, J.A., 2013. Sensitivity assessment of wave heights to surface forcing in Cook Inlet, Alaska. *Continental Shelf Research*, *63*, pp.S50-S62.

Smith, O., Khokhlov, A., Zieserl, M., 2005. Water property, sediment, tide, and current measurements and analyses in the vicinity of the proposed Knik Arm Bridge. Contract Report for URS and HDR, sponsored by Knik Arm Bridge and Toll Authority.

Smith, S.J., Peterson, M.D., Pratt, T.C. 2010. Numerical modeling studies supporting port of Anchorage deepening and expansion; Part II: measuring physical processes. Proc. Estuarine and Coastal Modeling Conference (ECM 11), Seattle, WA, 286-300.

Stabeno, P.J., Bond, N.A., Hermann, A.J., Kachel, N.B., Mordy, C.W., Overland, J.E. 2004. Meteorology and oceanography of the northern Gulf of Alaska. *Contin. Shelf Res.* 24, 859 – 897.

Tolman, H. L. 2009. User manual and system documentation of WAVEWATCH III version 3.14. NOAA/NWS / NCEP/ MMAB Technical Note 276, 194 pp. + Appendices.

Appendix : Publications

G. Singhal et al. / Continental Shelf / Research 63 (2013) S50-S62

Research papers

ave heights to surface forcing in Cook

Sensitivity assessment of w Inlet, Alaska

ang [a,b], James A. Nelson [c]

Gaurav Singhal [a,b,*], Vijay G. Panch

[a] *Maritime Systems Engineering, Texas A&M University at G*
alveston, 200 Seawolf Parkway, Galveston, TX 77553, USA
University, College Station, TX 77840, USA
Sand Lake Road, Anchorage, AK 99502, USA

[b] *Coastal and Ocean Division, Civil Engineering, Texas A&M*
[c] *National Weather Service, Anchorage Forecast Office, 6930*

A R T I C L E   I N F O

A B

S T R A C T

ng tidal forcing combined with complex winds and currents make wave modeling quite challenging
Cook Inlet (CI), Alaska. Using a coupled wind-wave–current modeling approach, we conducted a
sitivity analysis of the environmental factors that impact the modeling predictive skill for waves. A
th-averaged circulation model forced by the winds, tides, and river input was shown to replicate
sured flow velocities (NOAA data obtained in 2005) with high correlation coefficients ($R^2 > 0.8$).
ve–current interaction is examined by one-way and two-way coupling of the wave and circulation
dels for a 12-day period that included multiple storm events. On average, it is found that significant
e heights (SWHs), which were originally < 2 m, increase by about 0.5 m in the presence of currents
h speeds up to 3 m/s). While the effect of currents on larger SWHs (> 2 m) was found to be
imal. On the other hand, the effect of waves on the currents was found to be marginal, which
cated that two-way coupling between the models may be unnecessary. Artificial adjustment to the
ents (to account for possible errors and uncertainties in the circulation model such as baroclinic
ing, winds, and other effects) had only a small effect on the predicted SWHs resulting from the
pled model (< 10 cm, on average). On the other hand, errors in the wind-fields and wave open
ndary conditions resulted in substantial errors in the modeled SWHs. Overall, the experiments
ied out here suggest that for forecasting purposes, one-way coupling would be adequate; two-way
pling, albeit incorporating better physics, has less of an effect on the accuracy of the forecast than
roved wind-fields.

and Drift River. Other marine traffic is related to the recreation, tourism, and the commercial fishing industries.

1. Introduction

les long) stretching
uth-central Alaska
n activity (such as
roximately half of
nchorage, between
Alaska's largest city
ustry, and tourism.
building materials,
y to over 80% of
installations; while
pping routes in CI
s of Nikiski, Homer,

CI is also an extremely dynamic system. Exposure on three sides to the Gulf of Alaska, where the waves are among the largest in the world, renders human activities in CI vulnerable to complex and dangerous ocean conditions. Often, wave heights greater than 7 m are observed by the buoys near the entrance to the inlet (Fig. 1). There are also large tidal variations (about 8–9 m, the largest in the US) and the complex bathymetry and coastal morphology result in large tidal currents. For example, tidal bores are commonly found in Turnagain Arm, creating currents in excess of 2–3 m/s. Currents on the order of 1–2 m/s also occur throughout the inlet during full tidal flow. There is also significant wave/current action and during low tide, silty bottoms (mudflats) are exposed which cause navigation difficulties including the grounding of boats during low tide (e.g. Anchorage Daily News, 9/9/2011). In addition, the interaction of rugged topography (mountain ranges with elevations that abruptly rise to 3000 m, gaps, and channels) with the strong atmospheric pressure gradients results in the so-called "gap winds" that adversely affect

Cook Inlet (CI) is a large estuary (~180 mi from the Gulf of Alaska to Anchorage in so (Fig. 1) that experiences a great deal of huma shipping, oil and gas extraction, etc.). App Alaska's population lives along CI's shores. A Turnagain and Knik Arms at the head of CI, is and a center of transportation, commerce, ind The Port of Anchorage receives food, fuel, durable and expendable supplies for delive Alaska's population and to four large military seafood, minerals, and gas are exported. Shi serve the port year-round, as well as the ports

ing, Texas A&M Univer-
553.

ghts reserved.

*Corresponding author at: Maritime Systems Engineer
sity at Galveston, 200 Seawolf Parkway, Galveston, TX 77
Tel.: +1 409 740 4555.
E-mail address: singhalg@tamu.edu (G. Singhal).

Fig. 1. General region of CI. Color represents bathymetry (in meters) with respect to mean-sea-level; red circles represent weather stations, and diamonds represent buoy locations.

"Advanced Circulation" (ADCIRC) for various applications. Further, both of these latter studies were done in hindcast mode where computational efficiency was not an issue. In the forecasting mode, on the other hand, efficiency becomes a critical consideration so that the output may be provided in reasonable time.

The viability of interconnecting multiple models (i.e. winds, waves, and currents) in a dynamic environment such as CI presents unique challenges. Our interest here is to identify and include those phenomena in regional forecasting schemes that significantly influence the waves, but without expanding the cost and effort required to generate the forecast. An integrated wave forecasting scheme for CI should include the complex effects induced by the winds, currents, and water levels on the SWDs. These sharp topographic gradients produce complex wind regimes that should be properly modeled in order to obtain reliable simulations of both waves and currents. For this study, the wind forecasts are provided by the researchers from University of Alaska, Fairbanks (UAF), who are responsible for wind model development, implementation, improvement, and validation (a topic addressed elsewhere in this issue, Olsson and Volz, this issue). Thus, at present we have no control over the wind fields, however, a brief assessment of the winds, to the extent possible, is performed in this study.

As for the wave–current interaction, the strong currents in CI created by tides, winds, and other mechanisms (e.g. baroclinic forcing) can influence the waves (a strong opposing current can increase the wave height and steepness). The waves, in turn, could affect the currents by transferring their momentum to currents through gradients of radiation stress (Longuet-Higgins and Stewart, 1964), Stokes drift, and modified wind stress. The dynamic feedback between the waves and the currents should thus be addressed in CI wave forecasting. While the wave field can be obtained using a suitable wave model, they are usually influenced by the quality of the winds and the wave open boundary conditions (WOBCs) available for a regional forecast scheme. For developing hydrodynamic fields using a suitable circulation model the question of efficiency (2D vs. 3D; barotropic vs. baroclinic) must be investigated, i.e. the mode in which circulation model must run. This choice and the consequent assumptions can create inaccuracies in the results, as can the quality of the forcing functions, i.e. wind input, river discharge; none of which are accurately known.

Next, the issue of coupling the wave and circulation model is investigated using one-way and two-way approaches. The efficiency and accuracy of both coupling approaches as well as the influence of the time interval for information exchange between the two models on the results and on modeling efficiency is addressed. Finally, the effects of errors on the final solution is examined. The integrated model consists of several components each containing errors due to physics as well as operational constraints. In the development of a practical forecasting scheme it may not be feasible to remedy all of the errors in the component models; nor is a remedy for all errors warranted since some of them may influence the final solution only to a small extent. Errors in the integrated model results are quantified by identifying corresponding errors in the input forcing functions (winds, currents, WOBCs, etc.). The identification and quantification of such errors could eventually serve as "guidance" for estimating the uncertainty associated with the wave forecasts, and to determine which aspects need improvement.

The paper is organized as follows. Section 2 provides a description of various bathymetric datasets available, along with a qualitative assessment of bathymetric patterns in the CI region. Section 3 describes the various modeling methods (e.g. wind, circulation, wave, coupled wave–current modeling), followed by Section 4 which provides validation for winds, depth-average

maritime and aviation activities during the winter season (Liu et al., 2006). Also important is the impact of the strong tidal flows through lower CI and out of the Gulf of Alaska. Given the paucity of wave observations in CI,[1] it is critical to provide accurate and timely forecasts of surface conditions through the use of state-of-the-art wave/circulation models.

Over the last few years, regional wave forecasting systems have been established for various locations around the world. These systems provide wave forecasts on high-resolution grids and are connected to coarse resolution global wave forecasts (Tolman, 2009) produced by the National Centers for Environmental Prediction (NCEP). Some examples include forecasted wave conditions in the Gulf of Maine (www.gomoos.com) and Prince William Sound (www.aoos.org), that utilize the wave model SWAN ("Simulating Waves Nearshore"— Booij et al., 1999; Ris et al., 1999) to provide high-resolution wave forecasts for up to 48 h (see Singhal et al., 2010 for details related to the Prince William Sound forecasting system). In some cases, the regional wave model is also coupled with the circulation model to account for wave–current interaction. For instance, wave forecasts in Humboldt Bay (provided by National Weather Service, Eureka) include the effect of tidal currents near the harbor entrance. Coupled forecasts of surface waves and currents are also provided by the Naval Research Laboratory for the Mississippi and Southern California Bights. However, the tidal range and magnitude of the currents at these locations are not as extreme as found in CI. They were similarly small in the studies of Chen et al. (2007) and Funakoshi et al. (2008), who coupled SWAN and

[1] As of February 2010, no buoys within CI are functional. Buoy 46105 near Stevenson Passage only transmitted data from August to December 2008, whereas Buoy 46106 in central CI stopped functioning in February 2010. It is not certain when NDBC would restore these buoys.

currents and water surface elevations (WSEs), and SWHs before integrating the components. In Section 5, we examine the performance of the integrated system, determine the effect of currents on the waves, and attempt to ascertain how errors in the individual components affect the overall result. Conclusions are presented in Section 6.

2. Bathymetry

Bathymetry is one of the most critical aspects regarding the performance of any coastal model. Plant et al. (2009) showed the influence of bathymetric filtering on wave and flow fields, and found that the model results were extremely sensitive to the resolution of input bathymetry. NOAA's National Geophysical Data Center provides various bathymetric datasets for CI such as Etopo1/Etopo2 Global Relief Models, Tsunami Inundation Digital Elevation Model (DEM; NOAA Center for Tsunami Research), etc. The Etopo datasets have a fairly low resolution (1 min and 2 min) and do not properly resolve many complex bathymetric features of CI, while the DEM dataset is available at a 24 s resolution, presently the highest resolution available for CI region. We therefore used the DEM, however, it does not cover some regions of the northern CI (especially the Turnagain Arm). To compensate for the missing bathymetry in the Turnagain Arm region, past surveys (done by the National Ocean Service) along with the navigational charts were utilized. These data were interpolated onto the existing DEM to generate a more reliable bathymetry (a similar approach was used by Oey et al., 2007). Fig. 1 shows the updated CI bathymetry using the DEM dataset. In general, the depths decrease from about 200 m near Stevenson Passage (in the south) to about 50 m in the central inlet. The depths also show cross-shore variability in many regions. For instance, the depths reduce from > 50 m to less than 10 m across the channel near the Forelands. Overall, CI is mostly shallow with an average depth of about 50 m.

3. Modeling methodology

3.1. Wind modeling

CI experiences very complex and dynamic weather patterns. During the winter season, winds in the northern Gulf of Alaska are a result of cyclonic storm systems off the Pacific and attain maximum strength from October through March (Stabeno et al., 2004). It is critical to reliably model such complex weather patterns (such as the strong gap winds; Liu et al., 2006) for forecasting purposes, since it is frequently stated that the quality of wave model predictions are most dependent on the quality of the input winds. Unfortunately, there are only six weather stations – Amatuli Island (AMAA2), Augustine Island (AUGA2), Flat Island (FILA2), Drift River (DRFA2), Nikiski (NKTA2), and Anchorage (ANTA2) – that provide a synoptic snapshot of wind patterns in the CI, and these are too few to obtain an accurate description of weather patterns over the entire region (Fig. 1).

Over the last few years, NCEP's "North-American Mesoscale" (NAM) model, which assimilates satellite-based measurements, has provided a synoptic snapshot of surface winds over the global ocean. However, the NAM winds do not properly account for coastal topographical variations, their resolution is much too coarse, and often do not extend into several coastal domains (e.g CI, Prince William Sound, etc.). Since early 2007, operational weather forecasts using the "Weather Research and Forecasting" (WRF) model have become available (http://aeff.uaf.alaska.edu/). These provide better coverage of the CI domain and use

resolutions fine enough (~4 km) to resolve the salient features of the underlying topography. Details of the WRF model are discussed elsewhere in this issue (Olsson and Volz, this issue). While there are some errors in the WRF predictions (described later), Singhal et al. (2010) found their effect on wave predictions to be marginal. For this study, hence, we have used the WRF winds, obtained through the link noted above, to force the wave and circulation models (note that investigating the effect of waves and currents on the wind-fields was not feasible).

3.2. Circulation modeling

CI circulation is mostly tidally driven with M2 being the predominant constituent. The natural resonant frequency of CI is roughly equivalent to that of the tidal frequency, and as a result CI experiences some of the largest tidal fluctuations in the world. In addition, the tidal flow velocities intensify towards the north, with magnitudes reaching up to 3 m/s. Okkonen and Howell (2003) suggest that wind-driven and buoyancy-driven flows also contribute to the overall circulation patterns in CI. Tidal and baroclinic effects were also addressed in three-dimensional (3D) modeling studies by Oey et al. (2007) and Johnson (2008). Other observational studies, on the contrary, have noted that CI has a vertically well-mixed environment due to the strong tidal currents (Smith et al., 2005, 2010). While the aforementioned studies have addressed the circulation patterns and their seasonality in CI, how these affect the wave climate, in general, has yet to be understood.

For circulation modeling purposes, the US Environmental Protection Agency's "Environmental Fluid Dynamics Code" (EFDC) model is utilized, which solves the 3D, vertically hydrostatic, free surface, turbulent-averaged equations of motion for a variable density fluid (Hamrick, 1992). The EFDC model can be run in barotropic or baroclinic and in 2D or 3D modes. It also has the capability of simulating wetting and drying processes (Ji et al., 2001), and has been tested and verified in a wide range of hydrodynamic and environmental studies (e.g. Kuo et al., 1996; Shen et al., 1999; Jin et al., 2001). It is thus a comprehensive circulation model, which enables us to operate it with different levels of physics to ascertain the appropriate level of effort needed for eventual wave–current modeling and forecasting.

3.3. Wave modeling

Due to the presence of dynamic and energetic local weather systems, waves in the northern Gulf of Alaska are among the largest in the world with SWHs frequently exceeding 5 m during the winter season. Thus, it is critical to predict such extreme events accurately in order to support the various maritime activities. NCEP provides continuous 7-day wave forecasts for the CI region using the multi-grid version of WAVEWATCH III model (hereafter, WW3; Tolman, 2009) on a spatial resolution of about 7 km. The NCEP wave forecasts, however, utilize the NAM winds which, as noted earlier, are much too coarse to properly account for the local topographical features. In addition, the NCEP wave forecasts do not include the effects of currents, which may also have a significant effect on surface waves.

Clearly, the CI wave model should account for such complexities in order to obtain reliable estimates of wave parameters. For this purpose, the SWAN model (version 40.81) was utilized. The model has been widely used for hindcasting and forecasting purposes (e.g. Allard et al., 2008; Singhal et al., 2010). Details of the SWAN model have been described in Booij et al. (1999) and Ris et al. (1999), and elsewhere, and thus are not included here.

59

3.4. Coupled wave–current modeling

Coupling between the wave and circulation models can be performed in two ways—(1) off-line coupling and (2) on-line coupling (commonly used terminology when coupling earth system models). In general, off-line coupling entails running the two models separately (in no particular order) for the entire duration of simulation (e.g. 2 days). The information can then either be transferred from one model to the other model (one-way approach), or it could be exchanged among both the models (two-way approach). In the one-way approach, the second model is executed using the output of the first model, whereas the two-way approach requires both models to be executed multiple times, while exchanging information, until the solution converges. On-line coupling, in contrast, invokes both models simultaneously. After a suitable time interval (e.g. 3 h), the two models exchange information and continue the simulation until the next communication time step. This technique avoids the use of multiple iterations as there is dynamic exchange of information among the two models during the simulation process. However, in between two information exchange time-steps, conditions are assumed to be steady. In contrast, in the one-way approach, the required information at all time-steps from the other model is precalculated. Thus, there are advantages and disadvantages associated with both the methods and the effects of these on the model accuracy and efficiency must be investigated.

In the context of the present work, the coupling of SWAN and EFDC was performed on a Macintosh computer with Quad-core processor (with hyper-threading) and 16 GB RAM. SWAN can run in parallel mode for multi-processor systems, whereas EFDC is only capable of running in serial mode. In this study, we have used the one-way off-line coupling (hereafter, C1W) and the two-way on-line coupling (hereafter, C2W). The purpose of using the two methods is to compare the wave model results with and without any coupling, and to address the question of which method is more efficient for forecasting purposes.

In the one-way approach, the simulation is started with EFDC which provides, by way of output, WSEs and flow velocities.

SWAN is then initiated with the EFDC output along with the other forcing terms (winds, WOBCs, etc.). For the on-line coupling, a simple interface was built using the shell scripting language. This interface controlled the execution of both the models simultaneously—starting from $t=0$, each model advances to the so-called "information exchange" time step when the models are stopped momentarily to exchange information (gradients of radiation stresses are transferred from SWAN to EFDC, whereas WSEs and flow velocities are transferred from EFDC to SWAN), after which the models continue the simulation until the next "information exchange" time-step, and so on. Thus, each model has information about the other model after each exchange, which is assumed steady until the next exchange. The results from the two coupling methods are compared to the results without coupling using two information exchange time-steps (1 h, 3 h); these model runs are named C1W-1 h, C1W-3 h, C2W-1 h, and C2W-3 h in the following discussion.

4. Validation of modeling components

Prior to integrating the various modeling components (winds, water levels, currents, waves), it is essential to ascertain their quality independently. It is to be noted that data availability poses a limitation to validation studies. While wind model (input) data are available for the time period after February 2007, current data are available only for the summer of 2005, and wave data are available for the fall of 2008.

4.1. Surface-winds from the WRF model

As stated earlier, the wind output was obtained from the WRF model run at UAF. Fig. 2 shows a sample comparison of wind speeds (in m/s) at various buoys and weather stations for the month of October 2008. It can be noticed that there is significant spatial variability in the observed wind speeds and, in general, the WRF model results are reasonable. For some nearshore locations (e.g. AMAA2, NKTA2, ANTA2), model errors seem to be significant
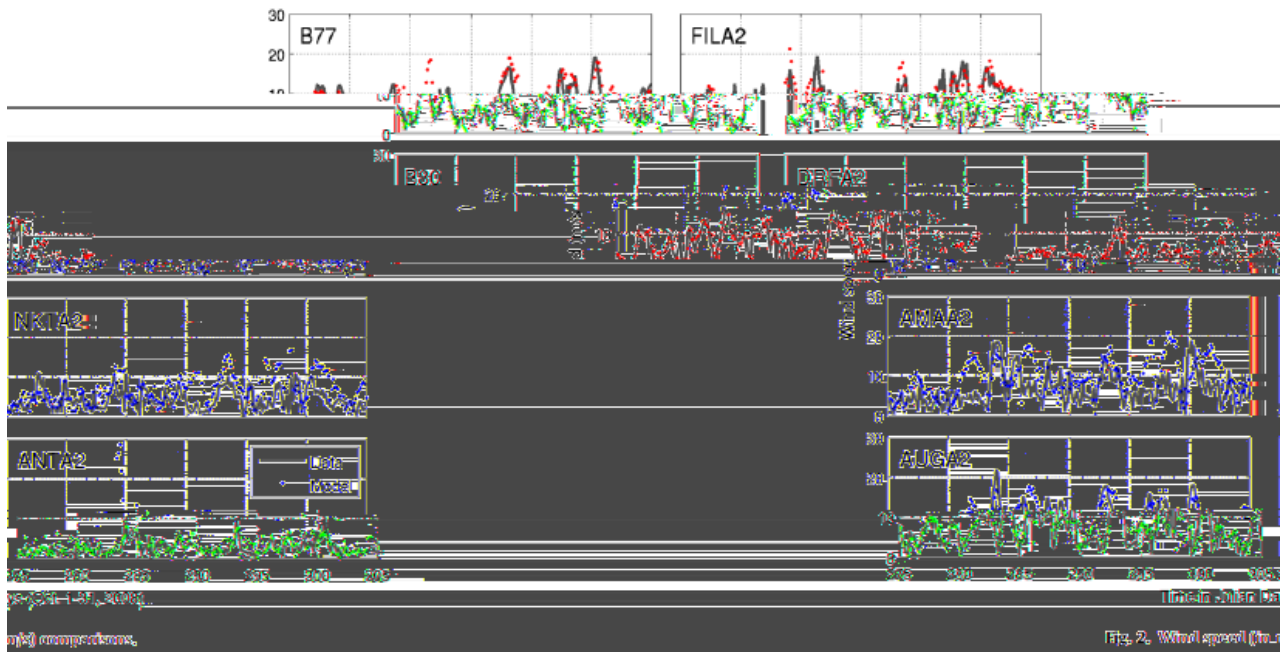
Fig. 2. Wind speed (in m/s) comparisons.

during some events (for instance, days 295–300 at AMAA2, day 285 at ANTA2, etc.). Although the 4 km resolution of WRF model seems reasonable for the CI region, it may be insufficient to resolve the sharp topographical gradients near the coastline and may have resulted in large errors at the locations noted above. Clearly, though, the effect of the errors in the WRF winds on the wave-fields must be determined. This is performed in Section 5.3. The comparisons for wind directions were reasonable at all the locations (not shown here).

4.2. Depth-averaged currents and WSEs from the EFDC model

The EFDC model was applied to the CI domain covering the region between −156°W to −149°W and 56°N to 61.5°N, on an irregular grid with a resolution of about 4 km at the open ocean boundaries, and decreasing to a resolution of ~1.5 km in the northern-most parts of CI (Fig. 3). Initially, the model was run in the depth-averaged mode, forced by tides, winds, and river discharge in the barotropic mode with a plan to advance to higher levels of physics (e.g. 3D, salinity and density effects, etc.), if needed.

The CI circulation model was tested via the simulation of tidal conditions for May–August 2005, coinciding with NOAA's comprehensive current measurement program (http://www.tidesand currents.noaa.gov/). Ten locations were selected from this survey for model comparison (current meter locations are shown in Fig. 3) in the lower CI (LCI) and central CI (CCI) regions (shown in Fig. 1; LCI region extends from 59° to 60°N, whereas CCI extends

from 60° to 60.75°N). Note that NOAA installed current meters first at five locations in the CCI for about a month (late May to early July, 2005), and then moved those to the LCI for another month (July–August 2005). Modeled WSEs are also compared to data from four tidal gauges (locations shown in Fig. 3). The model was initiated from motionless conditions on 1 May 2005 via prescription of tidal elevations and velocities at the open model domain boundaries (8 tidal constituents were included, viz. M2, S2, N2, K2, K1, O1, P1, and Q1). The corresponding boundary tidal elevations and velocities were extracted from TPXO6.2 global satellite-based tidal model (Egbert and Erofeeva, 2002). Further, monthly discharges from seven major rivers, as provided by US Geological Survey and Oey et al. (2007), were inputted to account for the mass introduced by the rivers into the domain. Winds from six weather stations and two NDBC buoys were also interpolated on the model grid to account for wind-driven circulation (please note that, during 2005, winds from the WRF model were not available).

The model results for WSEs (relative to mean sea level) are shown in Fig. 4. In the north, the tidal range increases from about 3 m at Kodiak Island to roughly 9 m at Anchorage. It can be seen that the model captured the observed tidal variability, which is significant, at all four locations. Table 1 shows the overall summary of statistical estimates of best-fit slope (m) and intercept (c), correlation coefficient (R^2), and root mean square error (RMSE) for about 3-month period (from 19 May to 1 August 2005) between the model and data. For the most part, the model results correlate with the data to a high degree (values of m and R^2 are in general larger than 0.88 and 0.86, respectively). Results at Anchorage, however, show a larger error compared to those at other locations; although the model predicted the tidal extremes correctly, the model results lagged the data by roughly 30 min. Such a lag can also be noticed in Fig. 5 of Oey et al. (2007) at Nikiski; at Anchorage, however, Oey et al.'s model predicted a somewhat early arrival of tides. At any rate, lack of precision in the prediction of WSEs near Anchorage can be potentially dangerous for mariners, given the large tidal range which causes extensive wetting and drying.

This type of mismatch in the timing of the tides could perhaps be attributed to the resolution used. In our model implementation, the resolution is 700 m × 1400 m in the vicinity of Anchorage, which is situated in a narrow, meandering channel in Knik Arm. To examine the effect of the resolution, a nested grid with a
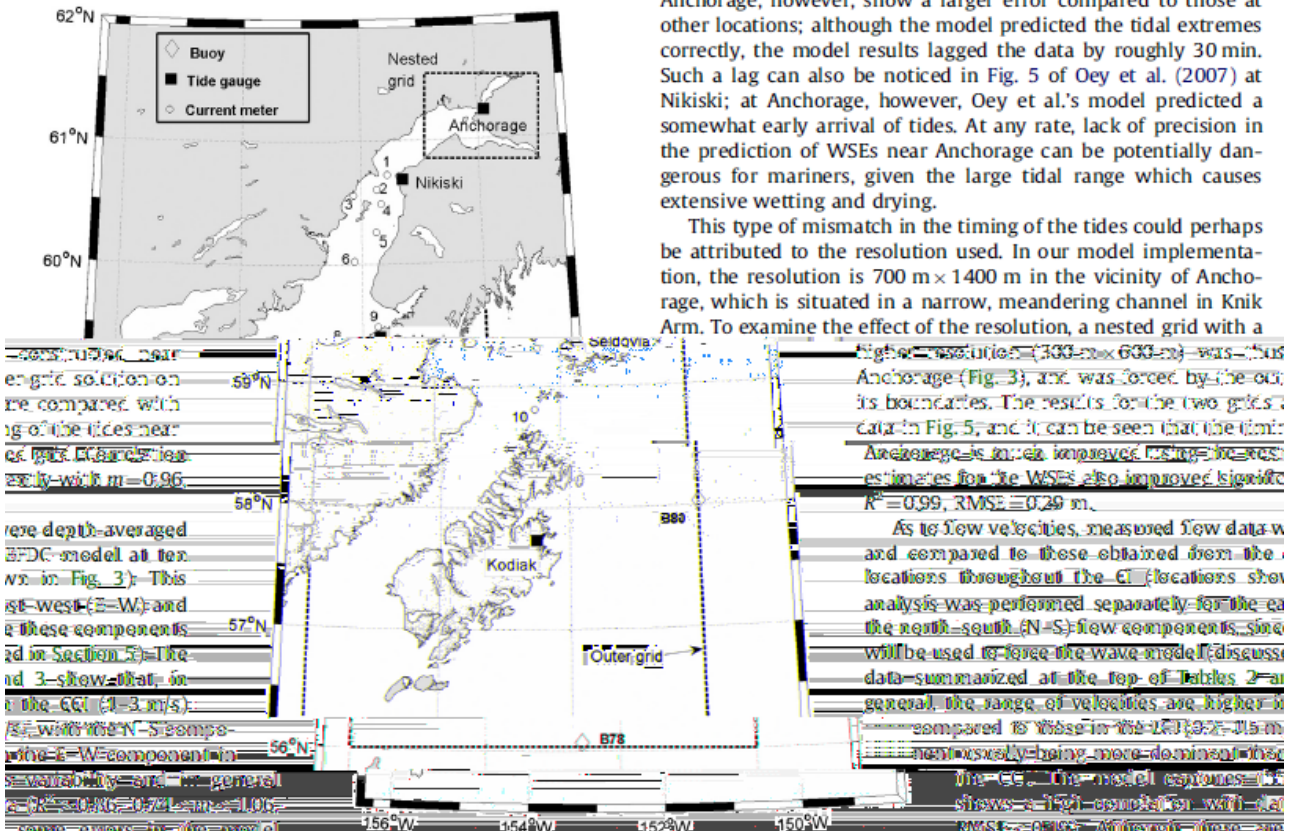

Fig. 3. Measurement locations of buoys, tide gauges, and current meters in CI. Note that current meters were deployed for a limited time in summer 2005. Dashed lines represent model boundaries for outer and nested grids.
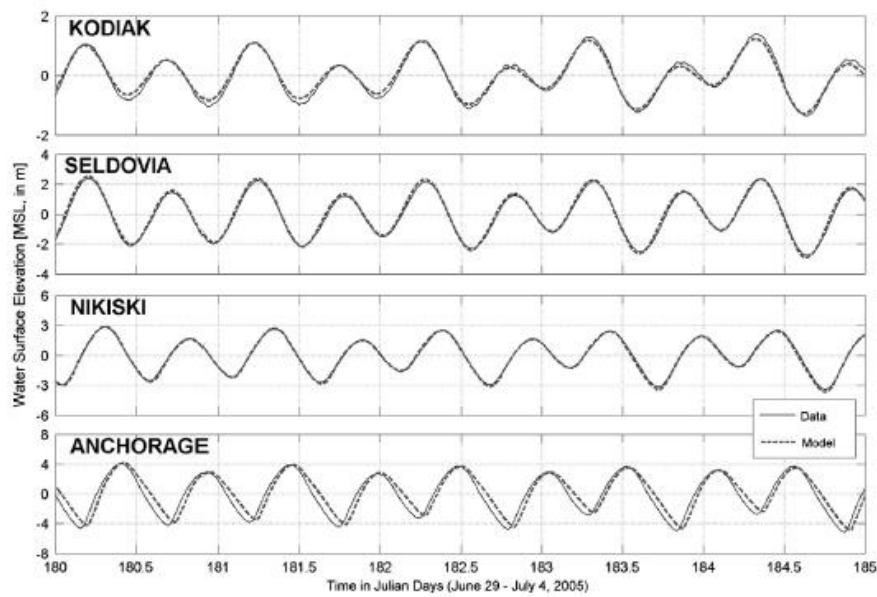
Fig. 4. WSE (relative to MSL, in m) comparisons.

Table 1
Statistical comparisons of WSE for the tide gauges. RMSE is in m, N is the sample size.

Measure	Kodiak	Seldovia	Nikiski	Anchorage
m	0.91	1.01	1.05	0.88
c	0.05	0.08	−0.02	0.28
R^2	0.98	0.99	0.99	0.86
RMSE	0.11	0.15	0.16	0.96
N	3553	3553	3553	3553
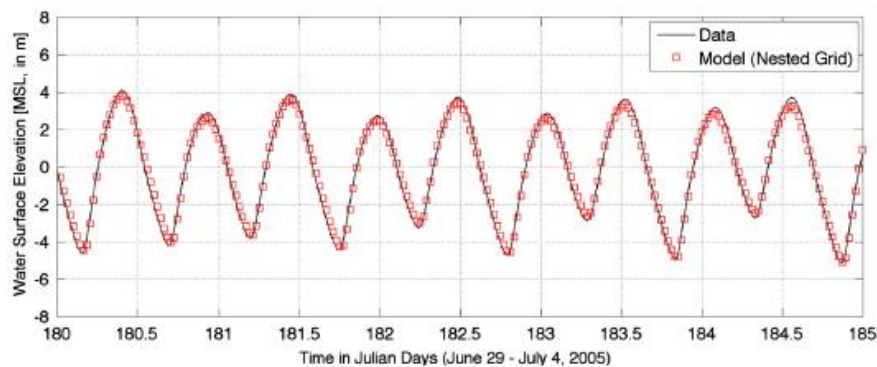
Fig. 5. WSE comparisons (relative to MSL, in m) at anchorage using the nested grid.

and it would appear that accounting for additional physics may not be warranted. Yet, a further explanation of the effects of possible residual/random errors on the wave-field is described in Section 5.3.3.

4.3. SWHs from the SWAN model

The SWAN wave model covered the same region as the circulation model, but at a resolution of about 1.5 km throughout the domain. SWAN was set up using the default options for wave generation (wind growth, quadruplet, and triad wave–wave interactions), wave breaking, bottom friction, etc. A model time step of 15 min was initially used. The wave model was forced by the WRF model that provided the output of winds every hour at a resolution of ~4 km. The WOBCs were obtained from the global WW3 model at the locations of Buoy 46078 (hereafter, B78) and Buoy 46080 (hereafter, B80). The full spectral output at B80 was forced along the east boundary, while the output at B78 was used to force the south boundary. Since the WW3 model, at present, does not provide full spectral output at locations near the west boundary, the output at B78 was also assumed along the west boundary (the validity of this assumption is discussed in Section 5.3.1).

Sample results obtained using the above model configuration are compared with buoy measurements for B05 and Buoy 46106 (B06) for a 12-day period in November 2008 (Fig. 6). The wave model, in general, seems to capture the variability in the SWHs,

62

Table 2
Statistical comparisons of depth-averaged flow velocities (m/s) for locations in the CCI. RMSE is in m/s, N is the sample size. Numbers in parentheses show minimum and maximum values for depth-averaged flow velocity components.

Measure	Forelands (1)		South of West Forelands (2)		Drift river (3)		East of Kalgin Island (4)		South-east of Kalgin Island (5)	
	E–W	N–S	E–W	N–S	E–W	N–S	E–W	N–S	E–W	N–S
Data (m/s) (min, max)	(−0.89, 0.64)	(−2.12, 2.32)	(−1.66, 1.69)	(−1.34, 1.02)	(−1.08, 1.02)	(−0.98, 1.00)	(−0.65, 0.86)	(−2.85, 2.11)	(−0.89, 0.94)	(−1.87, 1.47)
Model (m/s) (min, max)	(−0.99, 0.60)	(−2.16, 2.64)	(−1.75, 1.68)	(−1.44, 1.23)	(−0.84, 1.10)	(−0.64, 1.03)	(−0.9, 0.67)	(−3.04, 2.19)	(−1.13, 0.89)	(−2.01, 1.61)
m	0.97	0.94	0.98	1.06	0.91	0.77	0.99	0.96	0.97	0.95
c	0.01	0.02	0.07	0.04	0.06	0.03	−0.08	0.03	−0.09	0.03
R^2	0.86	0.98	0.96	0.97	0.95	0.94	0.94	0.99	0.96	0.98
RMSE	0.15	0.19	0.19	0.12	0.11	0.10	0.09	0.09	0.08	0.13
N	1489		1485		1530		1498		1503	

Table 3
Same as Table 2 but for locations in the LCI.

| Measure	West of Cape Ninilchik (6)		Augustine Island (7)		West of Kachemak Bay (8)		Seldovia (9)		Stevenson Passage (10)	
	E–W	N–S	E–W	N–S	E–W	N–S	E–W	N–S	E–W	N–S
Data (m/s) (min, max)	(−1.25, 0.82)	(−1.92, 1.49)	(−0.44, 0.23)	(−0.92, 0.70)	(−0.33, 0.26)	(−1.19, 1.22)	(−0.68, 1.01)	(−0.44, 0.64)	(−1.25, 1.13)	(−0.35, 0.81)
Model (m/s) (min, max)	(−1.21, 0.70)	(−1.94, 1.46)	(−0.36, 0.24)	(−0.92, 0.72)	(−0.24, 0.18)	(−1.31, 1.21)	(−0.75, 0.74)	(−0.48, 0.41)	(−1.15, 1.02)	(−0.63, 0.63)
m	0.89	0.96	0.89	0.98	0.74	1.01	0.95	0.94	0.92	0.95
c	−0.08	−0.08	0.003	−0.01	−0.01	−0.04	−0.05	−0.04	0.06	−0.14
R^2	0.96	0.98	0.87	0.95	0.75	0.99	0.89	0.92	0.91	0.87
RMSE	0.08	0.11	0.05	0.07	0.05	0.06	0.10	0.06	0.12	0.08
N	1441		1418		1412		1486		1448	
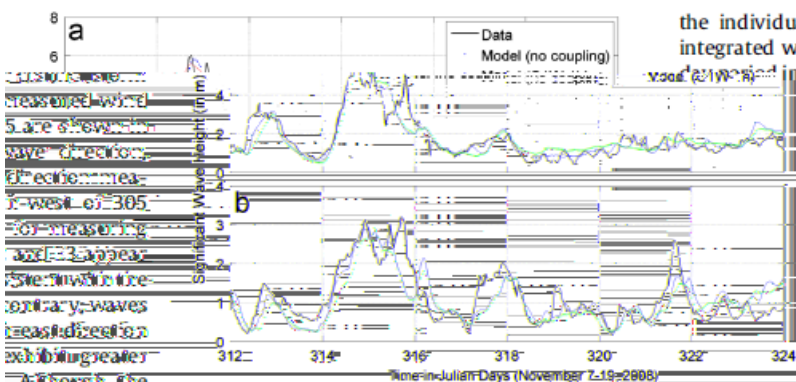
Fig. 6. Sample SWH comparisons at (a) B05 and (b) B06.

the individual component models affect the overall result. The integrated wind-wave–current model was implemented for a 12-

although there are some errors which may be due to inaccuracies in the winds and WOBCs. In addition, there may be some effect due to the water-level fluctuations and/or currents; the result obtained using CTW_T is also shown in Fig. 6 (red line), however this is discussed later in Section 5.2.

5. Results: Application of coupled wind-wave–current modeling

Overall, the validation studies described above inspire confidence in the individual component models. We now examine the performance of the integrated system determined by actual the currents on the waves, and attempt to ascertain how errors in

5.1. Choice of coupling methods

Our first task is to qualitatively explore the results and modeling efficiency when different coupling methods are used. A snapshot of the modeled wind and wave conditions (with no currents) during is for the CCI region. The winds and waves during
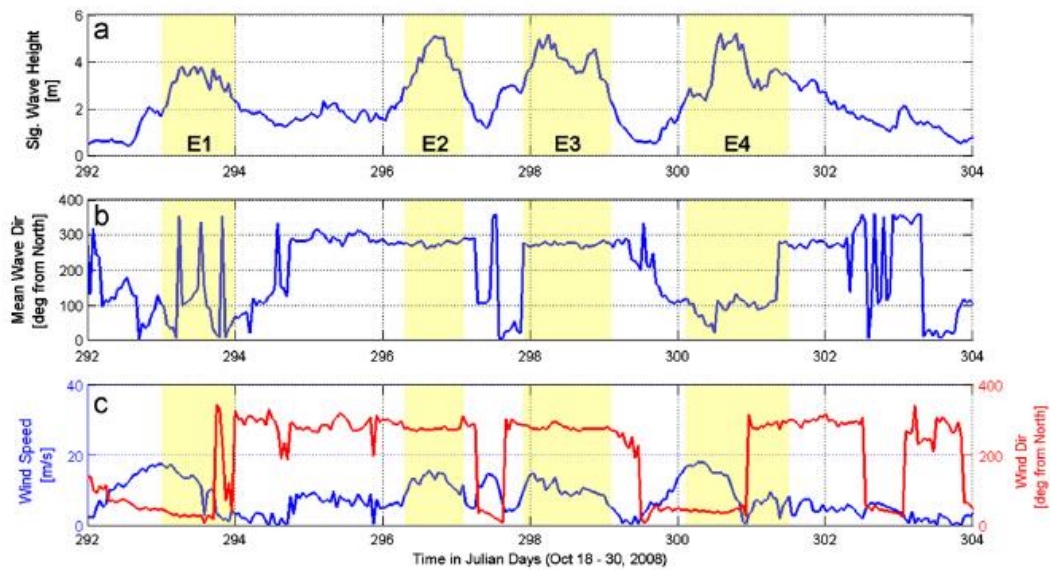
Fig. 7. (a) SWH (in m) and (b) mean wave direction (degrees from north, clockwise) measured at B05, (c) wind speed (in m/s, blue line) and direction (degrees, red line) measured at AUGA2.
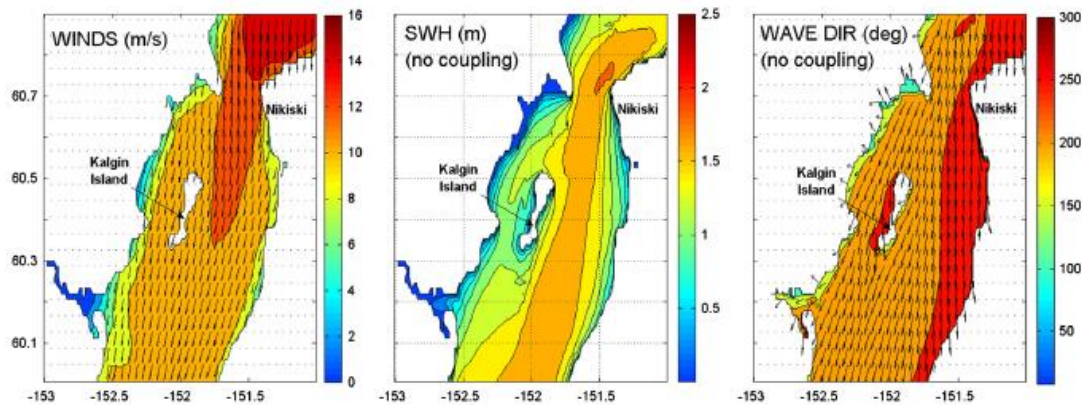

Fig. 8. Modeled wind speed (color) and direction arrows (left panel), SWHs (central panel), and mean wave direction (right panel) in the CCI on 27 October 2008 at 1 AM UTC (i.e. Julian day 301.0417).

mostly southward with wind speeds ~12–14 m/s and the modeled SWH ~1.5–2 m.

For wave–current interaction, the two coupling methods (i.e. C1W and C2W) were implemented using 1 h and 3 h updating intervals. Fig. 9 shows a combined plot of wave and current conditions, outputted from the SWAN model, on day 301.0417 (same time as Fig. 8). For C1W-1 h, the flow-field (which is largely tidal) was inputted to the wave model every hour; this yields a resolution of about 12 points per tidal cycle which may be considered to be reasonably accurate. In this case, the current direction is northward (opposite to the wind/wave direction) with a maximum speed of about 1.3 m/s near the Forelands, whereas to the south of Kalgin Island, currents are directed southward (same as the wind/wave direction) with speeds about 1 m/s (Fig. 9a). The opposite current directions are indicative of tide reversal during this time instant. The result in C1W-3 h (Fig. 9b), with an updating resolution of about 4 points per tidal cycle, is fairly similar to Fig. 9a but the peak velocities near the Forelands are different by ~0.3 m/s, since the flow-field at this instant (i.e. day 301.0417) is obtained by interpolation between days 301 and

301.125 (3-h period). The C2W simulations contain more physics (owing to the effect of the waves being accounted for in the currents) and are hence more time-intensive relative to the C1W simulations. In C2W-1 h (Fig. 9c), the flow-fields were updated on day 301.0417 and are mostly similar to those shown in C1W-1 h. However, in the case of C2W-3 h (Fig. 9d), the updating interval has a much greater effect because the flow-field taken from the previous updating time instant (i.e. on day 301) is assumed to be constant for the next 3 h (i.e. day 301.125) in the wave model. As a result, C2W simulations (Fig. 9d) show current-fields from the previous updating time instant (i.e. day 301), which are propagating northward in the entire domain, and are larger in magnitude (compared to those shown in C1W and C2W-1 h simulations) with maximum speeds of about 2 m/s (indicative of a flooding tide). Looking at the overall results, it would appear that the C2W-3 h diverges from the other solutions; the similarity of C2W-1 h with C1W simulations would suggest that the effect of waves on the flow-fields is marginal.

Compared to the SWHs obtained without any coupling (Fig. 8), the SWHs obtained using C1W simulations (Fig. 9e and f) are
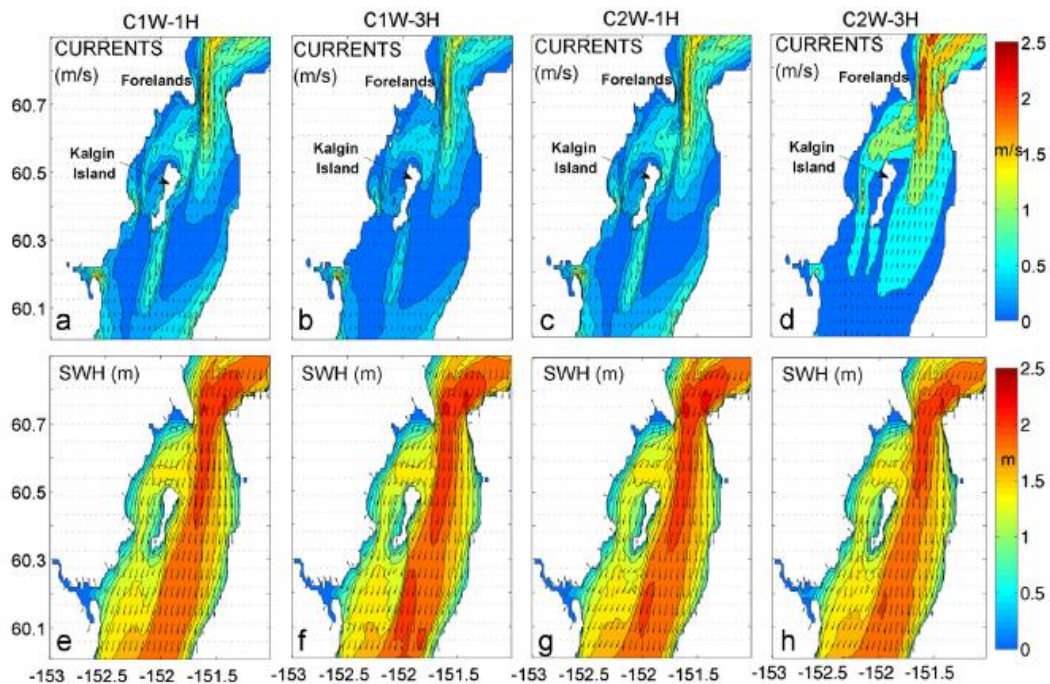
Fig. 9. Comparison of coupled model results of currents (top panels) and SWHs (bottom panels) in CCI using C1W and C2W approaches during the same time as Fig. 8. Panels (a)–(d) show currents outputted from C1W-1H, C1W-3H, C2W-1H, and C2W-3H simulations, respectively, whereas panels (e)–(h) show SWHs outputted from C1W-1H, C1W-3H, C2W-1H, and C2W-3H simulations, respectively. Arrows in top and bottom panels indicate current and wave direction, respectively.
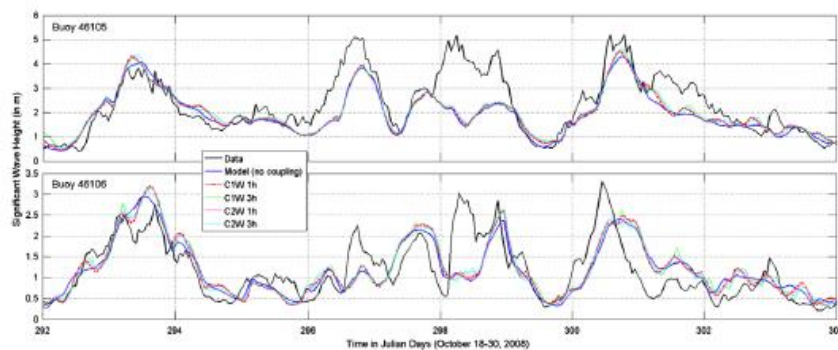
Fig. 10. Model comparisons of SWHs with and without coupling with data at B05 (top) and B06 (bottom).

about 0.3–0.4 m higher near the Forelands due to the effect from the opposing current. South of Kalgin Island, however, the SWHs increase by about 0.2 m with C1W-1 h (Fig. 9e), and by about 0.3 m with C1W-3 h (Fig. 9f). These differences in the SWHs with C1W simulations (Fig. 9e and f) are related to 1 h vs. 3 h interpolation of flow-fields in the wave model. SWHs obtained using C2W simulations (Fig. 9g and h), on the other hand, seem to be about 0.1–0.2 m higher than C1W, and about 0.5 m higher compared to no coupling. As explained above, these differences are due to the differences in current-fields between C1W and C2W simulations. In general, these results, which are qualitatively consistent with our expectations given the directions of the waves and currents, inspire confidence in the used modeling scheme.

Overall, the differences in the SWHs (~0.5 m) with and without coupling clearly indicate that some level of coupling (one-way or two-way) is necessary in the CI region. Since the effect of

waves on currents was found to be marginal, the C2W approach may not be warranted. Also, as discussed above, a smaller updating time step may be required (1 h or less) to better resolve the tidal fluctuations. With regard to the efficiency of the system, it was found that the C1W approach is more efficient compared to the C2W approach (a 2-day simulation using C1W with a 1 h exchange interval took about 2 h, whereas with C2W the same simulation took about 3 h).

5.2. Quantitative model performance evaluation

The model performance was then evaluated with and without coupling against data from B05 and B06 (Fig. 10) situated in the LCI. While the above discussion dealt with only one event, here data from all 12 days are used. There are rather small differences between the results of all model simulations (i.e. no coupling, C1W-1 h, C1W-3 h, C2W-1 h, and C2W-3 h), and overall they

65

follow a similar trend at both the locations. For smaller SWHs (<2 m), however, the coupled model results show some oscillations with a period of approximately half a day, especially between days 302 and 304, which are not seen in the results obtained without coupling (blue line; Fig. 10). These patterns can also be seen in Fig. 6a (red line, between days 318 and 322). Although the data undulations shown in Fig. 6a (black line, between days 318 and 322) are not exactly reproduced by the C1W-1 h simulation, these results indicate that, for smaller SWHs (<2 m), the coupling does modify the SWHs due to fluctuating tidal currents. Overall, from these results and the discussion in Section 5.1 above, it may be concluded that C1W-1 h is sufficient for coupling SWAN and EFDC in CI.

As regards the coupled model performance for the four events shown in Fig. 10, only event E1 was predicted with better accuracy compared to the other events (E2, E3, E4 were under-predicted roughly by 20%, 40%, and 15% respectively). These large errors demand further investigation of other factors (winds, wave boundary conditions etc.) in order to identify the cause of such errors.

5.3. Effect of individual errors in the integrated system

The SWH errors discussed above could have resulted from errors in any of the individual components of the overall system (such as winds, currents, WOBCs). In the following, the effect of these errors is discussed in detail only for B05.

5.3.1. Effect of errors in WOBCs

The accuracy of the WOBCs could dictate the accuracy of the wave conditions at locations in the interior of the model domain. The LCI is often dominated by swells coming from Gulf of Alaska through Stevenson Passage and Kennedy Entrance towards the east, and Shelikof Strait towards the west (Fig. 1). The spectral output of WW3 model forms the basis for the WOBCs of the CI wave model. As discussed earlier in Section 4.3, spectra at B78 and B80 were used as forcing functions along the open boundaries. It is thus obvious that one must check the quality of WW3 output at B78 and B80. It can be clearly seen that the four storm events are under-estimated by WW3 (black dashed line in Fig. 11a and b). For instance, during E4, the measured SWH at B80 exceeded 8 m (Fig. 11b), whereas the WW3 prediction was about 5.5 m (~30% underestimation). This implies that these errors on the boundaries could be responsible for some of the error (or the entire error) at B05. One way to confirm this hypothesis is to force the model through buoy-measured wave spectra on the open boundaries. Unfortunately, B78 and B80 only measure the 1D wave energy spectrum and do not contain any directional information. Thus, the buoy-measured spectra were used along with the WW3 output of peak wave direction (assuming it was accurate) and the spreading function of Mitsuyasu et al. (1975) to construct a 2D wave energy spectrum (the chosen spreading function may not be suitable for unidirectional swell conditions, and hence introduces additional uncertainty). The resulting 2D wave spectra were then imposed along the open boundaries.

Wave model results at the locations of B78, B80, and B05 using the buoy-imposed spectra are also shown in Fig. 11 (red dotted line). The model output closely matched the buoy measurements at the locations of B78 and B80 (Fig. 11a and b). At the location of B05 (Fig. 11c), only E1 and E4 seemed to be affected by the change in WOBCs. Since the wave direction is predominantly from the eastern Gulf of Alaska, this implies, to some extent, that the large seas associated with E1 and E4 are representative of the seas that occurred at B80 (located on the eastern boundary of the model domain). However, this does not apply to other events (E2 and E3) since those are still under-estimated by the model. This possibly suggests that the waves measured at B05 during events E2 and E3 may not have originated in Gulf of Alaska; rather they may be a result of some other physical phenomenon (e.g. local winds).

Comparisons at the location of Buoy 46077 (B77) are also shown to check the validity of using wave conditions at B78 on the entire west-boundary. B77 is located in Shelikof Strait (Fig. 1) and experiences swells coming from the south-west direction (apart from locally generated wind-seas). As can be seen from Fig. 12 (black dashed line), the model results do not fare well throughout the period of the simulation. This indicates that the assumption of wave conditions from B78 is incorrect along the western open boundary. Unfortunately, there are no nearby
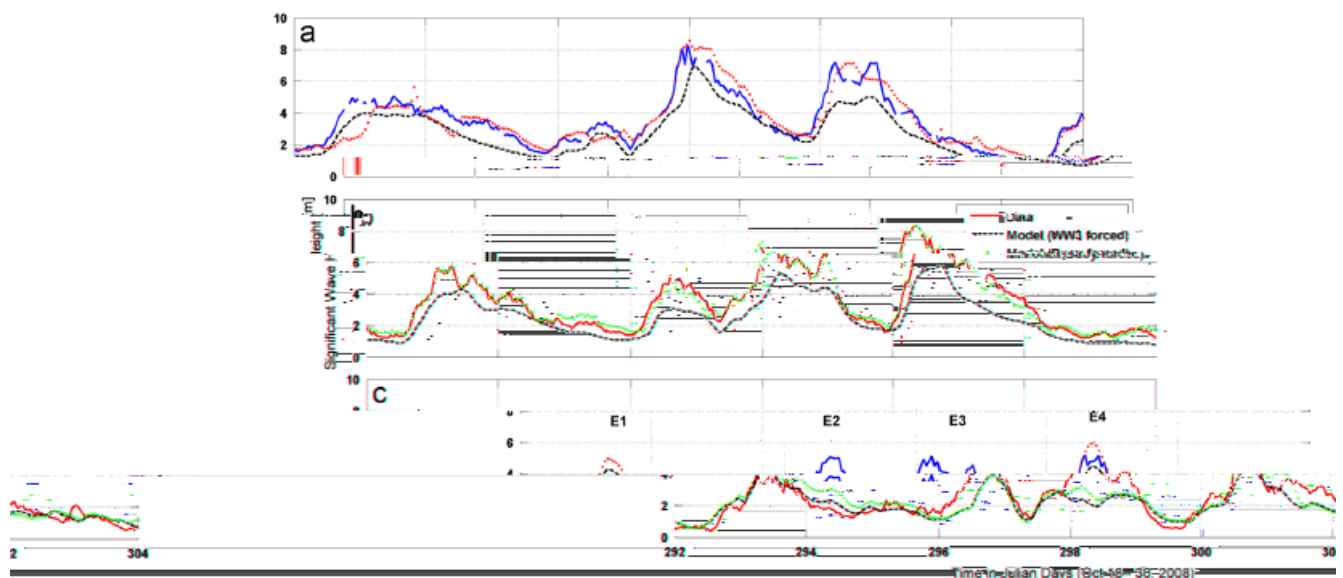
, (b) B80, and (c) B05.   Fig. 11. SWH comparisons using WW3 and buoy-forced wave spectra on boundaries at (a) B78
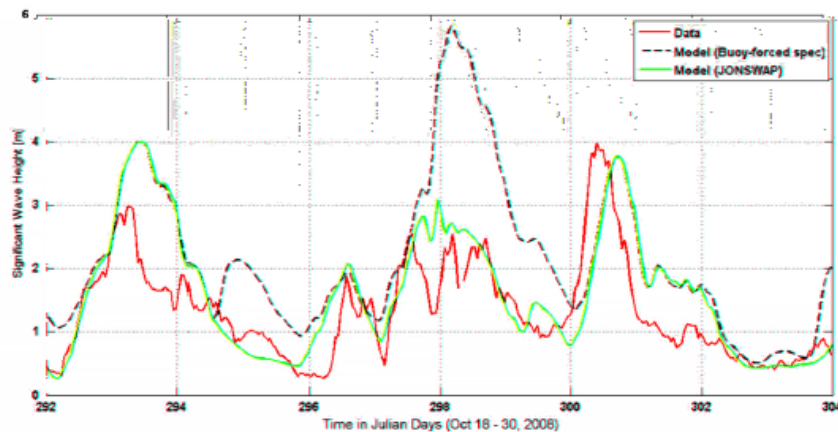
Fig. 12. SWH comparisons at B77 using buoy and JONSWAP spectra on the western open boundary.

points along the western boundary from where full spectral information could be extracted. Thus, we have resorted to using an approximate approach, outlined in Singhal et al. (2010), for generating the 2D wave spectra along the western boundary. In particular, WW3 provides output of SWH, peak wave period, and peak wave direction on a 7 km grid for northern Gulf of Alaska. Using these quantities, one can utilize the JONSWAP spectrum along with a suitable directional spreading function to create a 2D energy spectrum (see Singhal et al. (2010) for specific details). Fig. 12 also shows the effect of using the approximate approach on SWHs at the location of B77 (red line). It can be seen that the large errors around day 298 have reduced significantly. This allows us to conclude that the approximate approach of using JONSWAP spectrum, while not without problems, appears superior to assuming the wave conditions from B78 along the western boundary. For the remainder of the discussion that follows, the open boundaries are forced by approximated 2D JONSWAP spectrum on the western boundary and the full spectral output at the locations of B78 and B80 along the southern and the eastern boundary, respectively.

5.3.2. Effect of errors in winds

Turning to the errors in the input winds, based on the previous discussion, events E2 and E3 do not seem to be affected by the errors present in the WOBCs. The quality of WRF winds was checked specifically during E2 and E3. As noted earlier, B05 is not equipped with an anemometer, and thus WRF winds were compared at the locations of three weather stations – Augustine Island (AUGA2), Flat Island (FILA2), and Amatuli Island (AMAA2) – that form a triangle around B05 (Fig. 1). The winds were predominantly from the west during the two events (Fig. 13 right column). This trend is typical during the month of October when the winds originate from Iliamna Lake in the west (Liu et al. 2006). Fig. 13 indicates that the WRF model under-predicted the wind speeds at AUGA2 and FILA2. The under-prediction, on average, was by a factor of about 1.25 for E2, and about 1.75 for E3. This under-prediction in the wind speeds seems to be in line with the corresponding under-prediction in the modeled SWHs at B05. The winds at AMAA2, on the contrary, were consistently over-predicted by WRF (this trend was found during other times as well). A full assessment of WRF model for CI is, however, beyond the scope of this work, and attention is rather directed towards finding solutions in order to improve the corresponding wave estimates.

In this case, a straightforward remedy is to modify the wind speeds using the average under-prediction ratio during events E2 and E3. The WRF wind speeds were thus adjusted by a factor of 1.25 spatially over a small region near B05 (somewhat subjectively determined) for E2 (that lasted about a day); a factor of 1.75 was used over the same region for E3 (also lasted about a day). The results, shown in Fig. 14, clearly indicate that the adjustment significantly improves the SWH estimates during E2 and E3 (even though some errors still remain).

Although the above discussion shows that improving the winds for specific events may improve the SWHs, the obvious question, viz. "how does the wave forecaster know there is a problem with the winds?", still remains unanswered. The randomness of the wind-fields renders the creation of simple correction factors for general use impossible. Other solutions, such as the improvement of the WRF model physics, better resolved topographical features, and/or data assimilation, must thus be explored.

5.3.3. Effect of errors in currents

While the velocity fields calculated in Section 4.2 were fairly accurate, it is possible that random errors in the wind-fields used to force the circulation model or (possibly seasonal) baroclinic effects, not considered here, could induce errors in a forecasting scheme. A sensitivity analysis was therefore performed by adding a random error ϵ to the modeled flow velocities, where ϵ is a uniformly distributed random number such that, $-0.1*velocity \le \epsilon \le 0.1*velocity$. The SWH results obtained using the updated velocities were compared to the results without the added error at various locations throughout the CI. It was found that, for the most part, the maximum differences between the SWHs were of the order of ± 10 cm. These small differences are negligible in the context of the surface wave heights applications, and suggests that the velocities obtained from the EFDC simulations are adequate for the task at hand.

6. Conclusions

1. It is found that the depth-averaged EFDC model provided reliable predictions of water-levels and circulation patterns in CI. The water levels were predicted with high accuracy at Kodiak, Seldovia, and Nikiski ($R^2 > 0.98$); near Anchorage a finer grid was required to obtain a good match with data and, in particular, to properly predict the tidal phases.
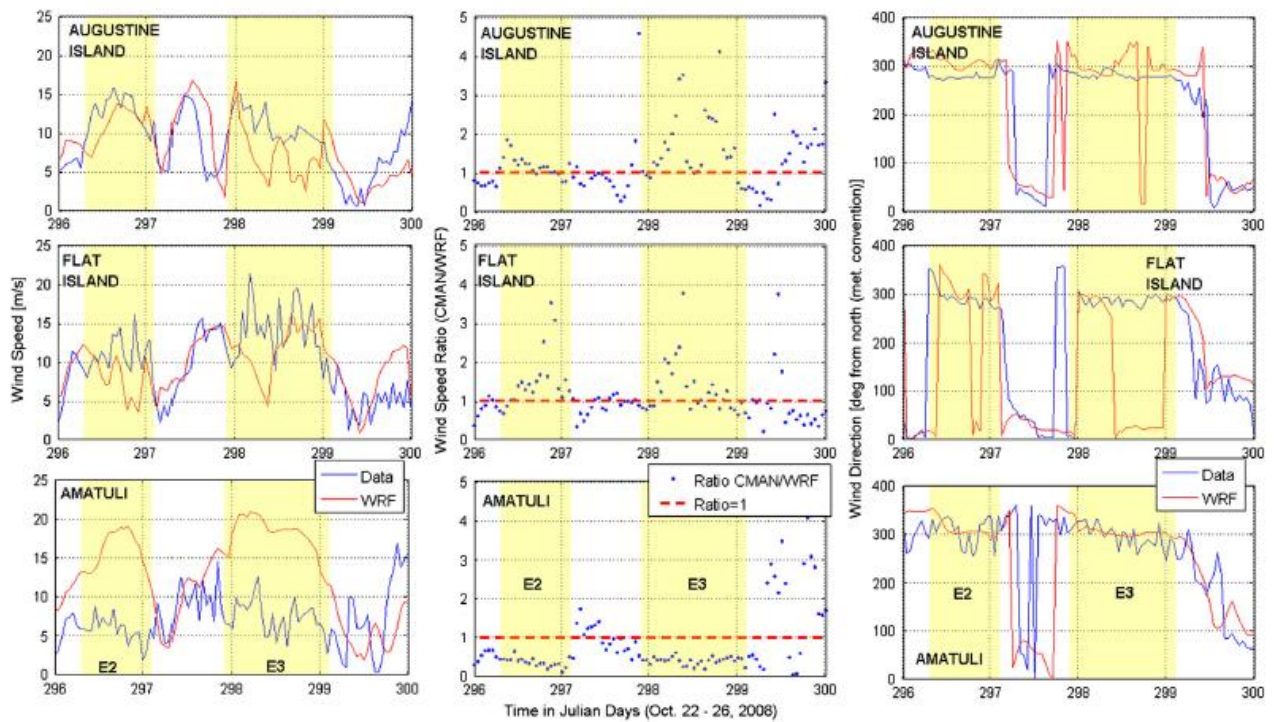
Fig. 13. WRF model comparisons at three weather stations for wind speed (left column), ratio of observed vs. WRF (central column), and wind direction (right column).
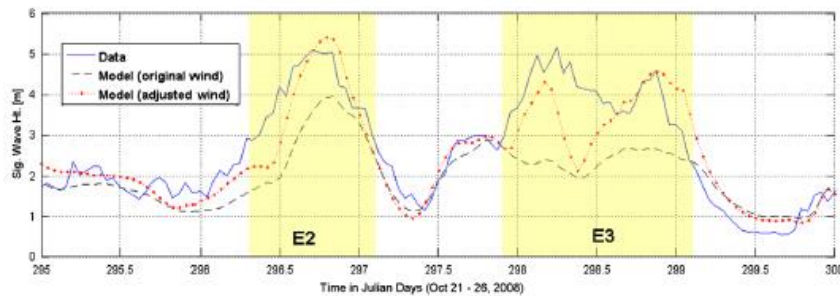

Fig. 14. Sensitivity of SWHs to enhancement of wind speeds during E2 and E3 at B05.

The depth-averaged flow velocities were also predicted with high accuracy ($m > 0.74$, $R^2 > 0.86$) throughout the CI, thereby suggesting that the 2D model is sufficient and accounting for additional physics may not be warranted for forecasting purposes.

2. Coupling of SWAN and EFDC was performed in the one-way (C1W) and two-way (C2W) modes using a 12-day period dominated by four storm events. It was found that the differences in SWH results obtained using C1W and C2W were due to the rapidly changing tidal conditions, the effects of which are not updated frequently in C2W because of the assumption of steady conditions in the time between the information exchanges. This can be corrected by using a much smaller information exchange time step; however, the computations would be too time consuming for forecasting purpose. Sensitivity studies using 1 h and 3 h updating intervals also showed qualitative differences in the SWHs, and to fully capture the rapid tidal fluctuations, a smaller updating interval (1 h or less) may be needed. Not only is C1W more efficient than C2W, the C2W approach may not be necessary because

the effect of the waves on the currents was found to be marginal at the spatial scales ($\sim$1.5 km) investigated.

3. As to the wave–current interaction, at the locations where data were available (i.e. in LCI), for SWHs > 2 m, no discernible differences were found in the modeled SWHs with and without the currents. For the smaller SWHs (SWH < 2 m), some effect, including fluctuations corresponding approximately to the tidal period, were seen in the coupled model results. Qualitative results show that the shallow northern CI (near Kalgin Island and the Forelands) – where the "background" SWHs were found to be about 1.5–2 m during the study period – experienced a change of $\sim$0.5 m.

4. For those periods when the wind-fields were reliable, the SWH predictions reasonably matched the data (e.g. day 315 in Fig. 6, event E1 in Fig. 10). Other times, the errors in modeled SWHs were found to be largely due to the errors in the winds and the WOBCs (e.g. events E2, E3, and E4 in Fig. 10), and less due to errors in the modeled hydrodynamic fields. It was shown that an (artificial) improvement in the wind-fields and WOBCs reduced the errors in the wave predictions. However, it was

68

found that the errors in winds were random and thus could not be easily remedied for future forecasts. As to the WOBCs, the SWHs at B05 were sometimes found to be sensitive to the wave conditions at B80 (e.g. during E1 and E4). Sensitivity studies involving artificial adjustment to the currents (to account for possible baroclinic effects, errors in wind-fields, and other effects) had only a marginal difference on the SWHs (<10 cm on average). To eliminate errors of the sort seen in Fig. 10, improved wind-fields and more detailed specification of wave spectra on the open boundaries are needed.

Acknowledgments

References

Allard, R.A., Dykes, J.D., Hsu, Y.L., Kaihatu, J.M., Conley, D., 2008. A real-time nearshore wave and current prediction system. Journal of Marine Systems 69, 37–58.

Booij, N., Ris, R.C., Holthuijsen, L.H., 1999. A third-generation wave model for coastal region: 1. Model description and validation. Journal of Geophysical Research 104 (C4), 7649–7666.

Chen, Q., Wang, L., Zhao, H., Douglass, S.L., 2007. Prediction of storm surges and wind waves on coastal highways in hurricane-prone areas. Journal of Coastal Research 23 (5), 1304–1317.

Egbert, G.D., Erofeeva, S.Y., 2002. Efficient inverse modeling of barotropic ocean tides. Journal of Atmospheric and Oceanic Technology 19 (2), 183–204.

Funakoshi, Y., Hagen, S.C., Bacopoulos, P., 2008. Coupling of hydrodynamic and wave models: case study for Hurricane Floyd (1999) hindcast. Journal of Waterway, Port, Coastal and Ocean Engineering, 321–335.

Hamrick, J.M., 1992. A Three-dimensional Environment Fluid Dynamics Computer Code: Theoretical and Computational Aspects. Special Report 317. The College of William and Mary, Virgina Institute of Marine Science, Williamsburg, Virgina, 63 pp.

Ji, Z.-G., Morton, M.R., Hamrick, J.M., 2001. Wetting and drying simulations of estuarine processes. Estuarine, Coastal, and Shelf Science 53, 683–700.

Jin, K.-R., Hamrick, J.H., Tisdale, T., 2001. Application of a three-dimensional hydrodynamic model for Lake Okeechobee. Journal of Hydraulic Engineering 126, 758–771.

Johnson, M., 2008. Water and Ice Dynamics in Cook Inlet. Final Report, OCS Study MMS 2008-061. Mineral Management Service, p. 106.

Kuo, A.Y., Shen, J., Hamrick, J.M., 1996. The effect of acceleration on bottom shear stress in tidal estuaries. Journal of Waterway, Port, Coastal, and Ocean Engineering 122, 75–83.

Liu, H., Olsson, P.Q., Volz, K.P., Yi, H., 2006. A climatology of mesoscale model simulated low- level wind jets over Cook Inlet and Shelikof Strait, Alaska. Estuarine, Coastal and Shelf Science 70, 551–566.

Longuet-Higgins, M.S., Stewart, R.W., 1964. Radiation stress in water waves; a physical discussion, with applications. Deep-Sea Research 11, 529–562.

Mistuyasu, H., Tasai, F., Subara, T., Mizuno, S., Ohkusu, M., Honda, T., Rikiishi, K., 1975. Observations of the directional spectrum of ocean waves using a clover-leaf buoy. Journal of Physical Oceanography 5, 750–760.

Oey, L.-Y., Ezer, T., Hu, C., Muller-Karger, F.E., 2007. Baroclinic tidal flows and inundation processes in Cook Inlet, Alaska: numerical modeling and satellite observations. Ocean Dynamics 57, 205–221.

Olsson, P.Q., Volz, K.P. Forecasting near-surface weather conditions and precipitation in Alaska's Prince William Sound with the PWS-WRF modeling system. Continental Shelf Research, doi:10.1016/j.csr.2011.12.012, this issue.

Okkonen, S.R., Howell, S.S., 2003. Measurements of Temperature, Salinity, and Circulation in Cook Inlet, Alaska. Final Report, OCS Study MMS 2003-036. Mineral Management Service, 28.

Plant, N.G., Edwards, K.L., Kaihatu, J.M., Veeramony, J., Hsu, L., Holland, K.T., 2009. The effect of bathymetric filtering on nearshore process model results. Coastal Engineering 56, 484–493.

Ris, R.C., Booij, N., Holthuijsen, L.H., 1999. A third-generation wave model for coastal regions: part II verification. Journal of Geophysical Research 104 (C4), 7667–7681.

Shen, J., Boon, J., Kuo, A.Y., 1999. A numerical study of a tidal intrusion front and its impact on larval dispersion in the James River estuary. Estuary 22, 681–692.

Singhal, G., Panchang, V.G., Lillibridge, J.L., 2010. Reliability assessment for operational wave forecasting system in Prince William Sound, Alaska. Journal of Waterway, Port, Coastal, and Ocean Engineering 136 (6), 337–349.

Smith, O., Khokhlov, A., Zieserl, M., 2005. Water Property, Sediment, Tide, and Current Measurements and Analyses in the Vicinity of the Proposed Knik Arm Bridge. Contract Report for URS and HDR, sponsored by Knik Arm Bridge and Toll Authority.

Smith, S.J., Peterson, M.D., Pratt, T.C., 2010. Numerical modeling studies supporting port of Anchorage deepening and expansion; Part II: measuring physical processes. In: Proceedings of the Estuarine and Coastal Modeling Conference (ECM 11), Seattle, WA, pp. 286–300.

Stabeno, P.J., Bond, N.A., Hermann, A.J., Kachel, N.B., Mordy, C.W., Overland, J.E., 2004. Meteorology and oceanography of the northern Gulf of Alaska. Continental Shelf Research 24, 859–897.

Tolman, H.L., 2009. User Manual and System Documentation of WAVEWATCH III Version 3.14. NOAA/NWS/ NCEP/MMAB Technical Note 276, 194 pp.+Appendices.

Reliability and Efficiency of a Coupled Wind-Wave-Current Forecasting System for Cook Inlet, Alaska.

From Solution to Coastal Disasters 2011

RELIABILITY AND EFFICIENCY OF A COUPLED WIND-WAVE-CURRENT FORECASTING SYSTEM FOR COOK INLET, ALASKA

Gaurav Singhal[1], Vijay Panchang[2], Juan Horrillo[3], Chan Kwon Jeong[4]

1. Texas A&M University at Galveston, 200 Seawolf Parkway, Galveston, TX 77553, USA. singhalg@tamug.edu
2. Texas A&M University at Galveston, 200 Seawolf Parkway, Galveston, TX 77553, USA. panchanv@tamug.edu
3. Texas A&M University at Galveston, 200 Seawolf Parkway, Galveston TX 77553, USA. horrilloj@tamug.edu
4. Texas A&M University at Galveston, 200 Seawolf Parkway, Galveston, TX 77553, USA. chankwon@tamu.edu

Abstract: Knowledge of ocean weather conditions is important for mariners, offshore oil and gas operations, evacuation procedures, and sustainable management of coastal resources. While NOAA provides forecasts of ocean weather for outer oceans, these forecasts do not cover near-shore areas which present their own challenges such as complex coastal morphology, more complex wave dynamics, etc. To supplement NOAA's efforts, we describe the development of a coupled wind-wave-current forecasting system for Cook Inlet (CI), Alaska. The system utilizes two-way coupling to incorporate the effects of wave-current interaction in the forecasting scheme. Results indicate that the inclusion of surface-currents greatly affects the wave dynamics in the northern CI. During flood currents, the modeled wave heights are found to increase by as much as 50% compared to those without the effect of currents. However, preliminary findings suggest that the effect of wave model on the circulation model is marginal.

INTRODUCTION

Ocean weather forecasts (of winds, waves, currents, etc.) are critical for safety of maritime operations, evacuation of coastal communities during hurricanes/storms, planning and management of coastal resources, and also predicting the extent of contaminant transport (e.g. oil spills, waste water, etc.). It is thus necessary to provide

109

70

the most reliable forecast information in order to support these operations in a timely and effective manner.

NOAA's National Centers for Environmental Prediction (NCEP) branch has been undertaking such efforts for global oceans for quite a few years. For the continental US, NCEP also uses a nested grid system to provide forecasts on better-resolved scales (~15 km and ~7 km resolution). Their efforts have propelled other federal agencies to provide forecasts at an even higher resolution. For example, US Navy's Naval Research Laboratory provides coupled forecasts of surface waves and currents for Mississippi Bight and Southern California Bight at a resolution of about a km (http://www7320.nrlssc.navy.mil/CenGOOS/). Other local entities, such as Gulf of Maine Ocean Observing System and Alaska Ocean Observing System (AOOS), have also recently started providing forecast information, aided by observational experiments, to support a variety of operations (e.g. AOOS organized a field experiment in July 2009 to observe and validate various models in Prince William Sound; Schoch and Chao 2010).
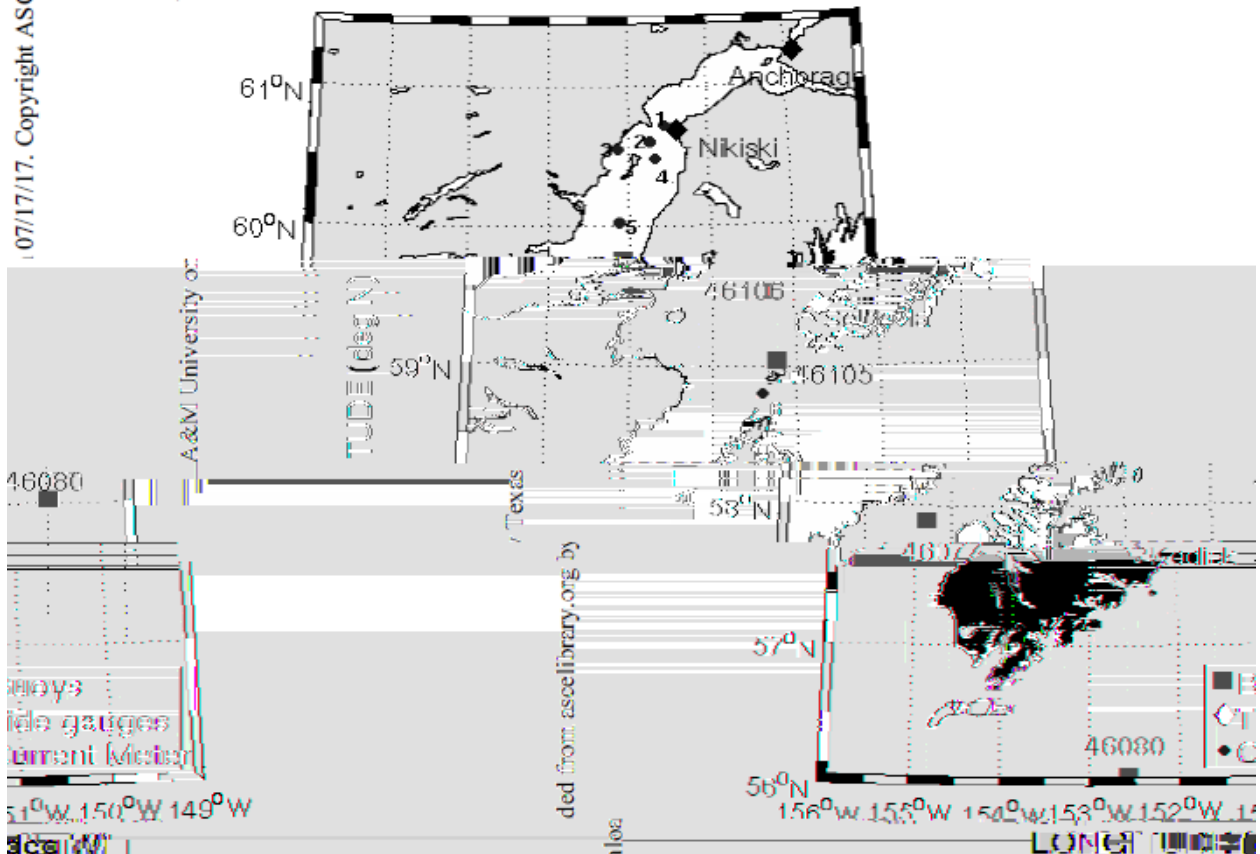

Figure 1. Cook Inlet model domain. Squares, diamonds, and circles represent buoy, tidal gauge, and current meter locations respectively. Current meter locations are Forelands (1), South of West Forelands (2), Drift River (3), East of Kalgin Island (4), Cape Ninilchik (5), and Stevenson Passage (6).

This study attempts to address the needs associated with safety of marine operations, environmental protection, and sustainable management of coastal resources in Cook Inlet (CI), Alaska (Fig. 1). CI is a large estuary (~ 180 miles long), stretching from the Gulf of Alaska to Anchorage in south-central Alaska. CI has a great deal of human activity, including high levels of resource extraction (oil and gas, timber, minerals, etc). Approximately half of Alaska's population lives along CI's shores. Anchorage, on Knik Arm at the head of CI, is Alaska's largest city and a center of transportation, commerce, industry, and tourism. The Port of Anchorage receives food, fuel, building materials, durable and expendable supplies of all kinds for delivery to over 80% of Alaska's population and to four large military installations. Shipping routes in CI serve the port year-round, as well as the ports of Nikiski, Homer, and Drift River with transshipment to smaller coastal communities. Other marine traffic is related to the recreation and tourism industries, as well as commercial fishing for halibut and salmon, on which the coastal communities of the Kenai Peninsula depend. Homer Harbor is one of the largest boat harbors in the State and is full to capacity with commercial and charter fishing, excursion, government agency, and private recreation boats. The majority of citizens living in the south-central Alaska rely on the marine environment to some extent for subsistence, recreation, or commercial uses. Offshore oil and gas operations require wave information for design and evacuation purposes.

CI is also an extremely dynamic system. A cursory examination of the brief dataset available from Buoy 46077 suggests that significant wave heights (SWH's) can be as large as 4.5 m (corresponding to "maximum" wave conditions of about 25 ft in that sea-state). There are large tidal variations (about 25 ft, second only to Bay of Fundy) and the bathymetry and coastal morphology are complex. There is significant wave/current action and during low tides, silty bottoms (mudflats) are exposed which further make marine navigation difficult. In addition, the underlying complex terrain impacts wind direction and speed. Also important is the impact of the strong tidal flows through Lower CI into and out of the Gulf of Alaska. Mariners piloting vessels in the region attest to the impact of the interaction of these forces on maritime operations.

As stated earlier, wave predictions for the Gulf of Alaska region are in fact produced by NOAA/NCEP, but as part of a large-scale simulation for the entire Pacific. In the last few years, NCEP has extended the forecasts into CI at an approximately 7-km resolution to produce first-order estimates of the wave conditions. We refer to them as first-order estimates because: (a) the resolution will need refinement in many areas for properly representing the intricacies of this domain that encompasses tens of miles of coastline with complicated bathymetric and geometric variations; (b) the predictions at present do not account for the extreme water level changes caused by the tides (tidal ranges in CI are high, varying from 6 m at Seldovia to 9.5 m at Anchorage); (c) the predictions do not include tidal and other currents, which in some cases can exceed 4 knots (opposing currents increase the wave height, etc.); (d) the predictions do not rely on a "local" wind model that incorporates the complexities induced by underlying topography (Liu et al. 2006); and (e) tidal and other fluctuations lead to alternate flooding and drying of many areas, which are not at present part of the NCEP forecast.

Clearly, these effects must be incorporated into NCEP's forecasts to provide the most accurate information. The main focus of this study is thus geared towards incorporating such higher order effects by way of a "coupled" approach. In particular, this study focuses on implementing a coupled forecasting system for CI through dynamic interlinking of atmospheric (wind) and oceanic (wave and circulation) models in order to produce the most efficient, yet reliable, ocean forecast. The paper is organized as follows. The following section describes the modeling methodology and validation studies for the wave and the circulation model. Then, the procedure for coupled wave-current modeling is described, followed by summary and concluding remarks.

MODELING METHODOLOGY AND HINDCAST STUDIES

This section describes the basic modeling methodology for CI forecasting system. Our efforts have been geared mainly towards establishing a base wave model and a base circulation model that is capable of simulating barotropic (effect of tides and winds) circulation within the CI. This involved experimentation with various bathymetric data (e.g. Etopo, coastal relief model etc.), model grids and grid resolutions, choice of boundary conditions, bottom friction coefficients etc. Initially, both the wave model and the circulation model were tested for accuracy without any inter-model interaction. Only after that, the two models were allowed to exchange information. In the following, we discuss the development and validation of the two models separately.

Basic Wave Modeling

For wave modeling, the SWAN ("Simulating WAves Nearshore") model was utilized. The details of the SWAN model have been described in numerous studies (e.g. Booij et al. 1999; Ris et al. 1999; Rogers et al. 2007; Funakoshi et al. 2008) and thus we have not included those here for brevity. In this study, a basic wave model for the general area of CI was established. The wave model domain covered the region between -156° W to -149° W, and 56° N to 61.5° N (Fig.1) at a resolution of about 1 km. The wave model was forced by high-resolution winds from Weather Research and Forecasting (WRF) model (WRF model output is provided by University of Alaska, Fairbanks). The boundary conditions on the open ocean boundaries were obtained using the multi-grid version of WAVEWATCH III^{TM} (WW III; Tolman 2009) model for the Alaskan region. In particular, the full spectral output of the WW III model at the locations of NDBC buoys 46078 and 46080 were forced on the south and east boundaries, respectively.

Sample wave model comparisons of SWHs with buoy data are shown in Fig. 2 (for specific details regarding wave modeling, please see Singhal et al. (2010) where the wave forecasting system was developed and verified for Prince William Sound, Alaska).

Basic Circulation Modeling

In this paper, only the most successful efforts towards development of CI circulation model are described. To that end, EPA's Environmental Fluid Dynamics Code (EFDC) was used. The EFDC model was developed at the Virginia Institute of Marine Science (Hamrick, 1992). The model solves the three-dimensional, vertically hydrostatic, free surface, turbulent averaged equations of motions for a variable density fluid. EFDC has been tested and verified in a wide range of hydrodynamic and environmental studies

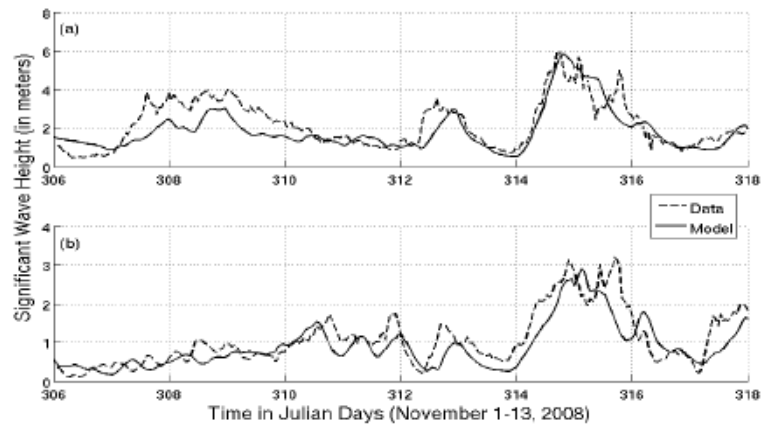(e.g. Kuo et al. 1996; Shen et al. 1999; Ji et al. 2001; Jin et al. 2001).

Figure 2. SWH comparisons at locations of (a) Buoy 46105 and (b) Buoy 46106.

The EFDC model was applied to CI domain on an irregular grid with a resolution of about 4 km at the open ocean boundaries, decreasing to about a resolution of 1 km in the north-most parts of CI. Other model resolutions were also tested (e.g. <1 km), however the model simulation time increased drastically for higher resolutions without a major impact on the accuracy of the results. Since the goal is to develop a real-time forecasting system, some compromise regarding the model grid resolution would need to be made in order to make efficient, yet accurate, forecasts.
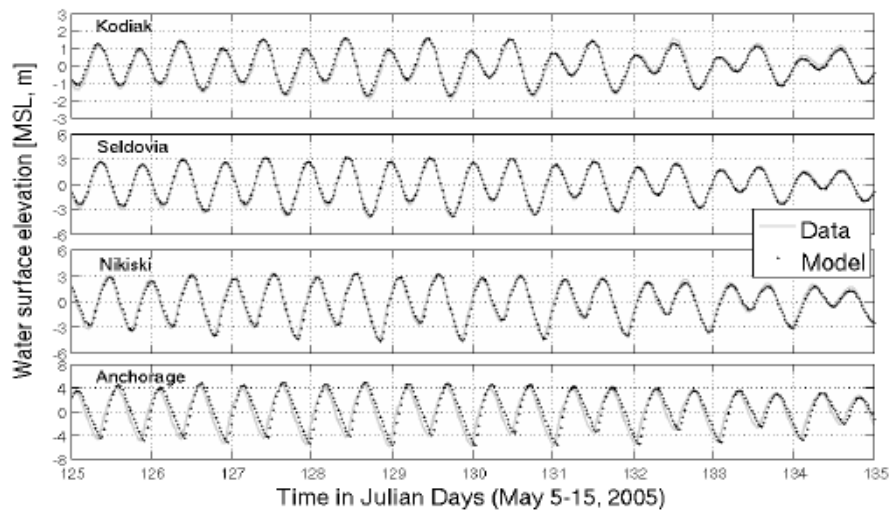

Figure 3. Water surface elevation (relative to MSL in m) comparisons. Solid line represents data and circles represent model results.

The CI circulation model was tested via simulation of tidal conditions for summer of 2005 (May-August). This period was selected mainly because it coincided with NOAA's comprehensive survey of current measurements within CI. Six locations were selected from this survey for model comparison (shown in Fig.1). The model was initiated from

motionless conditions on May 1, 2005 via prescription of sea surface heights provided at the open model domain boundaries (8 tidal waves were taken into account, namely: M2, S2, N2, K2, K1, O1, P1 and Q1). These boundary sea level elevations were extracted from TPXO6.2 global satellite-based tidal model (Egbert and Erofeeva, 2002). Winds from six land stations were also prescribed on the model grid (WRF wind data were not available during 2005). The model was verified with data from tidal gauges as well as current meters deployed at various locations.
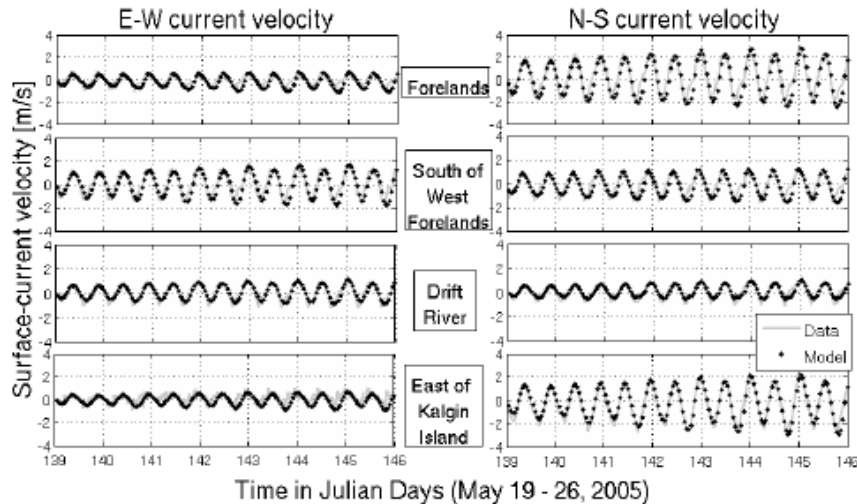

Figure 4. Surface-current velocity comparisons. Left panels show East-West (E-W) whereas right panels show North-South (N-S) velocities. Solid line represents data, and circles represent model results.
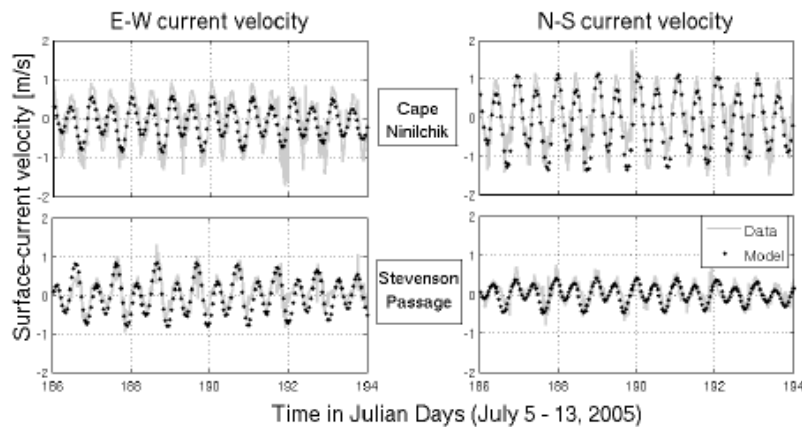
Figure 5. Same as Fig.4 but for different locations and different time period (current meters at these locations were deployed in July 2005)

It can be seen that the model captured significant variability of CI tidal circulation and calculated variability (Fig. 2). The simulated tidal elevations and tide-gauge stations for the tested period were in good agreement with tidal elevations calculated based on tidal constituents obtained from observations (Fig. 3). Comparison of modeled surface-current

velocities with the measurements at six locations throughout CI is also fairly reasonable (Figs.4, 5). Qualitatively, the model captured the semi-diurnal tidal fluctuations at all locations quite well.

COUPLED WAVE-CURRENT MODELING

After the two models were verified, the emphasis was directed towards coupling the two models to understand the effects of wave-current interaction. Generally speaking, changing water levels and currents modify the wave conditions (wave heights increase in opposing currents, etc.); wave-breaking, on the other hand, may alter the surface-current pattern to some extent. However, since the tidal regime in CI is quite strong it is expected that the wave-induced circulation may not play a significant role in affecting the overall circulation pattern within CI.

For coupling between a wave model and a circulation model, there are two possible options - 1) Off-line coupling, and 2) On-line coupling. In off-line coupling, there can be one-way or two-way coupling. In one-way coupling, the output from one model is transferred to the other model without any further exchange of information. For example, if a circulation model is executed first, then the water levels and currents are fed as input into the wave model, after which the simulation is stopped. In two-way coupling, one of the models is executed first, the output of which is transferred to the second model. Then the output from the second model is fed back into the first model, and the whole process is repeated. There are a few studies that have used both one-way and two-way coupling (in off-line mode) to address wave-current interaction. For example, Chen et al. (2005) performed a one-way coupling of SWAN and ADCIRC ("ADvanced CIRCulation") in Mobile Bay, whereas Funakoshi et al. (2008) performed two-way coupling of ADCIRC and SWAN for hindcasting Hurricane Floyd near northeast coast of Florida. On the other hand, on-line coupling invokes both models simultaneously. At a suitable time step, the two models exchange information and continue the simulation until the next communication time step. Warner et al. (2008) utilized the model-coupling toolkit to perform an on-line coupling of ROMS ("Regional Oceanographic Modeling System") with SWAN to study the evolution of a sediment bed for 10 idealized storms modeled after a 1992 storm in Massachusetts Bay.

It is to be noted that most of the coupling procedures described above have been applied either to hindcast studies or to idealized test cases where computational efficiency is not a critical issue. However when coupling between hydrodynamic and wave models is to be performed in forecasting mode (as is the case here), the modeler has to make a compromise between the accuracy and the computational efficiency of the forecast (of wave heights, water levels, surface currents, etc.).

Coupling Procedure

The coupling procedure was performed on a Macintosh computer with Quad-core processor and 8 GB RAM. SWAN can run in parallel mode for multi-processor systems, whereas EFDC is only capable of running in serial mode. In this study, we have utilized two-way off-line coupling involving three iterations. Both models are executed simultaneously without any cross-talk between the models (first iteration). A modeling

interface (written in MATLAB) is used to exchange the information between the two models. The modeling interface reads outputs from both the models and prepares appropriate input files for the next iteration. Specifically, the wave model provided hourly output of wave radiation stress which is fed into the circulation model to account for wave-induced circulation. The circulation model, on the other hand, generated hourly-fields of water surface elevation and surface-currents which are fed into the wave model. The simulations are then repeated for the second time. Upon completion of the second run, the information is again shared and the simulations are repeated for the third time.

For testing the coupling procedure outlined above, we selected a period of 10 days in the month of September 2008. Three processors were dedicated to SWAN, whereas one processor was assigned to EFDC. This set-up enabled both models to finish at approximately the same time. Both models (SWAN and EFDC) were initialized from motionless conditions on September 5. Fig. 6 shows comparison of wave parameters at the location of Buoy 46105. In general, the differences between the model results with and without the inclusion of currents at this location are marginal. Overall, the model results are in favorable agreement with data.
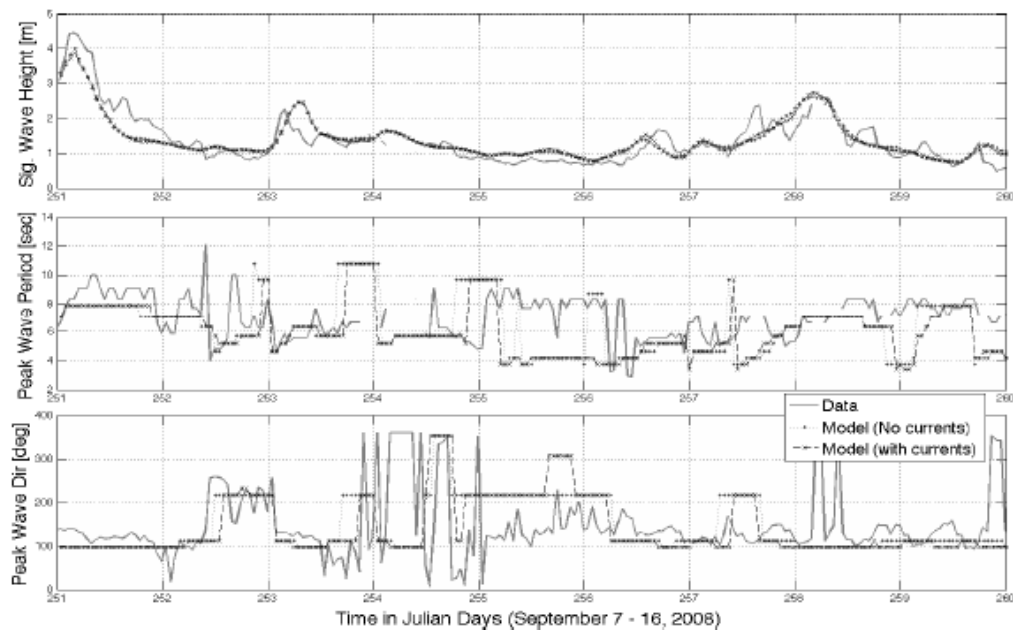

Figure 6. Wave model comparisons of SWH (top panel), peak wave period (middle panel), and peak wave direction (bottom panel) at the location of Buoy 46105. Solid line represents data, circled line shows model results without currents, and dash-crossed line shows model results with currents.

Inspection of spatial variation of SWHs during flood and ebb tidal cycles, however, reveals more prominent differences in the northern inlet when currents were included in the wave model. An example of such differences is shown on a zoomed region near Forelands (constricted area near center) during the flood tide (Fig.7). It can be seen that the presence of currents (Fig.7d), flowing opposite to the wind-wave flow (Fig.7a, b),

increases the SWHs in most parts of the region. Fig. 7c shows the difference between the model results obtained with the inclusion of currents and the model results obtained without the inclusion of currents. In the vicinity of Forelands, the difference is greater than 0.5 m (corresponding to about 50% increase in SWH). This clearly shows that the inclusion of currents in the wave model can greatly affect the wave climate in some areas of CI, which at times may pose hazardous conditions for navigation.
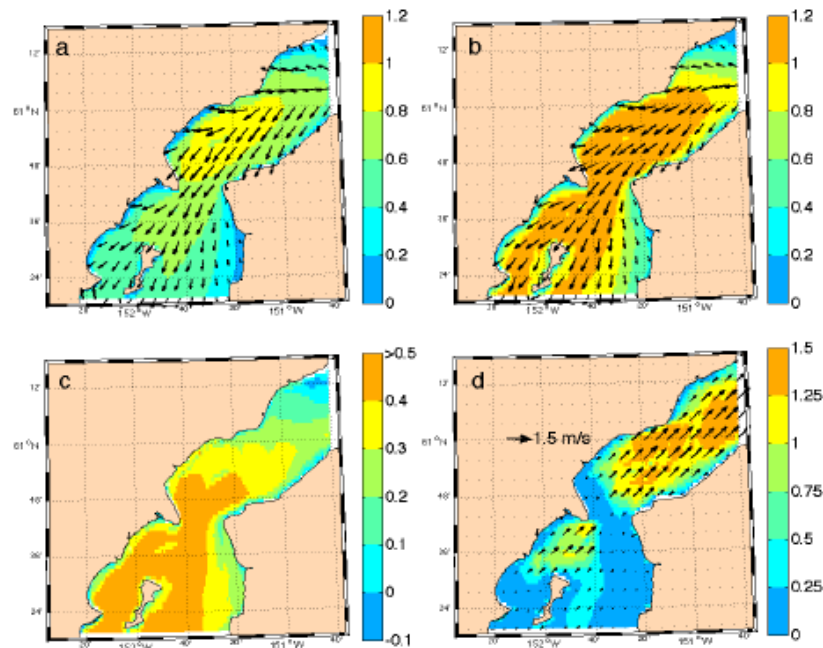

Figure 7. Model results during flood tide. (a) SWH (shaded; in m) and wave direction (arrows) without currents, (b) SWH (shaded; in m) and wave direction (arrows) with currents, (c) difference between SWH with and without currents (in m), and (d) current speed (shaded; in m/s) overlaid by current direction (arrows).

For the 10-day simulation, it was found that the effect of the wave model on the circulation model was very small (not shown). There were no readily discernible differences in the results of surface-currents (or water levels) upon inclusion of wave forcing in the circulation model. This may be because the tidal forcing mostly dominates the wave-induced forcing in CI. However, further testing is required in order to conclude that the coupling from wave model to the circulation model may not be necessary for the CI forecasting system.

SUMMARY AND CONCLUDING REMARKS

This study outlines the ongoing efforts towards the development of a coupled wind-wave-current forecasting system to assist in safety of maritime operations within the general region of CI. To date, we have established a base wave model and a base circulation model for CI. Wave modeling was performed using SWAN, whereas EFDC model was utilized for simulating the barotropic circulation. For studying the effects of wave-current interaction, the two models were coupled in the off-line mode using

78

multiple iterations. The SWH results from the coupled wave model showed remarkable differences in the upper inlet compared to those from the stand-alone results. This was mainly due to the presence of strong currents that changed the wave dynamics in the upper inlet. In some cases, it was found that the inclusion of currents resulted into waves moving in completely opposite direction. However, it was found that the impact of wave-induced circulation on the overall circulation pattern within CI was marginal.

Future work will involve identifying physical processes most relevant for implementing an efficient, yet reliable, coupled wind-wave-current forecasting system for CI. The preliminary results indicated that the wave-induced circulation (due to wave radiation stress) was not significant compared to the tidally-driven circulation. Additionally, waves can impact the wind-drag coefficients, which in turn, may alter the surface wind forcing and hence the wind-driven circulation. Thus there exists much need to further explore this effect in the circulation model. In addition, baroclinic gradients (fresh water discharge from rivers, etc.) are currently not incorporated into the circulation model. Some preliminary testing with baroclinic forcing indicated that the model computational time was greatly increased due to requirement of finer vertical model resolution and subsequently smaller model time-steps. Thus, it may not be operationally feasible to implement a fully 3D circulation model in the forecasting mode. We also plan to test the dynamic on-line coupling of the wave model and the circulation model, which may have some advantage over the off-line coupling in terms of avoiding multiple iterations.

Lastly, once the coupled system is fully tested and verified using available data, wave climatology could be developed for CI from coupled wave simulations for past several years. Based on these simulations, extreme wave estimates for a particular return period (e.g. 100-year) could be obtained. These estimates would be helpful for a variety of applications such as safety of marine operations, prevention of coastal disasters, design aspects of coastal/offshore structures, sediment transport studies, etc.

ACKNOWLEDGEMENTS

REFERENCES

Booij, N., Ris, R.C., and Holthuijsen, L.H. (1999). "A third-generation wave model for coastal regions, Part I: Model description and validation," *J. Geophys. Res.* 104(C4),7649-7666.
Chen, Q., Zhao, H., Hu, K., and Douglass, S.L. (2005). "Prediction of wind waves in a shallow estuary," *J. Waterway, Port, Coastal and Ocean Engg.* 131(4), 137-148.
Egbert, G.D. and Erofeeva, S.Y. (2002). "Efficient inverse modeling of barotropic ocean tides," *J. of Atmosph. and Oc. Tech.* 19(2), 183-204.
Funakoshi, Y., Hagen, S.C., and Bacopoulos, P. (2008). "Coupling of hydrodynamic and wave models: Case study for Hurricane Floyd (1999) hindcast," *J. Waterway,*

Port, Coastal and Ocean Engg. 134(6), 321-335.

Hamrick, J.M. (1992). "A three-dimensional environment fluid dynamics computer code: theoretical and computational aspects," Special Report 317. The College of William and Mary, Virgina Institute of Marine Science, Williamsburg, Virgina, 63pp.

Ji, Z.-G., Morton, M.R., and Hamrick, J.M. (2001). "Wetting and drying simulations of estuarine processes," *Estuarine, Coastal, and Shelf Science* 53, 683-700.

Jin, K.-R., Hamrick, J.H., and Tisdale, T. (2001). "Application of a three-dimensional hydrodynamic model for Lake Okeechobee," *J. Hydraulic Engg.* 126, 758-771.

Kuo, A.Y., Shen, J., and Hamrick, J.M. (1996). "The effect of acceleration on bottom shear stress in tidal estuaries," *J. Waterway, Port, Coastal, and Ocean Engg.* 122, 75-83.

Liu, H., Olsson, P.Q., Volz, K.P., and Yi, H. (2006). "A climatology of mesoscale model simulated low-level wind jets over Cook Inlet and Shelikof Strait, Alaska," *Estuarine, Shelf, and Coastal Science* 70 (4), 551-566.

Ris, R.C., Booij, N., and Holthuijsen, L.H. (1999). "A third-generation wave model for coastal regions, Part II: Verification," *J. Geophys. Res.* 104 (C4), 7667-7681.

Rogers, W.E., Kaihatu, J.M., Hsu, Y.L., Jensen, R., Dykes, J.D., and Holland, K.T. (2007). "Forecasting and hindcasting with the SWAN model in the Southern California Bight," *Coastal Engg.* 54 (1), 1-15.

Schoch, G.C., and Y. Chao (2010). "Ocean Observing system demonstrated in Alaska." *EOS* 11 (20), 181-182.

Shen, J., Boon, J., and Kuo, A.Y. (1999). "A numerical study of a tidal intrusion front and its impact on larval dispersion in the James River estuary," *Estuary* 22, 681-692.

Singhal, G., Panchang, V.G., and Lillibridge, J.L. (2010). "Reliability assessment for operational wave forecasting system in Prince William Sound, Alaska," *J. of Waterway, Port, Coastal, and Ocean Engg.* 136(6), 337-349.

Tolman, H.L. (2009). "User manual and system documentation of WAVEWATCH III version 3.14." *NOAA/NWS / NCEP / MMAB Technical Note* 276, 194pp.+ Appendices.

Warner, J.C., Sherwood, C.R., Signell, R.P., Harris, C.K., Arango, H.G. (2008). "Development of a three-dimensional, regional, coupled wave, current, and sediment-transport model," *Comp. Geosciences* 34, 1284-1306.

80

OCEANS'17 MTS/IEEE Conference in Anchorage, Alaska.

Operational wave forecast reliability in Cook Inlet, Alaska

Mindo Choi
Department of Ocean Engineering
Texas A&M University
College Station, TX, USA
mdchoi@tamu.edu

Vijay G. Panchang
Department of Ocean Engineering
Texas A&M University at Galveston
Galveston, TX, USA
panchanv@tamug.edu

Abstract— To enhance the safety of various marine operations in many coastal regions, ocean weather monitoring and prediction systems are playing an increasingly important role over the last couple of decades. To provide marine forecasts in Cook Inlet, Alaska, which has extremely complex geometry and the largest tidal fluctuations has in the U.S., a wave forecasting system is developed. High-resolution 36-hour forecasts of significant wave heights (SWHs) are provided daily. A comprehensive assessment of the forecasting system was performed by comparing the results with measurements from two satellites (JASON-2 and CRYOSAT-2) data for about 21 months. Scatter plots of observed data versus forecasts of SWHs and the probability of occurrence for groups of SWHs are presented as measures of wave forecast reliability. Correlation coefficients (R^2) and indices of agreement (D) between predicted and measured SWHs were reasonable for the full duration of study.

Keywords—Cook Inlet; Wave forecast reliability; Probability of occurrence

I. INTRODUCTION

The prediction of ocean wave heights is important for the safety of large and small seagoing vessels, for planning offshore operations, etc. In recent decades, a number of regional coastal ocean weather forecasting systems have been established for various parts of the US coast. The demand for reliable ocean information also comes from the need to avoid the risk of damage from winds, waves, and flooding and drying (e.g. boats running aground). The Cook Inlet (CI) region in Alaska is broadly exposed to the Gulf of Alaska which has among the largest waves in the world. Further, Cook Inlet exhibits the largest tidal fluctuations in the United States. It serves as a waterway connecting many ports for transport of natural resources, and also for fishing and recreational activities. As with many regions of Alaska, Cook Inlet is undergoing changes related to demands for conflicting uses as well as those related to global change. The inlet is the site of one of the largest remaining Beluga Whales run in the world and supports a large sport and commercial fishery. The Port of Anchorage plays an important role in providing supplies to Alaska's population. The Division of Oil and Gas in Department of Natural Resources has produced a map showing wells for oil and gas development in Cook Inlet in 2015. These existing and potential platforms will number more than 16 for off-shore and on-shore oil and gas reserves, which stretch from the Kachemak Bay to the nearshore of Upper Cook Inlet. Nearshore regions are often exposed to significant "wetting" and "drying" which can be hazardous to fishing and recreational vessels. Therefore, it is necessary to develop a system consisting of wind, wave, and tide models for reliably predicting ocean weather. Early efforts in that direction were described by Singhal et al. (2013) and Sharma et al. (2015).

Singhal et al. (2010) addressed the issue of forecast reliability in the context of wave prediction in Prince William Sound, Alaska. They used SWH data from the JASON-1, ENVISAT and GFO satellites as well as several NDBC buoys in their model domain. The satellites they used follow an exact repeat mission with the satellites flying over the same track every few days. A comprehensive assessment of the forecasted SWHs was performed through a statistical analysis by comparing them with satellite data which are available at specific lead times relative to the forecast (i.e. for lead times L=9 hr, 19 hr and L = 33 hr). Later, in Cook Inlet, Singhal et al. (2013) used NDBC buoys 46105 and 46106 to obtain wave data for wave model validation. However, these buoys have in recent years been unavailable.

As a result, there is no reliable source of wave data in upper and central CI which is the main focus of this study. Although NDBC buoys 46078 and 46080 are functional, they are located in lower CI and can only be used to obtain wave boundary conditions for the forecasting system. Therefore, the use of other sources in the form of remotely-sensed data is explored in this paper for analysis of the forecasting system, in particular, the SWHs. The approach taken here is similar to that proposed by Singhal et al. (2010). To get surface wave information, measurements from the JASON-2 and CRYOSAT-2 missions in this paper are used.

The work described here advances the preliminary validation work described by Sharma et al. (2015) in CI. In terms of assessing forecast skill, the lead times used here are different from the fixed times used by Singhal et al. (2010) in Prince William Sound, owing to satellite flight protocols being different. Also, we provide an assessment of wind forecasts. (Singhal et al. (2010) examined SWHs only).

II. MODELING SYSTEM

CI is a ~175 mile long estuary with Anchorage at its head. As noted by Singhal et al. (2013) and others, the CI domain is characterized by extremely complex geometry, with islands and rugged mountains that create strong and complex wind-fields. As noted earlier, it has among the largest waves in the world and the largest tidal fluctuations in the United States. It is therefore necessary to use a sophisticated system of wind, wave, and circulation models to develop reliable ocean weather predictions in CI.

An integrated system for forecasting has been developed, consisting of the wave model SWAN, the circulation model EFDC, and thee wind model WRF. The wind model is operationally run at the University of Alaska's "Alaska Experimental Forecast Facility". Its forecast output is accessed, along with NOAA's WAVEWATCH output at the open ocean boundary to force the wave model. The forecast system is run at Texas A&M University at Galveston, http://www.tamug.edu/ocen/WaveSimulation/GofAlaska.html. For details, see Singhal et al. (2013) and Sharma et al. (2015).

III. SATELLITE DATA

A satellite altimeter an essentially measures wave heights based on a radar pulse as it flies along its tracks. In this study, we used the JASON-2 and CRYOSAT-2 satellites for comparing with the model. JASON-2 operates using two different radar frequencies, viz. the Ku-band (13.6 GHz) and C-band (5.3 GHz). The Ku-band is most commonly used frequency for JASON-1, ENVISAT, etc. JASON-2 flies in low-earth orbit with a global coverage between 66°N and 66°S latitude and also covers 95% of world oceans with tracks repeating approximately 10 days apart. The other satellite used, CRYOSAT-2, is an altimetry satellite built by ESA (European Space Agency) and it also measures SWH (Ku-band) and wind. The repeat periods for JASON-2 and CRYOSAT-2 tracks are *approximately* 10 days and 30 days, respectively. Fig. 1 shows repeat paths for JASON-2 and CRYOSAT-2 which have a cyclic pattern in the Cook Inlet region.

The altimeter cannot measure reliably SWH data when it passes close to the coast (flying from ocean to land and vice versa). Measurements, therefore, are eliminated from our comparison if they appeared suspicious or unreliable, based on a detailed qualitative examination. SWH and wind data are extracted from AVISO (http://www.aviso.altimetry.fr/en/home.html) which provides 1°x 1°, gridded multi-mission wind/wave data and specific along-track data sets in CI region, using the "Radar Altimeter Acquisition System" or "RADS" which provides specific along-track data sets (http://rads.tudelft.nl/rads/data/authentication.cgi), as noted in Sharma et al. (2015). Comparisons between model and satellite data are made for the dates when the satellite passes over CI. SWHs measured during January 2015 to September 2016 are analyzed. During the initial analysis, we found that it is difficult to make comparisons because few, if any, satellite tracks fall directly over the model grid points. Therefore, for the comparisons, SWH data are used from the four nearest model grid points and averaged.
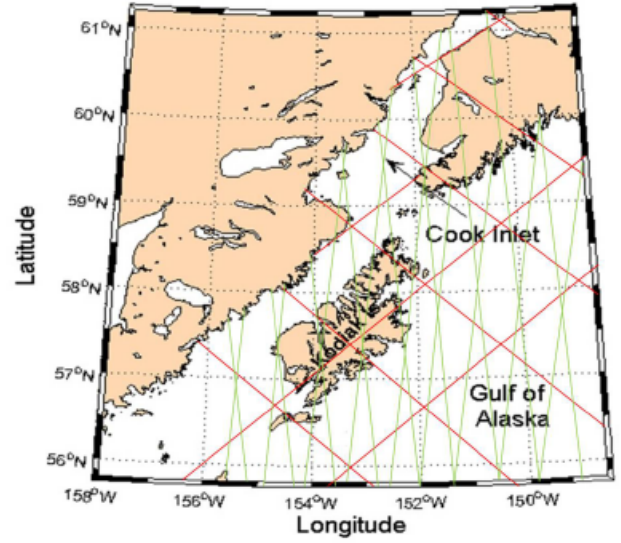

Fig. 1. Track of JASON-2 (red line) and CRYOSAT-2 (green line) satellites near Cook Inlet region

IV. ASSESSMENT OF FORECAST SKILL

Sharma et al. (2015) provided some validation of the model results in terms of plots comparing satellite track data overlaid on model predictions. Here, SWH and wind data measured during January 2015 to September 2016 are analyzed for a 21 month statistical study. Assessment of forecast skill is provided in terms of scatter plots and the likelihood of a forecast representing an actual sea-state. For the former, we use the following metrics below, and note that O is observed SWH, P is modeled SWH, σ is the standard derivation and N is sample size.

$$\text{Correlation coefficient (R}^2) = \left(\frac{\overline{(O-\overline{O})(P-\overline{P})}}{\sigma_O \sigma_P} \right)^2$$

$$\text{Root-mean-square error (RMSE)} = \sqrt{\frac{\sum_{i=1}^{N}(O_i - P_i)^2}{N}}$$

$$\text{Index of agreement (D)} = 1 - \frac{N(RMSE)^2}{\sum_{i=1}^{N}\left[|P_i - \overline{O}| + |O_i - \overline{O}|\right]^2}$$

$$\text{Absolute error} = \frac{|O_i - P_i|}{O_i}$$

To place some bounds on the range of actual sea-states which a forecast could represent, we used the two methods described by Singhal et al. (2010): (1) the RMSE method and (2) the absolute error method. First, we placed all predicted SWHs into distinct groups with fixed lead time proposed by Singhal et al. (2010). However, unlike the work of Singhal et al. (2010) in Prince William Sound, satellite data with JASON-2 and CRYOSAT-2 are available at different times in CI for each pass. i.e. the JASON-2 overflights repeat every 9.92 days,
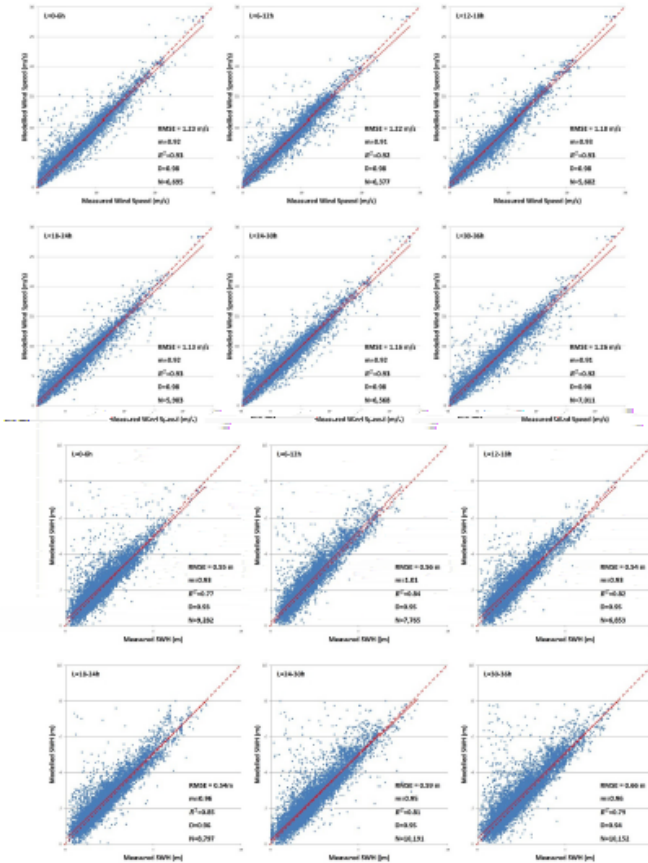
Fig. 2. Comparison of SWH for L=0-6 h, L=6-12 h, L=12-18 h, L=18-24 h, L=24-30 h and L=30-36 h. Points represent data from 2 satellites (JASON-2 and CRYOSAT-2), solid line represents best-fit slope and dashed line represents slope of unity

which means a repeat pass occurs on a 10-day later date, but two hours earlier, so these data yield different lead times relative to the forecasts made at noon the same day and previous day. A similar feature occurs for CRYOSAT-2 also (i.e. its repeat period is 28.14 days). The comparisons, therefore, were grouped into 6 categories with 6 hour intervals (Murphy, 1988), viz. 0 < L < 6 hr, 6 hr < L < 12hr, 12 hr < L < 18 hr, 18 hr < L < 24 hr, 24 hr < L < 30 hr and 30 hr < L < 36 hr from 0–1.5m, 1.5–3m, 3–5m and 5–8m. Grouping of SWHs is based on the predicted values (not measurements). For the RMSE method, the RMSE for each predicted SWH group was estimated. Then, the difference between each predicted SWH and the corresponding measured value was calculated. The percentage of data points for which this difference falls within specified intervals (0.5, 1.0, and 1.5 times the RMSE) are estimated. For the second method, the absolute error for each predicted SWH was computed, and the percentages of values that fell within 15%, 25%, and 35% absolute errors were estimated.

The results of the statistical analyses are shown in Fig. 2, for L=0-6h, 6-12h, 12-18h, 18-24h, 24h-30h and 30h- 36h with 6h intervals. The plots in Fig. 2 show that the agreement between the observed and the forecasted SWHs. The quality of

TABLE I. OVERALL STATISTICS OF PREDICTED SWHs WITH JASON-2 AND CRYOSAT-2

L (h)	Predicted SHW group (m)	RMSE (m)	RMSE bound 0.5	RMSE bound 1	RMSE bound 1.5	Absolute error bound 15 (%)	Absolute error bound 25 (%)	Absolute error bound 35 (%)	Samples (N)
			Probability of Occurrence						
0-6h	0.0-1.5	0.33	0.82	0.93	0.96	0.43	0.65	0.79	2790
	1.5-3.0	0.44	0.77	0.89	0.94	0.58	0.77	0.86	4683
	3.0-5.0	0.78	0.73	0.83	0.89	0.66	0.80	0.85	1620
	5.0-8.0	1.82	0.74	0.75	0.79	0.70	0.76	0.80	189
	Overall	0.55	0.81	0.91	0.94	0.55	0.74	0.84	9282
6-12h	0.0-1.5	0.32	0.83	0.92	0.96	0.45	0.65	0.79	2028
	1.5-3.0	0.41	0.79	0.90	0.95	0.60	0.80	0.88	3719
	3.0-5.0	0.77	0.67	0.82	0.88	0.56	0.75	0.85	1619
	5.0-8.0	1.31	0.64	0.77	0.83	0.61	0.77	0.87	399
	Overall	0.56	0.53	0.61	0.64	0.55	0.25	0.85	7265
12-18h	0.0-1.5	0.32	0.81	0.92	0.97	0.39	0.61	0.75	1948
	1.5-3.0	0.41	0.77	0.91	0.95	0.58	0.78	0.87	3309
	3.0-5.0	0.57	0.65	0.83	0.92	0.64	0.84	0.92	1196
	5.0-8.0	0.55	0.57	0.77	0.91	0.79	0.99	1.00	152
	Overall	0.43	0.76	0.89	0.94	0.54	0.74	0.84	6605
18-24h	0.0-1.5	0.35	0.81	0.92	0.96	0.41	0.62	0.76	2378
	1.5-3.0	0.52	0.75	0.88	0.93	0.47	0.68	0.80	3665
	3.0-5.0	0.79	0.69	0.83	0.88	0.62	0.76	0.85	1629
	5.0-8.0	0.89	0.61	0.77	0.87	0.67	0.90	0.96	383
	Overall	0.57	0.77	0.88	0.92	0.49	0.69	0.80	8055
24-30h	0.0-1.5	0.37	0.80	0.91	0.96	0.37	0.60	0.76	3011
	1.5-3.0	0.45	0.76	0.89	0.94	0.59	0.78	0.87	4348
	3.0-5.0	0.77	0.72	0.84	0.88	0.67	0.83	0.90	2217
	5.0-8.0	1.39	0.68	0.80	0.84	0.62	0.78	0.86	615
	Overall	0.59	0.79	0.90	0.94	0.56	0.74	0.84	10191
30-36h	0.0-1.5	0.37	0.80	0.92	0.96	0.39	0.62	0.78	2838
	1.5-3.0	0.47	0.77	0.89	0.93	0.58	0.78	0.86	4753
	3.0-5.0	0.75	0.72	0.84	0.89	0.65	0.80	0.87	2497
	5.0-8.0	1.36	0.67	0.80	0.85	0.61	0.79	0.87	666
	Overall	0.61	0.79	0.89	0.93	0.55	0.74	0.84	10754

the forecast appears to be lower for longer lead times (e.g. RMSE is 0.55m for L = 0-6 hr and 0.66m for L = 30-36 hr). In general, the correlation for the wave heights is high for all forecasts (R^2 = 0.77, 0.84, 0.82, 0.85, 0.81 and 0.79).

This is an indicator of reliable prediction capability. Moreover, the R^2 is slightly higher for the wind speed (R^2 = 0.93, 0.92, 0.93, 0.93, 0.93 and 0.92). The range of an actual sea-state which a forecasted event represents may be determined from Table 1. To use Table 1 for L=12-18hr, for instance, it is seen that the predictions that fall in the 1.5-3m range have an RMSE of 0.41m; these predictions would have a 91% chance of actually representing a sea-state between 1.06m and 3.44m (1.5-1×RMSE and 3.0+1×RMSE). Similarly, for the L=18-24 hr forecast that falls in the 3m - 5m interval, there would be a 72% chance of the actual conditions being between 2.68m (3-0.5×RMSE) and 5.32m (5+0.5×RMSE). Using the absolute error method, for L=24-30h, a prediction of 5m-8m would have an 78% of chance of experiencing a sea state between 3.75m (5m-0.25%) and 10.0m (8m+25%).

V. SUMMARY AND CONCLUDING REMARKS

The present study focus on assessment of quality of SWH and wind observations from JASON-2 and CRYOSAT-2 satellites. For the assessing reliability of wave forecast, forecast

data from period January 2015 to September 2016 were used. The above analysis represents a relatively novel but truly useful method, based on Singhal et al. (2010), of assessing forecast reliability. The comprehensive assessment of the results presented in Fig. 2 suggests that the predictions are close to reality, and the data in Tables 1 demonstrates that the forecast system provides results which are within 0.5*RMSE of the actual sea-state approximately 75% of the time. This enhances the practical benefit of the system to the user of the forecasts.

REFERENCES

[1] Booij, N., Holthuijsen, L. H., Doorn N., and Kieftenburg, A. T. M. M., (1997). "Diffraction in a Spectral Wave Model." Ocean Wave Measurements and Analysis: Proc. 3rd Int. Symp., Waves97, ASCE, 243-255.

[2] Booij, N., Ris, R.C., and Holthuijsen, L.H. (1999). "A third-generation wave model for coastal regions, Part I: Model description and validation." J. Geophys. Res., 104(C4), 7649-7666.

[3] Egbert, G.D. and Erofeeva, S.Y. (2002). "Efficient inverse modeling of barotropic ocean tides." J. of Atmosph. and Ocean Tech., 19(2), 183-204.

[4] Cryosat-2 product handbook. (2010). ESA/European Space Agency

[5] Funakoshi, Y., Hagen, S.C., and Bacopoulos, P. (2008). "Coupling of hydrodynamic and wave models: Case study for Hurricane Floyd (1999) hindcast." J. Waterway, Port, Coastal and Ocean Engrg., 134(6), 321-335.

[6] Hamrick, J.M. (1992). "A three-dimensional environment fluid dynamics computer code: theoretical and computational aspects." Special Report 317. The College of William and Mary, Virginia Institute of Marine Science, Williamsburg, Virginia, 63.

[7] Murphy, Allan H., (1988). "Skill scores based on the mean square error and their relationship to the correlation coeffiecient." J. of Monthly Weather Review, 116, 2417-2424.

[8] Ocean Surface Topography Mission (OSTM)/Jason-2 Product Handbook. (2009). NOAA/NESDIS, Polar Series/OSTM J400

[9] Oey, L-Y., Ezer, Tal, Hu, C. and Muller-K. Frank E. (2007). "Baroclinic tidal flows and inundation processes in Cook Inlet, Alfaska: numerical modeling and satellite observations." Ocean Dynamics, 57(3), 205-221.

[10] Ris, R. C.,Holthuijsen, L. H. and Booij, N. (1999). "A Third-Generation Wave Model for Coastal Regions, 2, Verification." J. Geophys. Res., 104(C4) 7667-7681.

[11] Rogers, W. E., J. M. Kaihatu, H. A. H. Petit, N. Booij and L. H. Holthuijsen (2002). "Diffusion reduction in an arbitrary scale third generation wind wave model." Ocean Engrg., 29(11), 1357-1390.

[12] Sharma, A., Choi, M., and Panchang, V.G. (2015). "Development and Validation of an Operational Forecasting System for Waves and Coastal Flooding and Drying in Cook Inlet, Alaska." Coastal Structures and Solutions to Coastal Disasters, Boston, Massachusetts, USA, 238-246.

[13] Singhal, G., Panchang, V.G., and Lillibridge, J.L. (2010). "Reliability assessment for operational wave forecasting system in Prince William Sound, Alaska." J. of Waterway, Port, Coastal, and Ocean Engrg., 136(6), 337-349.

[14] Singhal, G., Panchang, V.G., and Nelson, A.J. (2013). "Sensitivity assessment of wave heights to surface forcing in Cook Inlet, Alaska." Continental Shelf Research, 63(S15), S50-S62.

[15] Tolman, H.L. (2009). "User manual and system documentation of WAVEWATCH III version 3.14." NOAA/NWS / NCEP / MMAB Technical Note 276, NCEP.

Development and Validation of an Operational Forecasting System for Waves and Coastal Flooding and Drying in Cook Inlet, Alaska

Coastal Structures and Solutions to Coastal Disasters 2015   238

Abhishek Sharma[1]; Mindo Choi[2]; and Vijay Panchang[3]

[1]Dept. of Ocean Engineering, Texas A&M Univ., 31β6 TAMU, College Station, TX 77843, U.S.A. E-mail: abhishek.sharma@neo.tamu.edu
[2]Dept. of Ocean Engineering, Texas A&M Univ., 3136 TAMU, College Station, TX 77843, U.S.A. E-mail: mdchoi@tamu.edu
[3]Dept. of Ocean Engineering, Texas A&M Univ. at Galveston, 200 Seawolf Pkwy, Galveston, TX 77553, U.S.A. E-mail: panchangv@tamug.edu

ABSTRACT

Exposed on three sides to the Gulf of Alaska, the Cook Inlet region is an extremely dynamic system which has among the largest waves in the world. In addition, Cook Inlet exhibits the largest tidal fluctuations in the United States, and as a result, the nearshore regions encounter significant flooding and drying which poses threats to a variety of activities in the coastal regions. A coupled wind-wave-current system is developed to obtain daily forecasts of waves and circulation patterns. The SWAN wave model and the quasi three-dimensional EFDC flow model are implemented, using high-resolution WRF winds. The performance of these models is first verified using hindcast simulations. The forecasting system also simulates the extent of "wet" and "dry" regions in the coastal areas. The nested grid approach is utilized with high-resolution grids for two separate regions, namely the Kachemak Bay (KB) and the Upper Cook Inlet (UCI) region. To validate the efficiency of the forecasting system to reliably predict the wave parameters, satellite data from currently flying missions such as JASON-2, and CRYOSAT-2 are utilized. Moreover, the data from the Terra (MODIS) satellite are used to obtain true color and land reflectance (band 1-2) images of the Cook Inlet region. These images are then used to corroborate the efficacy of the system for providing accurate estimates of the extent of "wet" and "dry" regions. Good agreement between data and model results demonstrate the efficiency of this coupled system for operational forecasting.

INTRODUCTION

Cook Inlet (CI) is a ~175 mile long estuary that facilitates a variety of activities such as shipping, oil and gas extraction, etc. At its head, Anchorage is Alaska's largest city and a center of tourism, transportation, recreation, and commerce. The Port of Anchorage plays an important role in providing supplies to Alaska's population. Navigational routes in CI that connect the ports of Anchorage, Nikiski, Homer, and Drift River are also used to export seafood, minerals, and gas.

The CI domain is characterized by extremely complex geometry. It consists of islands and ruggedly mountainous terrains that create strong and complex wind-fields. As a result, CI region is an extremely dynamic system which has among the largest waves in the world, and the largest tidal fluctuations in the United States. Nearshore regions are often exposed to significant "wetting" and "drying" which often poses a hazard to fishing and recreational vessels. It is therefore necessary to use a sophisticated system of wind, wave and tide models for accurate ocean weather prediction in CI.

The objectives of this study are to develop integrated forecasting schemes for CI region and

85

to validate the different components of the forecasting system using available data. Note that, even after more than 25 years of the Exxon Valdez disaster, there is a paucity of reliable sources that provide ocean weather information in CI. Due to the importance of CI for the Alaskan region, there is always an established need for reliable ocean weather predictions. These predictions can help in safeguarding operations of cargo ships, tankers, fishing and recreational vessels in CI, and may also be used by concerned authorities to avoid the hazards imposed by mudflats exposed during "drying" events.
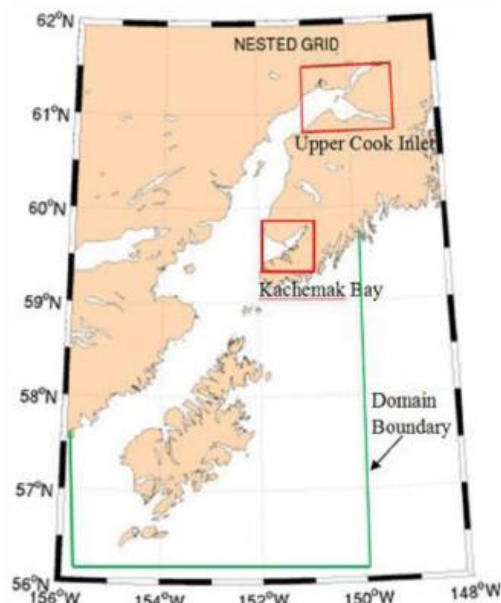
Figure 1. Outer Cook Inlet Domain, and nested KB and UCI domains.

Singhal et al. (2013) discussed various modeling methods for wind, circulation, wave, and coupled wave–current modeling. They examined wave–current interaction by coupling a wave model and a circulation model. Singhal et al. (2013) also used NDBC buoys 46105 and 46106 to obtain wave data for wave model validation. However, buoy 46106 went adrift in May 2011 and was later disestablished. Similarly, buoy 46105 was decommissioned starting January 2013. As a result, there is no reliable source of wave data in upper and central CI which is the main focus of this study. Although NDBC buoys 46078 and 46080 are functional, they are located in lower CI and can only be used to obtain wave boundary conditions for the forecasting system. Therefore, the use of other sources in the form of remotely-sensed data is explored in this paper for validating the forecasting system.

Here, we obtain wave predictions for CI on local high-resolution domains and validate them using satellite altimeter data. The approach taken here is similar to that proposed by Singhal et al. (2010) in Prince William Sound, Alaska. To get surface wave information, the JASON-2 and CRYOSAT-2 missions are used. Moreover, in nearshore regions where "wetting" and "drying" is significant, satellite images obtained using Terra MODIS satellite are used to map the extent of wet and dry regions and to test the performance of the forecasting system.

In the subsequent sections, various components of the forecasting system such as bathymetry,

© ASCE

input wind-fields, boundary conditions, wave and circulation model, and integrated forecasting schemes are discussed. In addition, validation of the forecasting system is performed using remote-sensed data.

BATHYMETRY

Various bathymetric datasets for CI (e.g. Etopo1/Etopo2 Global Relief Models and the Tsunami Inundation Digital Elevation Model) are available. The DEM dataset (24 s resolution) is presently the highest resolution available. The DEM data are therefore used in the present study, and missing bathymetry in the Turnagain Arm region is obtained using past surveys and navigational charts. The bathymetry used here is similar to the one used in Singhal et al. (2010) and Oey et al. (2007). Readers may refer to these papers for more details.
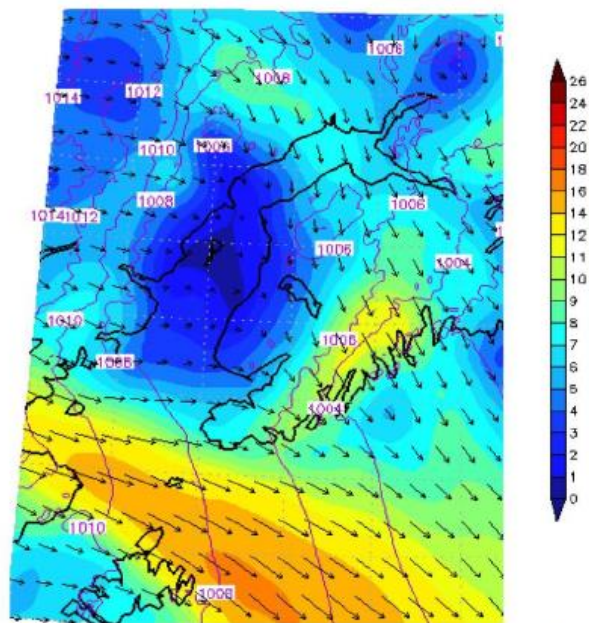
Figure 2. Example WRF wind field (in m/s) forecasted by Alaska Experimental Forecast Facility
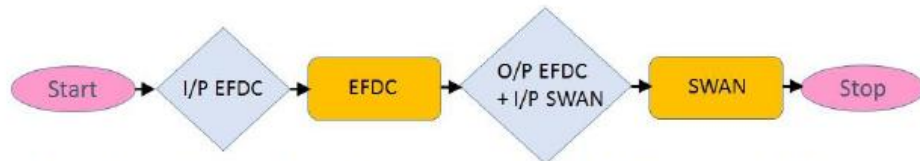

Figure 3. Offline coupling with one-way approach. I/P is input, O/P is output.

© ASCE

87

MODELING METHODOLOGY

We discuss the integrated forecasting schemes used in the development of a coupled wave-wind-tide system for the CI region. The computational domain covered the region between -156°W and -149°W, and 56°N and 61.5°N. Fig. 1 shows the extent of outer domain and two high-resolution nested domains, namely Kachemak Bay (KB) and Upper Cook Inlet (UCI). To simulate wave transformation, the third-generation wave model SWAN ("Simulating WAves Nearshore") was utilized. The SWAN model simulates wave transformation due to shoaling, refraction, blocking and reflection due to spatial variation in bathymetry and currents (e.g. Booij et al. 1999; Ris et al. 1999; Rogers et al. 2007; Funakoshi et al. 2008). The boundary values on the open ocean boundaries were obtained using WAVEWATCH III (Tolman 2009) model for the Alaskan regions.

Figure 4. The orbits along the tracks of Cryosat-2 over a three day period (left) and Jason-2 over a ten day period (right).
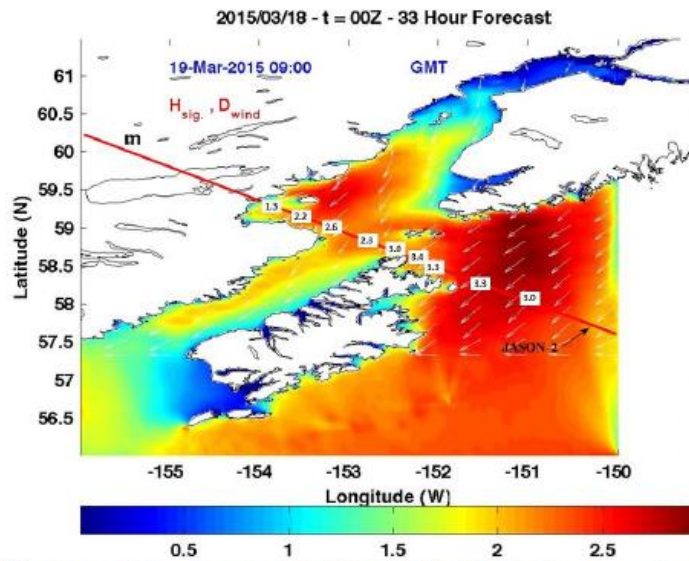
Figure 5. SWH comparisons (meters) for March 18, 2015 at 9 a.m.; color: 33-h forecast; white boxes; JASON-2 satellite measurements.
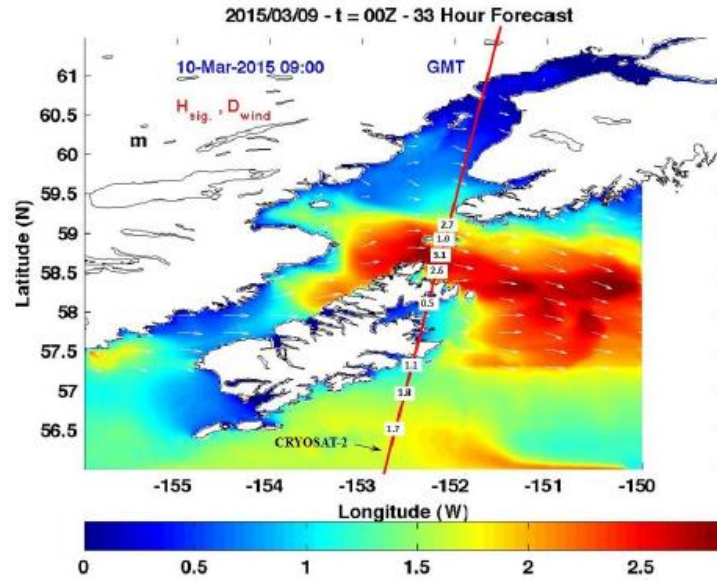
© ASCE

88

Figure 6. SWH comparisons (meters) for March 09, 2015 at 9 a.m.; color: 33-h forecast; white boxes; CRYOSAT-2 satellite measurements.
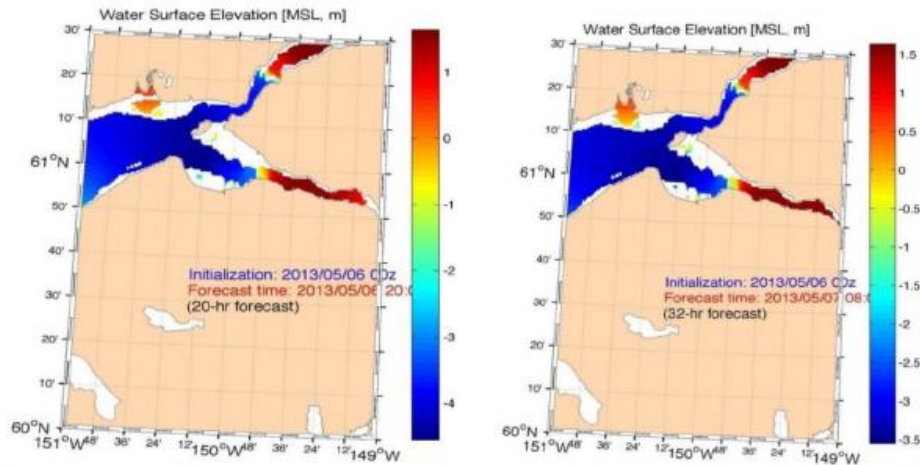

Fig. 7. Forecasted instantaneous water surface elevations for the high resolution UCI domain. White patches depict "dry" regions.

The forecasting system uses EPA's Environmental Fluid Dynamics Code (EFDC) for simulating flow field. The model solves the three-dimensional, vertically hydrostatic, free surface, turbulent averaged equations of motions (Hamrick, 1992). EFDC was applied to the CI domain on an irregular grid with a spatial grid resolution varying between 4 km near the open boundaries and 1 km in the northern most parts of CI. Boundary conditions in terms of surface elevations and currents are obtained using TPXO6.2 global satellite-based tidal model (Egbert and Erofeeva, 2002). The EFDC model for CI was tested via simulation of tidal conditions by

© ASCE

Singhal et al. (2013). The wind-fields (see Fig. 2) for both SWAN and EFDC are obtained using Alaska Experimental Forecast Facility (AEFF).

In general, the coupling between the wave and circulation models is performed using offline coupling (OFC) or online coupling (ONC). Details regarding these coupling methods are discussed in Singhal et al. (2013). They stated, "…for forecasting purposes, one-way coupling would be adequate; two-way coupling, albeit incorporating better physics, has less of an effect on the accuracy of the forecast than improved wind-fields." Moreover, they found the effect of the waves on the currents marginal and deemed the ONC approach unnecessary for CI domain. To develop the forecasting system, only offline coupling with one-way approach shown in Fig. 3 is considered.

To provide coupled wave-wind-tide forecasts systematically on a daily basis, a MATLAB protocol to automatically run the simulations is developed. The approach used here is similar to the one described by Singhal et al. (2010) and is not discussed here in detail.

For the outer (coarse) grid simulation, the boundary conditions are pre-specified. Eight tidal constituents, namely: M2, S2, N2, K2, K1, O1, P1 and Q1 are extracted along these boundaries and updated every hour. For the KB and UCI domains, the boundary conditions derived from the modeled results for the outer (coarse) grid simulation. Although the wetting and drying mode is activated for all three domains, the KB and UCI domains with finer grid resolution provide more reliable estimates of "wet/dry" regions. While running EFDC, the representative depth at which the grid is assumed to become dry (HDRY) must be selected to model the extent of dry regions. For each time-step, the model checks the total depth against the specified threshold depth HDRY at each grid point. Here, HDRY was set equal to 0.5 m.
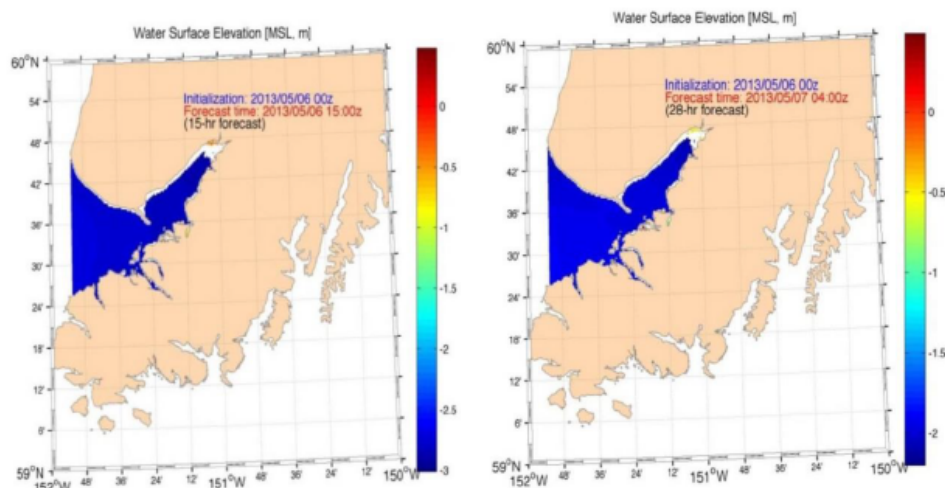

Fig. 8. Forecasted instantaneous water surface elevations for the high resolution KB domain. White patches depict "dry" regions.

VALIDATION

(a) Significant Wave heights (SWHs)

To validate the efficiency of the forecasting system, satellite data from currently flying missions like JASON-2 and CRYOSAT-2 can be used, as noted previously. The tracks along

JASON-2 and CRYOSAT-2 orbits are shown in Fig. 4. The work of data acquisition is tedious and we have been trying to identify appropriate tracks that also match the model predictions in space and time. We have collected satellite data from AVISO (http://www.aviso.altimetry.fr/en/home.html) which provides 1°x 1°, gridded multi-mission wind/wave data and specific along-track data sets in Cook Inlet region. As shown in Fig. 4, a suite of satellite tracks from JASON-2 and CRYOSAT-2 are used in our analysis.
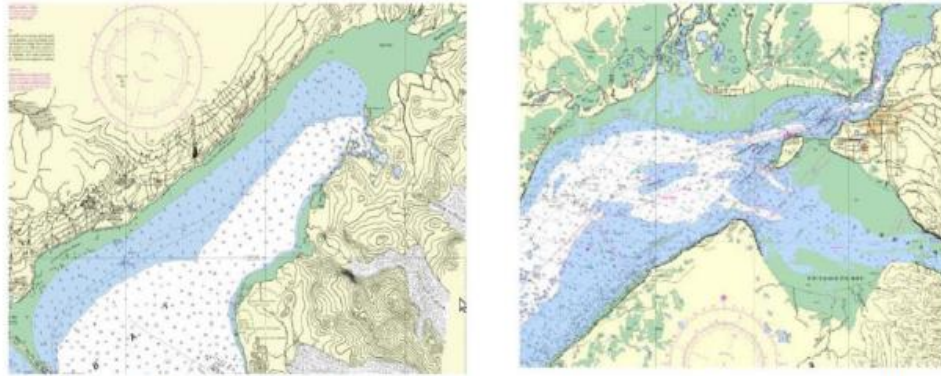
Fig. 9 Map of KB (left) and UCI (right) showing the extent of dry regions, which are depicted by the green shaded area (source: NOAA).
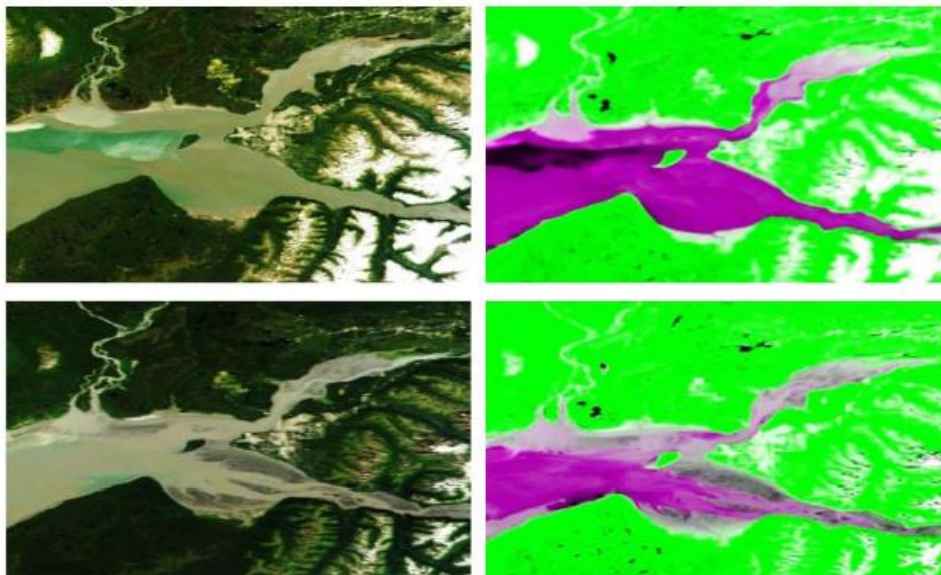
Figure 10. High tide event (top panel) and low tide event (bottom panel). True color satellite images (left) and Landsat TM images (right) for UCI region.

The "Radar Altimeter Acquisition System" or "RADS" which provides specific along-track data sets (http://rads.tudelft.nl/rads/data/authentication.cgi) is used here. Using RADS, the significant wave height data have been collected using automated MATLAB scripts which plot

© ASCE

91

the along-track data from their ASCII files.). Comparisons between model and satellite data are made for the dates when the satellite passes over CI. SWHs measured during January 2015 to April 2015 are analyzed. During the initial analysis, as we mentioned before, we found that it is difficult to make comparisons because few, if any, satellite tracks fall directly over the model grid points. Therefore, for the comparisons, significant wave height data are used from 4 nearest model grid points then averaged.

The significant wave height data obtained from the model are compared with measurements from the satellites for about four months, as stated earlier. Comparisons, for two tracks in March 2015, are shown in Figs. 5 and Figs. 6 for JASON-2 and CRYOSAT-2, respectively. The results show that the modelled significant wave heights were in the range of 1-3 m, and that they corresponded to the satellite measurements reasonably well. The comparisons at this point are too few for detailed statistical analyses, but the modelled data and measurements data are fairly close to each other. This is promising, and inspires confidence in the model results.

(b) Water Surface Elevations (WSEs)

Contour plots of recent intermediate hour forecasts (for 0000 GMT run on May 06, 2013) of WSEs obtained from the operational system for nested UCI and KB domains are shown in Figs. 7 and 8 respectively.

Note that the white patches in these plots depict dry regions. NOAA navigational charts for UCI and KB domains are shown in Fig. 9. For both nested domains, the dry regions predicted (see Fig. 7 and 8) by the forecasting system during the low tide event match reasonably well with the green shaded area in NOAA charts. Moreover, the true color and Landsat TM images obtained using data from Terra (MODIS) satellite are shown in Fig. 10 for the UCI domain. The extent of wet and dry regions seen in these satellite images is also in agreement with the extent predicted by the present system.

SUMMARY AND CONCLUSIONS

In this paper, the development of a forecasting system for CI region is discussed. The efficiency of the system to reliably predict the wave heights and the extent of wetting and drying is then corroborated using satellite data from currently flying missions. Satisfactory agreement between data and model results demonstrate the efficacy of this coupled system for operational forecasting. In future, we plan to conduct more detailed comparisons of modeled results with satellite data for a number of events during a tidal cycle. Such comparisons will be the true test of the system in simulating wetting and drying.

ACKNOWLEDGEMENTS

REFERENCES

Booij, N., Ris, R.C., and Holthuijsen, L.H. (1999). "A third-generation wave model for coastal regions, Part I: Model description and validation." *J. Geophys. Res.,* 104(C4), 7649-7666.

Egbert, G.D. and Erofeeva, S.Y. (2002). "Efficient inverse modeling of barotropic ocean tides." *J. of Atmosph. and Ocean Tech.,* 19(2), 183-204.

Funakoshi, Y., Hagen, S.C., and Bacopoulos, P. (2008). "Coupling of hydrodynamic and wave

92

models: Case study for Hurricane Floyd (1999) hindcast." *J. Waterway, Port, Coastal and Ocean Engrg.*, 134(6), 321-335.

Hamrick, J.M. (1992). "A three-dimensional environment fluid dynamics computer code: theoretical and computational aspects." *Special Report 317. The College of William and Mary*, Virginia Institute of Marine Science, Williamsburg, Virginia, 63.

Ocean Surface Topography Mission (OSTM)/Jason-2 Product Handbook. (2009). *NOAA/NESDIS*, Polar Series/OSTM J400

Oey, L-Y., Ezer, Tal, Hu, C. and Muller-K. Frank E. (2007). "Baroclinic tidal flows and inundation processes in Cook Inlet, Alfaska: numerical modeling and satellite observations." *Ocean Dynamics*, 57(3), 205-221.

Ris, R.C., Booij, N., and Holthuijsen, L.H. (1999). "A third-generation wave model for coastal regions, Part II: Verification." *J. Geophys. Res.*, 104(C4), 7667-7681.

Rogers, W.E., Kaihatu, J.M., Hsu, Y.L., Jensen, R., Dykes, J.D., and Holland, K.T. (2007). "Forecasting and hindcasting with the SWAN model in the Southern California Bight." *Coastal Engineering*, 54 (1), 1-15.

Singhal, G., Panchang, V.G., and Lillibridge, J.L. (2010). "Reliability assessment for operational wave forecasting system in Prince William Sound, Alaska," *J. of Waterway, Port, Coastal, and Ocean Engrg.*, 136(6), 337-349.

Singhal, G., Panchang, V.G., and Nelson, A.J. (2013). "Sensitivity assessment of wave heights to surface forcing in Cook Inlet, Alaska." *Continental Shelf Research*, 63, S50-S62.

Tolman, H.L. (2009). "User manual and system documentation of WAVEWATCH III version 3.14." *NOAA/NWS / NCEP / MMAB Technical Note 276*, 194.+ Appendices.

© ASCE

93